



Cite this: *J. Mater. Chem. A*, 2021, 9, 154

Recent advances in layered $\text{Ln}_2\text{NiO}_{4+\delta}$ nickelates: fundamentals and prospects of their applications in protonic ceramic fuel and electrolysis cells†

Artem P. Tarutin,^{ab} Julia G. Lyagaeva,^{ab} Dmitry A. Medvedev,^{ab} Lei Bi^{cd} and Aleksey A. Yaremchenko^{bd}

In the past decade, intensive research on proton-conducting oxide materials has provided a basis for the development of intermediate-temperature protonic ceramic electrochemical cells, which constitute a real alternative to conventional cells based on oxygen-conducting electrolytes. To achieve both high efficiency and excellent performance, not only electrolytes but also electrode materials should be carefully selected considering their functional properties. Compared to the traditional ABO_3 perovskite electrode materials, $\text{Ln}_2\text{NiO}_{4+\delta}$ with a layered structure has unique advantages (high chemical stability, mechanical compatibility, improved oxygen transport, and hydration ability), and thus is now becoming a hot topic in this field, offering both scientific and practical interests. However, a comprehensive and in-depth review is still lacking in the literature to date. Accordingly, this work presents a comprehensive overview of the prospects of layered nickelates ($\text{Ln}_2\text{NiO}_{4+\delta}$, where Ln = La, Nd, and Pr) as one of the most attractive oxygen (steam) electrode materials for protonic ceramic electrochemical cells. In particular, the crystalline features, defect structure, stability, chemical properties, and mechanical compatibility of this class of materials, contributing to their transport functionality, are discussed with the primary emphasis on revealing the relationship between the composition of the materials and their properties. The presented systematic results reveal the main strategies regarding the utilisation of $\text{Ln}_2\text{NiO}_{4+\delta}$ -based electrodes and existing gaps related to fundamental and applied research aspects.

Received 19th August 2020
Accepted 6th November 2020

DOI: 10.1039/d0ta08132a

rsc.li/materials-a

^aLaboratory of Electrochemical Devices Based on Solid Oxide Proton Electrolytes, Institute of High Temperature Electrochemistry, Yekaterinburg 620137, Russia. E-mail: dmitrymedv@mail.ru

^bUral Federal University, Yekaterinburg 620002, Russia

^cDepartment of Environmental Science and Engineering, School of Resource Environment and Safety Engineering, University of South China, Hengyang 421001, China. E-mail: lei.bi@usc.edu.cn

^dCICECO – Aveiro Institute of Materials, Department of Materials and Ceramic Engineering, University of Aveiro, 3810-193 Aveiro, Portugal. E-mail: ayaremchenko@ua.pt

† Electronic supplementary information (ESI) available. See DOI: 10.1039/d0ta08132a



Artem Tarutin received his Master's Degree in Chemical Technology at the Ural Federal University in 2019. Currently he is a PhD student at the Institute of High-Temperature Electrochemistry under the supervision of Dr D. Medvedev. His current research interests relate to the preparation, characterization and application of new electrode materials with layered structures for solid oxide fuel

(SOFCs) and electrolysis (SOECs) cells, including those based on proton-conducting electrolytes.



Julia Lyagaeva received her PhD Degree in Electrochemistry at the Institute of High-Temperature Electrochemistry in 2016 (Supervisor: Dr D. Medvedev). She is a Senior Researcher in the Laboratory of Electrochemical Devices Based on Solid Oxide Proton Electrolytes at the same institute. Her research interests focus on materials science and technological aspects of new functional

materials (electrolytes, electrodes and membranes) and their application in various electrochemical cells (hydrogen sensors, fuel cells and electrolysis cells).

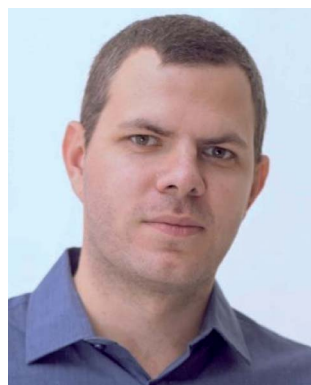
1. Introduction

The ever-increasing demand for the development of highly efficient, environmentally friendly, technologically straightforward and economically expedient energy systems has stimulated rapid progress in the hydrogen and electrochemical energy fields.^{1–4} Accordingly, research and development related to solid oxide electrochemical cells are widespread due to the higher efficiency, flexibility and variety of these cells for use in energy conversion processes compared with other electrochemical cells.^{5–7} Although conventional solid oxide electrochemical cells have some disadvantages due to their high operating temperatures, the existing problems can be overcome by replacing the oxygen-ionic conductive electrolytes with proton-conducting counterparts. The improved transfer behaviour of the latter is realised due to the greater mobility of the proton charge carriers, which also exhibit a low migration

barrier.^{8–11} Consequently, energy can be efficiently converted in solid oxide electrochemical cells based on proton-conducting electrolytes below 700 °C, and at this temperature, degradation and compatibility issues become less problematic.

Among the different types of electrochemical cells, protonic ceramic fuel cells (PCFCs) and protonic ceramic electrolysis cells (PCECs) are of special interest as systems for converting chemical energy into electricity and *vice versa*.^{12–14} These two types of operations can be combined in reversible protonic ceramic cells (rPCCs), which enable power generation or energy conversion depending on the necessary (momentary) requirements. However, although very promising performances have recently been achieved for both PCFCs and PCECs,^{15–20} their long-term operation under multiple cycles of temperature or steam and oxygen partial pressure requires further improvement. Problems associated with degradation phenomena may also occur for these systems, where instead of fast microstructural changes, cationic interdiffusion, segregation and poisoning occur at high temperatures,^{21–24} chemical and thermal incompatibilities in the electrode/electrolyte pair play a key role in maintaining the integrity of PCFCs, PCECs and rPCCs.

Although the transport properties of the corresponding electrochemical devices are regulated by a proton-conducting membrane, other functional materials also affect their target electrochemical characteristics (power density, hydrogen production rate, *etc.*). In particular, the selection of suitable oxygen electrodes is currently of great importance for fabricating low- and intermediate-temperature electrochemical systems, including PCFCs, PCECs and rPCCs.^{25–27} There is a significant number of publications on the design of suitable oxygen electrodes, as systematically detailed in the following works.^{28–31} Among the various classes of electrodes, herein, we focus on the interesting group of oxides based on lanthanide nickelates.



Dmitry Medvedev is a Leading Scientist at the Institute of High Temperature Electrochemistry (Yekaterinburg, Russia) and a Professor at the Ural Federal University (Yekaterinburg, Russia). He received his PhD degree in 2012 and Dr Habil in 2019, both in the field of high-temperature electrochemistry. His research activity deals with engineering new materials for energy conversion devices, such

as solid oxide fuel cells, solid oxide electrolysis cells, sensors, and oxygen permeable membranes. He has authored about 100 peer reviewed papers and filed 10 national patents.



Dr Lei Bi worked at the National Institute for Materials Science (NIMS) in Japan as a Postdoc after obtaining his PhD degree from the University of Science and Technology of China in 2009. Then he was appointed as a Research Scientist at King Abdullah University of Science and Technology (KAUST) in Saudi Arabia. In 2016, he joined Qingdao University as a Full Professor. His research is

focused on materials for energy and the environment. Currently, he is a Professor at the University of South China, leading a group working on solid oxide cells, particularly with proton-conducting electrolytes.



Dr Aleksey Yaremchenko is a Principal Researcher at the CICECO – Aveiro Institute of Materials, University of Aveiro, Portugal. He has been engaged in R&D in the fields of Materials Science & Engineering and Solid State Chemistry & Electrochemistry for over 20 years. The particular area of his scientific activity is electrochemical technologies and (electro)catalytic systems, including solid oxide

fuel/electrolysis cells (SOFC/SOEC) and reversible solid electrolyte cells (r-SOC), mixed-conducting ceramic membranes and membrane reactors, energy conversion and storage materials, and energy generation from renewable sources (biogas, biochar). Dr Yaremchenko has co-authored over 160 papers in SCI journals, including several reviews, with an h-index of 41.

The oxide $\text{Ln}_2\text{NiO}_{4+\delta}$ ($\text{Ln} = \text{La}, \text{Nd}, \text{and Pr}$) materials having a layered structure belong to the Ruddlesden–Popper (RP) family with the general formula $\text{A}_{n+1}\text{B}_n\text{O}_{3n+1}$, where $n \geq 1$, A is a rare-earth or alkaline-earth element and B is a transition metal.³² The properties of $\text{Ln}_2\text{NiO}_{4+\delta}$ such as excellent oxygen diffusion coupled with high surface exchange coefficients and reduced thermal expansion coefficients (TECs) have resulted in their wide application in solid oxide electrochemical cells, including that based on ZrO_2 ,^{33,34} CeO_2 ,^{35,36} and LaGaO_3 (ref. 37 and 38) oxygen-conducting electrolytes, and proton-conducting analogues. It should be noted that $\text{Ln}_2\text{NiO}_{4+\delta}$ oxides are considered to show triple-conducting behaviour when protonic transport exists simultaneously with oxygen-ionic and electronic transportation.³⁹ Since this feature can affect the target parameters of electrochemical systems based on proton-conducting electrolytes, it should be analysed in detail. Therefore, this review work is devoted to revealing the application peculiarities of nickelates in PCECs, PCFCs and rPCCs and identifying future strategies for the improvement of their efficiency and performance.

2. Structure and defect chemistry of $\text{Ln}_2\text{NiO}_{4+\delta}$

2.1. Crystal structure and oxygen nonstoichiometry

$\text{Ln}_2\text{NiO}_{4+\delta}$ nickelates belong to a series of perovskite-related layered compounds with the general formula $\text{A}_{n+1}\text{B}_n\text{O}_{3n+1}$, which are referred to as Ruddlesden–Popper (RP) phases.^{40,41} The RP structure is built of consecutive perovskite-type $(\text{ABO}_3)_n$ blocks alternating with rock-salt-type AO layers along the c crystallographic axis (Fig. 1). Its formula can be represented as $(\text{AO})(\text{ABO}_3)_n$, where n is the number of connected layers of vertex-sharing BO_6 octahedra. $\text{Ln}_2\text{NiO}_{4+\delta}$ and its derivatives are $n = 1$ members of the homologous RP-type nickelate series. Due to their structural similarities, this type of material is also referred to as K_2NiF_4 -type phases. In the stoichiometric $\text{Ln}_2^{3+}\text{Ni}^{2+}\text{O}_4^{2-}$ compounds, the A-site Ln cations positioned at the boundary of two types of layers are coordinated by 9 oxygen ions, while the B-site Ni cations are located in the center of octahedra formed by 6 oxygen anions. The NiO_6 octahedra share corners in the a - b plane, forming a 2-dimensional network.

The characteristic feature of the $\text{Ln}_2\text{NiO}_{4+\delta}$ phases is the possibility to accommodate variable oxygen excess of up to $\delta \sim 0.25$ – 0.30 in the case of $\text{Ln} = \text{La}$,^{42,43} which is required for the stabilization of the RP-type A_2BO_4 structure. The structural stability of A_2BO_4 phases is governed by the bond length matching between the perovskite and rock-salt-type layers, which can be rationalized by the Goldschmidt tolerance factor:^{41,42,44–47}

$$t = \frac{r_{\text{Ln}} + r_{\text{O}}}{\sqrt{2}(r_{\text{Ni}} + r_{\text{O}})} \quad (1)$$

where r is the ionic radii of cations and oxygen in the appropriate coordination.

Empirically, the tetragonal RP-type A_2BO_4 (or K_2NiF_4 -type) structure is stable over the approximate range of $0.85 < t <$

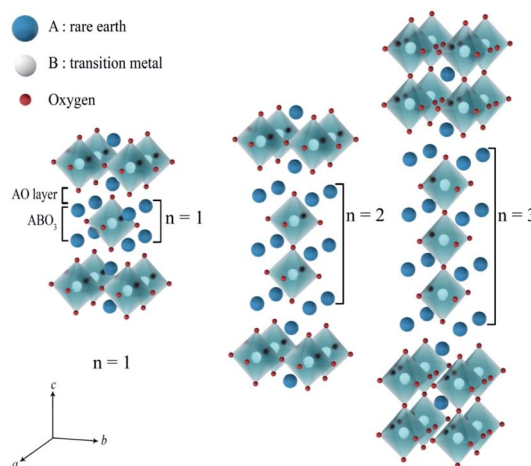
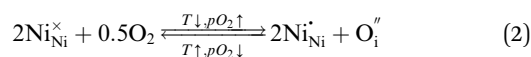


Fig. 1 Idealized representation of the crystal structures of $\text{A}_{n+1}\text{B}_n\text{O}_{3n+1}$ Ruddlesden–Popper phases.

1.00.^{41,44–46} The perfect matching of two layer types will yield a tolerance factor of $t = 1$, while any deviation in the t value implies a buildup of internal stress in the a - b plane of the crystal lattice.^{42,45,47} The ionic radii of rare-earth cations are smaller than the ideal $r_{\text{A}} \sim 1.56 \text{ \AA}$ (estimated employing Shannon's radii).⁴⁸ The calculated $t = 0.885$ in the case of stoichiometric $\text{La}_2\text{NiO}_{4+\delta}$ means that the La–O bonds are under tensile stress and the Ni–O bonds are under compressive stress. Incorporation of interstitial oxygen ions into the rock-salt-type LaO layers relaxes the structure due to several factors as follows:^{42,47,49,50} (i) an increase in the average Ln–O bond length as a result of an increase in the Ln cation coordination; (ii) electrostatic repulsion of intercalated oxygen ions, leading to the same effect; and (iii) shortening of the average Ni–O bond length due to the partial oxidation of nickel cations as a result of the following charge compensation:



with electroneutrality condition

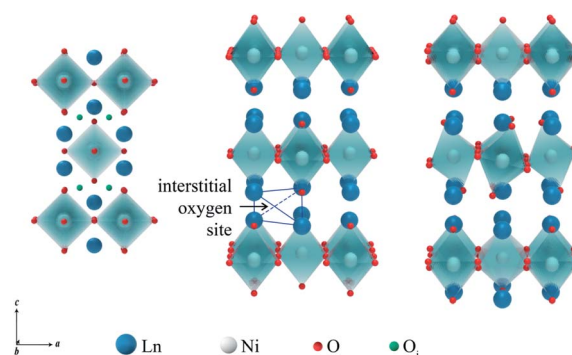


Fig. 2 Crystal structures of A_2BO_4 phases ($\text{A} = \text{Ln}$ and $\text{B} = \text{Ni}$) with tetragonal (center) and orthorhombic (right) lattice symmetry. The a - c projection of the tetragonal lattice (left) illustrates the positions of the interstitial oxygen ions.

$$[\text{Ni}'_{\text{Ni}}] = 2[\text{O}''_{\text{i}}] \quad \text{or} \quad p = 2\delta \quad (3)$$

where p is the concentration of electron holes.

Due to geometric constraints, only three rare-earth cations can form RP-type $\text{Ln}_2\text{NiO}_{4+\delta}$ compounds in the undoped form, *i.e.* lanthanum, praseodymium and neodymium. The oxygen excess, δ , in these phases reversibly decreases on heating or reducing the oxygen partial pressure as a result of oxygen release from the lattice and reduction of Ni cations *via* reverse reaction (2), but is frozen at temperatures below ~ 350 °C (ref. 51–54) due to kinetic reasons. High-temperature $p\text{O}_2$ - T - δ diagrams and their analysis can be found in ref. 55–65. At elevated temperatures, $\text{Ln}_2\text{NiO}_{4+\delta}$ has a tetragonal structure with the space group $I4/mmm$ ^{55,66,67} (Fig. 2) and interstitial oxygen ions in the $(\frac{1}{4}, \frac{1}{4}, \frac{1}{4})$ positions in the unit cell.⁶⁸ A common view is that on cooling in air, the effect of intercalation of interstitial oxygen ions becomes insufficient for the release of internal strains in the tetragonal lattice due to the different thermal expansion of the Ln–O and Ni–O bonds. Consequently, the mismatch between the bond lengths in the perovskite and rock-salt-type layers is additionally released by tilting the NiO_6 tetrahedra, leading to a symmetry reduction to orthorhombic symmetry (or even monoclinic).^{69,70} Aspera *et al.*⁷¹ suggested that increasing the concentration of interstitial oxygen in rock-salt-type LnO layers may be a major factor contributing to the change in structure: the interstitial oxygen ions repulse the neighboring apical oxygen ions in the perovskite layers, thus causing tilting of the octahedra. Different space groups have been proposed to describe the orthorhombic lattice of air-equilibrated nickelates (Fig. 2), including $Fm\bar{m}m$ ^{53,67,68,70,72–74} for $\text{La}_2\text{NiO}_{4+\delta}$, $Fm\bar{m}m$ ^{73–75} and $Bmab$ ^{72,75} for $\text{Pr}_2\text{NiO}_{4+\delta}$, and $Fm\bar{m}m$,^{72,76–78} $Abma$ ⁷⁶ and $Bmab$ ^{53,79} for $\text{Nd}_2\text{NiO}_{4+\delta}$. Although praseodymium exists in a mixed 3+/4+ oxidation state in binary PrO_x oxides under oxidizing conditions, analysis of the XANES spectra collected at 25–700 °C demonstrated that the Pr cations retain only the 3+ state in the $\text{Pr}_2\text{NiO}_{4+\delta}$ structure in air.⁸⁰

The ionic radius of the Ln^{3+} cations decreases in the sequence $\text{La} > \text{Pr} > \text{Nd}$,⁵⁰ leading to a corresponding increase in oxygen excess content necessary to compensate the structural strain under identical conditions,^{53,81–83} and also a shift of the orthorhombic–tetragonal transition to a higher temperature. For air-equilibrated $\text{Ln}_2\text{NiO}_{4+\delta}$, the reported values of δ at room temperature increase from 0.15–0.18 for $\text{Ln} = \text{La}$ ^{43,49,66,67,72,73,84,85} to 0.20–0.24 for $\text{Ln} = \text{Pr}$ ^{49,54,72,73,84} and to 0.22–0.28 for $\text{Ln} = \text{Nd}$.^{49,72,76,77,86,87} The orthorhombic-to-tetragonal transition on heating in air was reported to occur at ~ 50 – 150 °C in air-equilibrated $\text{La}_2\text{NiO}_{4+\delta}$,^{53,66,67,72,84} 420–450 °C in $\text{Pr}_2\text{NiO}_{4+\delta}$,^{49,54,72,84} and 520–620 °C in $\text{Nd}_2\text{NiO}_{4+\delta}$.^{49,53,72,76,78,86,88,89} In the case of $\text{Pr}_2\text{NiO}_{4+\delta}$ and $\text{Nd}_2\text{NiO}_{4+\delta}$, this reversible structural transformation is accompanied by a discrete change in the oxygen nonstoichiometry and occurs when δ in the orthorhombic modification is decreased to a certain level by 0.175–0.20 for $\text{Pr}_2\text{NiO}_{4+\delta}$ (ref. 54, 72 and 90) and 0.135–0.155 for $\text{Nd}_2\text{NiO}_{4+\delta}$.^{72,91} Consequently, the temperature of the transition decreases with reducing $p\text{O}_2$.^{54,72,76,88,90,91} In $\text{La}_2\text{NiO}_{4+\delta}$ ($\delta \geq 0.15$),

an orthorhombic-to-tetragonal transition occurs at reduced temperatures when oxygen exchange is kinetically frozen, but the temperature of this transition increases with an increase in the frozen-in δ value.^{55,66}

In addition to interstitial oxygen ions, oxygen defects important for transport and electrocatalytic properties include oxygen vacancies in the perovskite layers of the RP-type structure. Oxygen vacancies may form due to intrinsic Frenkel-type disorder



or as a result of modifications of the cation composition as discussed below.

2.2. A-site deficiency and $\text{Ln}_2\text{NiO}_{4+\delta}$ -based solid solutions

Similar to ABO_3 perovskites, the RP-type A_2BO_4 structure is very flexible to the introduction of A-site cation deficiency and various substitutions in both sublattices, with effects on structural properties, oxygen nonstoichiometry, ionic and electronic transport, electrocatalytic activity, and other relevant properties. The reported solubility of selected cations in the A and B sublattices of $\text{Ln}_2\text{NiO}_{4+\delta}$ is summarized in Table 1. However, the existing range of $\text{Ln}_2\text{NiO}_{4+\delta}$ -based solid solutions is not limited to individual doping in the Ln or Ni sites, but also includes a variety of co-substitutions in one or both sublattices.

2.2.1. A-site cation deficiency. Available literature data indicates that the $\text{Ln}_2\text{NiO}_{4+\delta}$ structure can tolerate a certain concentration of cation vacancies in the Ln sublattice. The formation of $\text{Ln}_{2-x}\text{NiO}_{4\pm\delta}$ solid solutions was reported up to $x = 0.15$ for $\text{Ln} = \text{La}$,^{51,85,122–124} $x = 0.30$ for $\text{Ln} = \text{Pr}$,^{75,92} and $x = 0.10$ for $\text{Ln} = \text{Nd}$,^{53,87,125,126} although a detailed phase and structural analysis was not always provided. Formation of A-site deficient nickelates may also be affected by the employed synthetic procedure. In particular, the presence of phase impurities was reported for $\text{La}_{2-x}\text{NiO}_{4+\delta}$ ($x \geq 0.02$ – 0.03)^{127,128} and $\text{Pr}_{2-x}\text{NiO}_{4+\delta}$ ($x = 0.10$ and 0.20).⁷⁵

An increase in the concentration of Ln vacancies was reported to gradually decrease the oxygen hyperstoichiometry in the lattice,^{51,75,85,87,126} eventually leading to oxygen deficiency even in air.^{51,53} However, room-temperature neutron diffraction studies of $\text{Pr}_{2-x}\text{NiO}_{4+\delta}$ demonstrated that an increase in praseodymium deficiency results in an increase in the concentration of oxygen vacancies in the perovskite layer, in the equatorial and, preferentially, apical positions, while the concentration of interstitial oxygen remains essentially unchanged.⁷⁵ Thus, the introduction of cation vacancies into the A-sublattice of $\text{Ln}_2\text{NiO}_{4+\delta}$ is charge compensated preferentially by the formation of oxygen vacancies, implying the importance of Frenkel disorder in these phases, and the full electroneutrality condition can be expressed as

$$3[\text{V}'''_{\text{Ln}}] + 2[\text{O}''_{\text{i}}] = [\text{Ni}'_{\text{Ni}}] + 2[\text{V}''_{\text{O}}] \quad \text{or} \quad p = 3x + 2\delta, \quad (5)$$

where $\delta = [\text{O}''_{\text{i}}] - [\text{V}''_{\text{O}}]$, and V'''_{Ln} denotes Ln vacancy.

2.2.2. Mutual solubility. The full range of solid solutions was reported to exist in $\text{La}_2\text{NiO}_{4+\delta}$ – $\text{Pr}_2\text{NiO}_{4+\delta}$,^{73,83,93,129} $\text{La}_2\text{NiO}_{4+\delta}$ – $\text{Nd}_2\text{NiO}_{4+\delta}$,⁸⁹ and $\text{Pr}_2\text{NiO}_{4+\delta}$ – $\text{Nd}_2\text{NiO}_{4+\delta}$ (ref. 74 and

Table 1 Reported solubility of substituting cations in the A- and B-sublattices of $\text{Ln}_2\text{NiO}_{4+\delta}$ under oxidizing conditions^a

$\text{Ln}_{2-x}\text{A}_x\text{NiO}_{4\pm\delta}$	Ln = La		Ln = Pr		Ln = Nd	
	x	Ref.	x	Ref.	x	Ref.
V''_{Ln}	0.15 (<i>max</i>)	51	0.30	92	0.10	53
La	—	—	2.0	73, 83 and 93	2.0	89
Pr	2.0	73, 83 and 93	—	—	2.0	74 and 94–96
Nd	2.0	89	2.0	74 and 94–96	—	—
Sm	1.1	97	—	—	—	—
Ca	0.6 (<i>max</i>)	98	0.7	101	0.6 (<i>max</i>)	79
	$0.3 < x_{(\text{max})} < 0.4$	99 and 100	0.5 (<i>max</i>)	102	0.5 (<i>max</i>)	78
					1.0	103
Sr	1.6 (<i>max</i>)	104 and 105	1.6	106 and 107	1.6	108
	1.5 (<i>max</i>)	98	—	—	1.67	104
Ba	1.0	109	0.4	110	0.6 (<i>max</i>)	79
	1.1 (<i>max</i>)	98	—	—	—	—

$\text{Ln}_2\text{Ni}_{1-y}\text{M}_y\text{O}_{4+\delta}$	Ln = La		Ln = Pr		Ln = Nd	
	y	Ref.	y	Ref.	y	Ref.
Cu	1.0	111–114	0.4 (<i>max</i>)	111	0.3 (<i>max</i>)	115 and 116
			0.5	45		
Co	0.20 (<i>max</i>)	97 and 117	0.1	118	0.1	119
Fe	0.10	120 and 121	0.1	52	0.1	119
Mn					~0.1	119

^a “Max” indicates the identified solubility limit in a given report.

96) pseudobinary systems, which is expected considering the structural identity between the parent materials. Changing the fractions of two Ln cations in the A sublattice leads to a gradual change in the structural properties, oxygen nonstoichiometry and temperature of the orthorhombic-to-tetragonal transition on heating, in agreement with the properties of individual $\text{Ln}_2\text{NiO}_{4+\delta}$ compounds. In the case of $\text{La}_{2-x}\text{Pr}_x\text{NiO}_{4+\delta}$ solid solutions, the oxygen nonstoichiometry, δ , at temperatures above ~ 400 °C was observed to exhibit a rather weak dependence on the praseodymium content up to $x \sim 1.5$, and then decreased rapidly.^{93,129} Contrary to other studies, Vibhu *et al.*⁷⁰ recently reported the existence of a biphasic region in the $\text{La}_{2-x}\text{Pr}_x\text{NiO}_{4+\delta}$ system at $x = 0.5$ – 1.0 based on room-temperature high-resolution synchrotron and neutron powder diffraction data.

2.2.3. A-site substitutions by alkaline-earth cations. RP-type nickelates form a wide range of $\text{Ln}_{2-x}\text{A}_x\text{NiO}_{4+\delta}$ solid solutions, where $\text{A} = \text{Ca},$ ^{53,78,79,99–102,109,130–132} Sr ^{56–58,79,83,105,106,108,109,133–149} or $\text{Ba}.$ ^{79,98,109,110} As a common effect, an increase in x results in a gradual decrease in oxygen content from excess ($x \leq 0.3$ – 0.4) to oxygen stoichiometry ($\delta \approx 0$ for intermediate x) and eventually to oxygen deficiency ($x \geq 1.0$). This is accompanied by a decrease in the orthorhombic-to-tetragonal transition temperature (below room temperature for $x \geq 0.1$ – 0.3),^{78,79,101,102,110,130,132,141,143,144,146,147,149,150} a gradual increase in Ni^{3+} concentration,^{57,83,98,105,134,136,151} and even the formation of Ni cations in the formal 4+ oxidation state for A-rich compositions.^{98,105,108,145,152} Thus, acceptor-type doping by

alkaline-earth cations is charge compensated by a decrease in interstitial oxygen concentration and the formation of electron holes and oxygen vacancies (Fig. 3). The full electroneutrality condition is given by

$$[\text{A}'_{\text{Ln}}] + 2[\text{O}''_{\text{i}}] = [\text{Ni}'_{\text{Ni}}] + 2[\text{Ni}''_{\text{Ni}}] + 2[\text{V}''_{\text{O}}] \quad \text{or} \quad p = x + 2\delta \quad (6)$$

where $p = [\text{Ni}'_{\text{Ni}}] + 2[\text{Ni}''_{\text{Ni}}]$, $\delta = [\text{O}''_{\text{i}}] - [\text{V}''_{\text{O}}]$, and O''_{i} and V''_{O} prevail for small and large A-cation fractions, respectively.

The solubility of alkaline-earth cations decreases in the sequence $\text{Ca} < \text{Ba} < \text{Sr}$ (Table 1), in agreement with considerations of the tolerance factor, t , (eqn (1)) and stability of the A_2BO_4 structure.⁹⁸ Sr^{2+} has a slightly higher ionic radius than that of Ln^{3+} (coordination number of A-site cations in the idealized Ln_2NiO_4 structure is 9).⁴⁸ Therefore, the incorporation of strontium into the Ln sites effectively releases the tensile stress in the Ln–O bonds, and Sr cations may occupy up to $\sim 5/6$ sites in the A sublattice of $\text{Ln}_{2-x}\text{A}_x\text{NiO}_{4+\delta}$. The ionic radius of Ca^{2+} is between that of La^{3+} and Nd^{3+} and is similar to the ionic radius of Pr^{3+} (ref. 50), thus having the opposite, but comparatively small steric effect on the RP lattice for different Ln. In combination with the shortening of the Ni–O bond lengths due to gradual $\text{Ni}^{2+} \rightarrow \text{Ni}^{3+}$ oxidation, this results in the comparatively limited solubility of calcium in the A-sublattice. Finally, large Ba^{2+} cations⁴⁸ are even more effective than Sr^{2+} for releasing the tensile stress in the rock-salt-type layers; however, the tolerance factor reaches the upper limit of $t = 1$ at a lower concentration compared to the Sr-substituted counterparts.

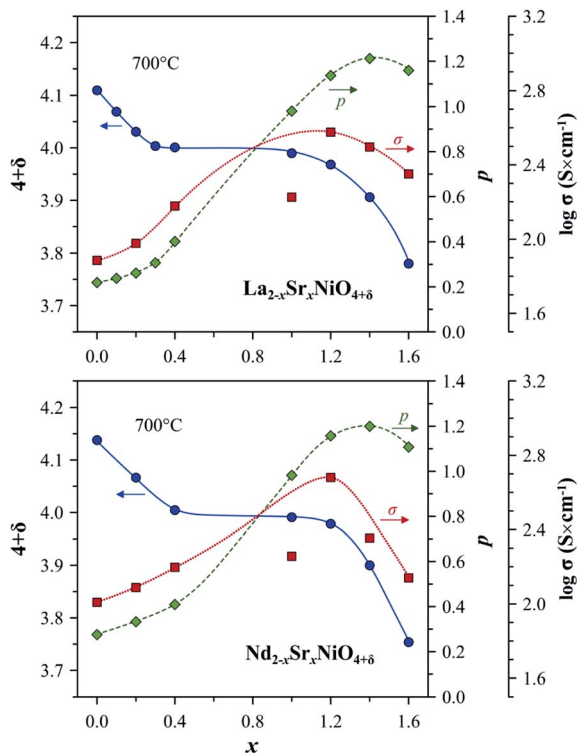


Fig. 3 Trends in the variation of oxygen nonstoichiometry $4 + \delta$, electron-hole concentration, p , and electrical conductivity, σ , with strontium content, x , in $\text{Ln}_{2-x}\text{Sr}_x\text{NiO}_{4+\delta}$ systems at 700 °C. The experimental data on oxygen nonstoichiometry and electrical conductivity are from ref. 56, 59, 108, 142, 145 and 148. The electron-hole concentration is calculated using eqn (6). Note that σ of the Sr-rich compositions is undervalued due to the porosity of samples and microcracking effects.^{108,145}

The level of A-site doping and, consequently, the level of oxygen content has an impact on the variations of oxygen nonstoichiometry with temperature and $p\text{O}_2$ within the phase stability domain of RP-type $\text{Ln}_{2-x}\text{A}_x\text{NiO}_{4+\delta}$ phases at temperatures above ~ 400 °C as follows:^{56–59,81,106,108,131,139,140,142,145,153–155}

(i) *Oxygen-hyperstoichiometric phases ($\delta > 0$ in air)*. These compositions behave similarly to the parent nickelates. The oxygen content decreases on heating and with a reduction in oxygen partial pressure, but the materials maintain oxygen excess.

(ii) *Oxygen-stoichiometric and nearly stoichiometric phases ($\delta \sim 0$ in air)*. These materials demonstrate negligible δ variations upon thermal and $p\text{O}_2$ cycling under oxidizing conditions, but tend to exhibit moderate temperature-dependent oxygen deficiency at reduced oxygen pressures. Specifically, increasing x suppresses the formation of interstitial oxygen under oxidizing conditions and promotes the formation of oxygen vacancies under reducing conditions.

(iii) *Oxygen-deficient solid solutions ($\delta < 0$ in air)*. Oxygen deficiency increases on heating and with a decrease in oxygen partial pressure. These phases tend to exhibit a structural transformation to a distorted orthorhombic structure (space group *Immm*) under moderately reducing conditions (e.g. $p\text{O}_2 \sim$

10^{-5} atm) accompanied by ordering in the oxygen sublattice and substantial dimensional changes.^{108,155} Besides, A-rich phases exhibit strongly anisotropic thermochemical expansion, which complicates high-temperature ceramic processing.^{108,138,145}

2.2.4. B-site substitutions by transition metal cations. The formation of a full range of solid solutions with orthorhombic or tetragonal structure was reported for the $\text{La}_2\text{NiO}_{4+\delta}$ – $\text{La}_2\text{CuO}_{4+\delta}$ pseudobinary system.^{111–114,156} Due to the stable 2+ oxidation state of the copper cations under oxidizing conditions, increasing y in $\text{La}_2\text{Ni}_{1-y}\text{Cu}_y\text{O}_{4+\delta}$ results in a gradual decrease in oxygen excess in the lattice,^{113,156,157} down to $\delta \leq 0.01$ for $y = 0.4$ – 0.8 at room temperature.¹⁵⁶ Since Cu^{2+} has a larger ionic radius than that of Ni^{2+} (coordination number of B-site cations in the idealized Ln_2NiO_4 structure is 6),⁴⁸ increasing the B–O bond length and a decrease in δ as a result of Cu substitution decrease the tolerance factor¹¹¹ and destabilize the RP-type A_2BO_4 structure. This leads to the limited solubility of the copper cations in the nickel sublattice of praseodymium and neodymium nickelates, i.e. $y = 0.4$ – 0.5 for $\text{Pr}_2\text{Ni}_{1-y}\text{Cu}_y\text{O}_{4+\delta}$ (ref. 45, 111, 158 and 159) and $y = 0.3$ for $\text{Nd}_2\text{Ni}_{1-y}\text{Cu}_y\text{O}_{4+\delta}$.^{87,115,116}

Other transition metal cations (such as Co, Fe, Mn, Cr, and Ti) tend to exhibit higher oxidation states in oxide compounds under oxidizing conditions, and therefore have very limited (if any) solubility in the nickel sublattice of $\text{Ln}_2\text{NiO}_{4+\delta}$. The solid solubility range of cobalt in $\text{La}_2\text{Ni}_{1-y}\text{Co}_y\text{O}_{4+\delta}$ was found to be limited to $y = 0.2$ in air,^{97,117,160} although it can be extended under reducing conditions.^{97,117} The confirmed solubility of cobalt cations in $\text{Ln}_2\text{Ni}_{1-y}\text{Co}_y\text{O}_{4+\delta}$ ($\text{Ln} = \text{Pr}$ and Nd) and iron cations in $\text{Ln}_2\text{Ni}_{1-y}\text{Fe}_y\text{O}_{4+\delta}$ ($\text{Ln} = \text{La}$, Pr , and Nd) is only 10 at%.^{52,60,118–121,161} Miyoshi *et al.*¹⁶² reported the results of oxygen permeation studies of $\text{La}_2\text{Ni}_{0.8}\text{Fe}_{0.2}\text{O}_{4+\delta}$ and $\text{Pr}_2\text{Ni}_{0.8}\text{M}_{0.2}\text{O}_{4+\delta}$ ($\text{M} = \text{Co}$, Fe , and Mn), but did not present a detailed analysis of the XRD data, and thus their phase purity is questionable. Phase impurities were detected in the XRD patterns of $\text{Nd}_2\text{Ni}_{0.9}\text{Mn}_{0.1}\text{O}_{4+\delta}$,¹¹⁹ $\text{La}_2\text{Ni}_{0.9}\text{M}_{0.1}\text{O}_{4+\delta}$ ($\text{M} = \text{Ta}$ and V),^{163,164} and $\text{La}_2\text{Ni}_{1-y}\text{Mo}_y\text{O}_{4+\delta}$ ($y = 0.0125$ – 0.05).¹⁶⁵

The impact of partial substitution of nickel by cobalt or iron in $\text{Ln}_2\text{NiO}_{4+\delta}$ in terms of defect chemistry is an increase in the concentration of interstitial oxygen and electron holes.^{60–62,97,120,121,160,161} The corresponding electroneutrality condition is

$$[\text{Ni}'_{\text{Ni}}] + [\text{M}'_{\text{Ni}}] = 2[\text{O}''_{\text{i}}] \quad \text{or} \quad p = 2\delta, \quad (7)$$

where $p = [\text{Ni}'_{\text{Ni}}] + [\text{M}'_{\text{Ni}}]$.

In the $\text{La}_2\text{Ni}_{0.9}\text{M}_{0.1}\text{O}_{4+\delta}$ series, δ was found to increase in the sequence $\text{M} = \text{Cu} < \text{Ni} < \text{Co} < \text{Fe}$.^{61,62,65,120,121} A similar tendency was observed for B-site-doped $\text{Pr}_2\text{NiO}_{4+\delta}$.⁵²

The solid solubility of transition metal cations in the nickel sublattice of $\text{Ln}_2\text{NiO}_{4+\delta}$ under oxidizing conditions can be substantially expanded by co-substitutions with alkaline earth-cations into the Ln sublattice. In that case, donor-type doping into the B sublattice is partially charge-compensated by acceptor-type doping in the A sublattice. This leads to a complex interplay between the cation composition, oxygen

nonstoichiometry, transport and electrochemical properties. The reported examples of co-substitutions include $\text{La}_{2-x}\text{Sr}_x\text{Ni}_{1-y}\text{M}_y\text{O}_{4+\delta}$ ($M = \text{Co}, \text{Fe}, \text{Mn}, \text{Ti}, \text{and Mo}$),^{45,165–174} $\text{La}_{2-x}\text{Ca}_x\text{Ni}_{1-y}\text{M}_y\text{O}_{4+\delta}$ ($M = \text{Fe}$),¹³¹ $\text{Nd}_{2-x}\text{Sr}_x\text{Ni}_{1-y}\text{M}_y\text{O}_{4+\delta}$ ($M = \text{Cu and Co}$),^{175,176} and $\text{Pr}_{2-x}\text{Sr}_x\text{Ni}_{1-y}\text{M}_y\text{O}_{4+\delta}$ ($M = \text{Co}, \text{Mn}$).^{177,178} The solubility of the transition metal typically increases with an increase in the fraction of alkaline-earth cation in the A-sublattice, and in the case of Co or Fe, may reach the entire range of B-site concentrations.^{170,172,174–176}

The synthesis of Cr-doped $(\text{Ln}, \text{A})_2\text{Ni}_{1-y}\text{Cr}_y\text{O}_{4+\delta}$ (A – alkaline-earth cation) is only possible at reduced oxygen pressures, under an argon atmosphere.^{179–184} As an exception, Ishihara *et al.*¹⁸⁵ reported the preparation of $\text{Pr}_2\text{Ni}_{0.75}\text{Cu}_{0.20}\text{M}_{0.05}\text{O}_{4+\delta}$ ($M = \text{Cr and V}$) in air, but without accurate structural studies.

2.2.5. B-site substitutions by other metal cations. The data on other B-site substitutions are rather scarce, and in many cases, accurate analysis of the phase composition and structural data are not available.

Ye and Hertz¹⁸⁶ reported that Mg^{2+} can substitute into the nickel sublattice up to $y = 0.3$ in $\text{La}_2\text{Ni}_{1-y}\text{Mg}_y\text{O}_{4+\delta}$ and $y = 0.2$ in $\text{La}_{1.85}\text{Ni}_{1-y}\text{Mg}_y\text{O}_{4+\delta}$, and that the solubility can be further extended by strontium co-substitution into the lanthanum sublattice. Zhang *et al.*³⁸ confirmed that $\text{La}_2\text{Ni}_{1-y}\text{Mg}_y\text{O}_{4+\delta}$ is formed at least in the range $0 \leq y \leq 0.1$. The formation of $\text{La}_{1.7}\text{Sr}_{0.3}\text{Ni}_{1-y}\text{Mg}_y\text{O}_{4+\delta}$ ($y = 0–0.5$) was reported by Meeporn *et al.*¹⁸⁷ On the other hand, Klande *et al.*¹⁶³ failed to prepare single-phase $\text{La}_2\text{Ni}_{0.9}\text{Mg}_{0.1}\text{O}_{4+\delta}$.

Ganguli *et al.*¹²³ reported the formation of Zn-substituted $\text{La}_{1.9}\text{Ni}_{0.9}\text{Zn}_{0.1}\text{O}_{4+\delta}$ and $\text{La}_{1.9}\text{Sr}_{0.1}\text{Ni}_{0.9}\text{Zn}_{0.1}\text{O}_{4+\delta}$, while Silva *et al.*¹⁸⁸ claimed the zinc solubility of up to 40 at% in the nickel sublattice.

The confirmed solubility of aluminum in $\text{La}_2\text{Ni}_{1-y}\text{Al}_y\text{O}_{4+\delta}$ corresponds to 5 at% in the nickel sublattice,^{189,190} while $\text{La}_2\text{Ni}_{0.9}\text{Al}_{0.1}\text{O}_{4+\delta}$ was reported to comprise of secondary phases.¹⁶³ Surprisingly, donor-type doping by Al^{3+} was found to reduce the oxygen excess in $\text{La}_2\text{Ni}_{0.95}\text{Al}_{0.05}\text{O}_{4+\delta}$ compared to the parent nickelate.¹⁸⁹

The formation of the full range of $\text{LaSrNi}_{1-y}\text{Ga}_y\text{O}_{4\pm\delta}$ ($y = 0–1.0$) solid solutions with a tetragonal structure was reported by Reinen *et al.*,¹⁹¹ whereas the solid solubility of scandium in $\text{LaSrNi}_{1-y}\text{Sc}_y\text{O}_{4+\delta}$ was found to be limited to $y = 0.2$.¹⁹² Zhang *et al.*¹⁹³ also reported the formation of single-phase $\text{La}_{1.9}\text{Ni}_{0.45}\text{Cu}_{0.45}\text{Sc}_{0.1}\text{O}_{4\pm\delta}$.

The synthesis of $\text{La}_2\text{Ni}_{0.9}\text{Zr}_{0.1}\text{O}_{4+\delta}$ was attempted in ref. 163 but the product contained $\text{La}_2\text{Zr}_2\text{O}_7$ impurity.

The membrane screening tests by Miyoshi *et al.*¹⁶² included oxygen permeation studies of $\text{Pr}_2\text{Ni}_{0.8}\text{Zn}_{0.2}\text{O}_{4+\delta}$ and $\text{Pr}_2\text{Ni}_{0.9}\text{M}_{0.1}\text{O}_{4+\delta}$ ($M = \text{Mg}, \text{Al}, \text{and Ga}$), but the reported information is insufficient to conclude about the phase purity of the samples. A number of works focused on investigating the oxygen permeability or electrochemical properties of co-substituted phases in the $(\text{Ln}_{1-x}\text{A}_x)_{2-a}\text{Ni}_{1-y-z}\text{Cu}_z\text{M}_y\text{O}_{4+\delta}$ ($\text{Ln} = \text{Pr or Nd}$; $\text{A} = \text{La or Sr}$; $\text{M} = \text{Al}, \text{Ga}, \text{In}, \text{Zr}$; $x = 0–1.0$, $a = 0–0.10$, $y = 0–0.10$)^{185,194–200} series. The compositions were claimed to be phase-pure or to contain minor phase impurities, which were ignored. In most cases, again, the quality of the

provided XRD data is not sufficient to accurately conclude about the solid solubility limits of the dopant cations M.

2.2.6. $\text{Sm}_2\text{NiO}_{4+\delta}$ -based solid solutions. As mentioned above, undoped $\text{Ln}_2\text{NiO}_{4+\delta}$ exists only for $\text{Ln} = \text{La}, \text{Pr and Nd}$.¹⁰⁴ Sm^{3+} cations are too small to form the $\text{Sm}_2\text{NiO}_{4+\delta}$ compound. However, the formation of $\text{Sm}_2\text{NiO}_{4+\delta}$ -based solid solutions is possible if an appropriate larger cation is incorporated into the Sm sublattice to increase the tolerance factor.

$\text{Sm}_{2-x}\text{La}_x\text{NiO}_{4+\delta}$ solid solutions with a tetragonal structure were reported to form in the concentration range of $0.9 \leq x \leq 2.0$.⁹⁷ Changing the lanthanum content was observed to have a negligible impact on the low-temperature oxygen nonstoichiometry: for all the compositions, δ varied between 0.11 and 0.13 at room temperature.

$\text{Sm}_{2-x}\text{Sr}_x\text{NiO}_{4+\delta}$ solid solutions exist in a wide range of strontium contents from $x = 0.4–0.5$ up to $x = 1.67$ (*i.e.* 5/6 sites in the Sm sublattice).^{104,143,201–204} As in the case of other Ln series, increasing the Sr content decreases the temperature of the orthorhombic-to-tetragonal transition. At room temperature, the structure changes from orthorhombic for $x = 0.5–0.7$ to tetragonal for $x = 0.8–1.67$.^{104,143,204} Under these conditions, $\text{Sm}_{2-x}\text{Sr}_x\text{NiO}_{4+\delta}$ is nearly oxygen-stoichiometric for $x = 0.5–1.0$ and tends to exhibit oxygen deficiency at higher Sr concentrations, while the average Ni oxidation state increases monotonically with x .²⁰²

2.2.7. Modifications of the oxygen sublattice. Doping into the oxygen sublattice of $\text{Ln}_2\text{NiO}_{4+\delta}$ remains an unexplored area, although additional anionic defects certainly may affect the crystal structure, defect chemistry and transport properties. Only a few studies can be found on this topic. Bhat *et al.*²⁰⁵ attempted fluorination of oxygen stoichiometric La_2NiO_4 at 150 °C. They found that the amount of fluorine entering the bulk of the samples is small, but results in a transformation from orthorhombic to tetragonal structure. Elongation along the *c*-axis upon fluorination was interpreted as the incorporation of interstitial species. Arbuckle *et al.*²⁰⁶ prepared fluorinated $\text{Nd}_{2-x}\text{Sr}_x\text{NiO}_{4+\delta}\text{F}_y$ ($x = 0, 0.5, \text{and } 1.0$) with the fluorine content changing from $y \sim 0.018$ for $x = 0$ to $y \sim 0.08$ for $x = 1.0$. Fluorination was observed to have an impact on the crystal lattice parameters. Contrary to $\text{Nd}_2\text{NiO}_{4+\delta}$, the fluorinated counterpart showed no evidence of phase transition in the temperature range of up to 700 °C (upper limit of thermal stability of the prepared materials). Tarutin *et al.*²⁰⁷ reported the synthesis and characterization of $\text{Nd}_{1.9}\text{Ba}_{0.1}\text{NiO}_{4+\delta}\text{F}_\gamma$ ($\gamma = 0–0.10$) solid solutions with an orthorhombic structure. The incorporation of fluorine was found to have only a minor effect on the structural parameters but results in a gradual decrease of oxygen content in the lattice, whereas the overall anion content ($4 + \delta + \gamma$) remained nearly constant. Wissel *et al.*²⁰⁸ prepared and characterized the $\text{La}_2\text{NiO}_3\text{F}_2$ composition derived from the polymer-based fluorination of the $\text{La}_2\text{NiO}_{4+\delta}$ parent phase. The XRD technique combined with ¹⁹F magic-angle spinning NMR spectroscopy allowed the localization of the fluorine ions to be determined. Particularly, it was found that the fluoride ions occupied the apical anion sites, whereas the oxide ions are located in the interstitial sites. Nowroozi *et al.*²⁰⁹ studied a fluorine-containing nickelate for utilization in all-solid-state

fluoride ion batteries (FIB). They demonstrated that $\text{La}_2\text{NiO}_{4+\delta}$ ($\delta = 0.13$) can accumulate a large amount of fluorine ions during FIB charging at 170 °C, with the formation of highly-fluorinated $\text{La}_2\text{NiO}_{4.13}\text{F}_{1.59}$ with nearly full occupation of the interstitial sites in the rock-salt-type layers by anions. The latter phase has an orthorhombic structure (space group $Fmmm$) with a unit cell significantly elongated along the c -axis ($c \sim 15.2$ Å compared to $c \sim 12.7$ Å for $\text{La}_2\text{NiO}_{4+\delta}$), confirming the incorporation of fluorine ions into the interstitial sites.

3. Thermodynamic and chemical stability of $\text{Ln}_2\text{NiO}_{4+\delta}$

The thermal stability of the phases in the pseudobinary La_2O_3 – NiO system (Fig. 4) increases in the sequence $\text{LaNiO}_{3-\delta} < \text{La}_4\text{Ni}_3\text{O}_{10-\delta} < \text{La}_3\text{Ni}_2\text{O}_{7-\delta} < \text{La}_2\text{NiO}_{4+\delta}$,^{210,215–217} consistent with the reduction in the average oxidation state of the Ni cations from 3+ for LaNiO_3 to 2+ for La_2NiO_4 . $\text{La}_2\text{NiO}_{4+\delta}$ is the only stable compound in this system at atmospheric oxygen pressure at temperatures above ~ 1250 °C (ref. 210 and 215–217) and exists up to the melting point of 1670–1750 °C.²¹⁰ Although $\text{La}_2\text{NiO}_{4+\delta}$ easily forms in air, and once formed can maintain a phase-pure state at different temperatures, RP-type $\text{La}_{n+1}\text{Ni}_n\text{O}_{3n+1}$ ($n = 2$ or 3) and perovskite-like $\text{LaNiO}_{3-\delta}$ appear to be thermodynamically more favorable at temperatures below 900–1100 °C under ambient $p\text{O}_2$. The corresponding $p\text{O}_2$ – T stability ranges can be found in available phase diagrams.^{210,216,217} However, the transformation of $\text{La}_2\text{NiO}_{4+\delta}$ into other La–Ni–O phases at temperatures below 1100 °C is kinetically suppressed.^{211,217} While it can be promoted by thermal treatments at elevated oxygen pressures (>150 bar) at 825–850 °C,^{156,216} no evidence of phase decomposition can be observed after heating $\text{La}_2\text{NiO}_{4+\delta}$ for 100 h in ambient air at different temperatures in the range of 600–1100 °C.²¹ However, Amow *et al.*^{97,218} demonstrated that $\text{La}_2\text{NiO}_{4+\delta}$ does undergo phase decomposition during a longer term: the formation of a secondary phase (presumably $\text{La}_3\text{Ni}_2\text{O}_{7-\delta}$) was detected after heating at 900 °C for two weeks in air. Later, Gauquelin *et al.*²¹⁹ observed the segregation of nickel-rich $\text{La}_4\text{Ni}_3\text{O}_{10-\delta}$ and $\text{La}_3\text{Ni}_2\text{O}_{7-\delta}$ phases on the surface of $\text{La}_2\text{NiO}_{4+\delta}$ single crystals after annealing in air at 1000 °C for 13 days. Furthermore, it was

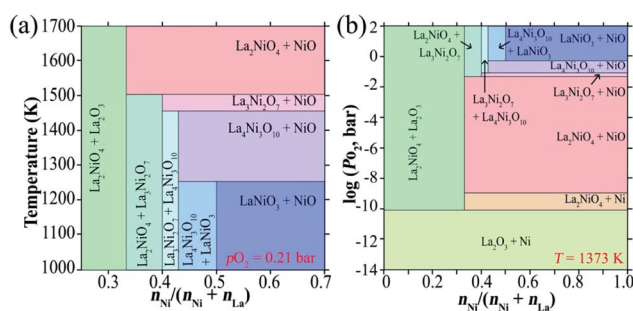


Fig. 4 T - (a) and $p\text{O}_2$ - (b) based phase diagrams in the NiO – $\text{LaO}_{1.5}$ oxide systems. Reproduced with permission.²¹⁰ Copyright 2004, Elsevier.

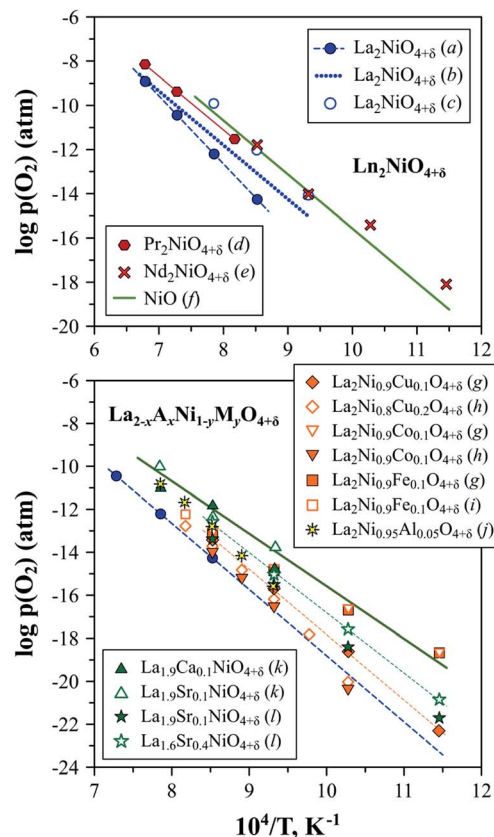


Fig. 5 Low- $p\text{O}_2$ stability boundaries of $\text{Ln}_2\text{NiO}_{4+\delta}$ and $\text{La}_{2-x}\text{A}_x\text{Ni}_{1-y}\text{M}_y\text{O}_{4+\delta}$ nickelates. Literature sources: (a) ref. 212, (b) ref. 211, (c) ref. 63, (d) ref. 222, (e) ref. 58, (f) ref. 223, (g) ref. 120, (h) ref. 214, (i) ref. 121, (j) ref. 189, (k) ref. 153 and (l) ref. 56.

found that the decomposition of $\text{La}_2\text{NiO}_{4+\delta}$ into higher-order RP-type nickelates is catalyzed and strongly facilitated by contact with Pt at temperatures ≥ 800 °C,^{220,221} thus raising concerns about the impact of Pt current collectors on the results of electrochemical studies of $\text{La}_2\text{NiO}_{4+\delta}$ -based electrodes. No such an effect was observed in contact with Au current collectors under similar conditions.²²⁰

The stability boundary of $\text{La}_2\text{NiO}_{4+\delta}$ at reduced oxygen partial pressures at 600–1300 °C was determined in ref. 56, 211 and 212 and corresponds to $p\text{O}_2 \sim 10^{-17}$ – 10^{-15} atm at 800 °C (Fig. 5). A decrease in oxygen chemical potential below this boundary results in a reduction to La_2O_3 and metallic Ni. Moderate substitutions (5–20 at%) in the B-sublattice by other transition metal cations (Fe, Co, and Cu)^{120,121,213,214} or aluminum¹⁸⁹ have a rather minor effect of the low- $p\text{O}_2$ stability limits at 600–1000 °C (Fig. 5). Nakamura *et al.*⁵⁶ studied the $\text{La}_{2-x}\text{Sr}_x\text{NiO}_{4\pm\delta}$ ($x = 0$ –0.4) system at 600–900 °C and observed only a slight shift in the low- $p(\text{O}_2)$ stability boundary towards more oxidizing conditions caused by Sr doping for $x = 0.2$ –0.4. Similar results were obtained by Kim *et al.*¹⁵³ for $\text{La}_{1.9}\text{Sr}_{0.1}\text{NiO}_{4+\delta}$ and $\text{La}_{0.9}\text{Ca}_{0.1}\text{NiO}_{4+\delta}$ at 800–1000 °C.

No information on the possible instability of $\text{Nd}_2\text{NiO}_{4+\delta}$ under oxidizing conditions can be found in the literature. Petrov *et al.*²¹¹ indicated that the low- $p\text{O}_2$ stability limits of

$\text{Nd}_2\text{NiO}_{4+\delta}$ are close to the NiO/Ni boundary. Later, Nakamura *et al.*⁵⁸ evaluated the $\text{Nd}_{2-x}\text{Sr}_x\text{NiO}_{4+\delta}$ ($x = 0-0.4$) system at 600–900 °C and confirmed that the stability boundary of undoped $\text{Nd}_2\text{NiO}_{4+\delta}$ is close to that of nickel oxide (Fig. 5), and, similar to the $\text{La}_{2-x}\text{Sr}_x\text{NiO}_{4+\delta}$ system, the substitution of Nd by Sr has no substantial effect on the stability limits under reduced oxygen pressures.

Thus, electrode materials derived from $\text{Ln}_2\text{NiO}_{4+\delta}$ ($\text{Ln} = \text{La}$ or Nd) can be expected to remain tolerant towards reductive decomposition under the typical conditions of oxygen electrode operation, even under very high cathodic polarisation.

The low- $p(\text{O}_2)$ stability boundary of $\text{Pr}_2\text{NiO}_{4+\delta}$ (Fig. 5) is between that of $\text{La}_2\text{NiO}_{4+\delta}$ and $\text{Nd}_2\text{NiO}_{4+\delta}$,²²² while partial substitutions in the nickel sublattice were reported to shift the stability limits of $\text{Pr}_2\text{Ni}_{0.9}\text{Fe}_{0.1}\text{O}_{4+\delta}$ and $\text{Pr}_2\text{Ni}_{0.8}\text{Cu}_{0.2}\text{O}_{4+\delta}$ to more oxidising conditions.⁵² Contrary to its La- and Nd-based counterparts, the $\text{Pr}_2\text{NiO}_{4+\delta}$ phase easily decomposes in the high- $p(\text{O}_2)$ region. Sullivan *et al.*²²² were the first to show that $\text{Pr}_2\text{NiO}_{4+\delta}$ undergoes a transformation into Ruddlesden–Popper $\text{Pr}_4\text{Ni}_3\text{O}_{10\pm\delta}$ and PrO_y when exposed to oxidising conditions below a certain temperature (*e.g.* below ~ 1030 °C in pure oxygen) (Fig. 6). The instability of the $\text{Pr}_2\text{NiO}_{4+\delta}$ lattice at higher oxygen pressures was confirmed and assessed in more detail in subsequent studies.^{52,75,224–229} $\text{Pr}_2\text{NiO}_{4+\delta}$, which is stable in air at $T \geq 925$ °C, can be rapidly quenched down to low temperatures.^{52,225} Thermal treatments at $T \leq 900$ °C result in a reversible decomposition into a mixture of praseodymium oxide PrO_y , Ruddlesden–Popper $\text{Pr}_4\text{Ni}_3\text{O}_{10\pm\delta}$ and perovskite-like PrNiO_3 . Ruddlesden–Popper $\text{Pr}_4\text{Ni}_3\text{O}_{10\pm\delta}$ is a dominant nickel-containing product at 800–900 °C,^{75,224–226} while PrNiO_3 forms preferentially at lower temperatures ≤ 700 °C.^{228,229} Although the decomposition kinetics is very slow at 580–600 °C (lowest temperature at which the oxidative decomposition was

observed),^{75,228,229} it accelerates with temperature, particularly above 700 °C.⁹⁶

The stability field boundary of the $\text{Pr}_2\text{NiO}_{4+\delta}$ lattice is inter-related with the overstoichiometric oxygen content. Partial substitution of nickel by copper was found to decrease δ and expand the stability field in air to lower temperatures, while doping by iron in the Ni sublattice led to the opposite effect.⁵² However, B-site substitutions have a rather negligible effect on the stability from a practical point of view.^{52,111,118,199,230} A more effective approach, involving the suppression of excess oxygen and stabilisation of the $\text{Pr}_2\text{NiO}_{4+\delta}$ phase under oxidising conditions, is the substitution of praseodymium by alkaline-earth cations. In particular, $\text{Pr}_{2-x}\text{Ca}_x\text{NiO}_{4+\delta}$ solid solutions are reported to be stable in air when $x \geq 0.3$ for at least 250 h at 850 °C.¹⁰¹ Moreover, no evidence of phase separation under oxidizing conditions was observed for $\text{Pr}_{1.35}\text{Sr}_{0.65}\text{Ni}_{0.75}\text{Co}_{0.25}\text{O}_{4+\delta}$ (ref. 177) and heavily Sr-doped $\text{Pr}_{2-x}\text{Sr}_x\text{NiO}_{4+\delta}$ ($x = 1.0-1.6$).^{106,107} The incorporation of cation vacancies into the praseodymium sublattice was suggested as a possible alternative to decrease the oxygen excess and expand the stability field.²³⁰ Yet another strategy involves the substitution of praseodymium by lanthanum or neodymium with the formation of $(\text{Pr}_{1-x}\text{Ln}_x)_2\text{NiO}_{4+\delta}$ solid solutions.^{94–96,228,229} However, it was found that full stabilisation requires the substitution of up to 75% of praseodymium cations.^{96,228,229} Although the intermediate compositions with $x \sim 0.5$ were reported to be stable in the short term (≤ 100 h scale),^{94,95} they decomposed in the course of long-term thermal treatments (a month scale).^{96,228,229}

$\text{Ln}_2\text{NiO}_{4+\delta}$ -derived ceramic materials demonstrate good stability in the presence of steam or carbon dioxide in the gas phase at elevated temperatures. In particular, no degradation of the electrical conductivity of $\text{Ln}_2\text{NiO}_{4+\delta}$ ($\text{Ln} = \text{La}$, Pr, and Nd) and LaSrNiO_4 ceramics in moist air, $p\text{H}_2\text{O} = 0.03$ atm, was observed at 25–630 °C.⁸¹ Water partial pressures of up to 0.3 atm were reported to have no detrimental effect on the conductivity of $\text{Pr}_2\text{NiO}_{4+\delta}$ ceramics at temperatures ≤ 700 °C.²³¹ Li *et al.*²³² reported the phase stability of $\text{Pr}_2\text{NiO}_{4+\delta}$ powder in a 40% steam/60% air mixture at 700 °C (24 h) and the absence of degradation of electrical conductivity of $\text{Pr}_2\text{NiO}_{4+\delta}$ ceramics in a 60% steam/40% air atmosphere at 700 °C (> 7 h test). The TGA-MS experiments performed by Egger *et al.*⁸⁶ did not reveal any significant influence of humidity or carbon dioxide on the oxygen exchange properties of $\text{Nd}_2\text{NiO}_{4+\delta}$ in air containing $\sim 1\%$ of H_2O or 5% of CO_2 at 500–900 °C. Upasen *et al.*²³³ exposed $\text{Ln}_2\text{NiO}_{4+\delta}$ ($\text{Ln} = \text{La}$, Pr, and Nd) ceramics to harsher treatment conditions, consisting of high steam pressure of 40 bar, both with and without CO_2 gas dissolved in water, at 550 °C for 5 days. The presence of secondary phases originating from undesirable hydroxylation and carbonation in the course of the treatment was detected only in the near-surface layers, while the $\text{Nd}_2\text{NiO}_{4+\delta}$ ceramics exhibited the highest structural, mechanical and chemical stability under these conditions. When pure CO_2 was used as the sweep gas, the phase stability upon exposure to CO_2 and the absence of oxygen permeation flux degradation through mixed-conducting $\text{Ln}_2\text{NiO}_{4+\delta}$ -based ceramic membranes were demonstrated in numerous studies conducted at 750–950 °C.^{163,234–239} At the same time, excessive doping by

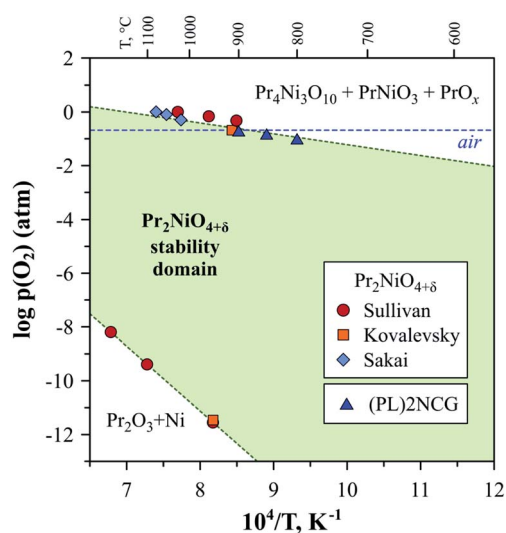


Fig. 6 Approximate stability domain of RP-type $\text{Pr}_2\text{NiO}_{4+\delta}$. The literature data on low- and high- $p\text{O}_2$ stability limits was taken from Sullivan,²²² Kovalevsky⁵² and Sakai.⁹⁵ The data on the high- $p\text{O}_2$ stability boundary of $(\text{Pr}_{0.9}\text{La}_{0.1})_2\text{Ni}_{0.74}\text{Cu}_{0.21}\text{Ga}_{0.05}\text{O}_{4+\delta}$ ((PL)2NCG) was from Xue.²³⁰

alkaline-earth cations into the Ln sublattice may deteriorate the stability of CO₂, as was demonstrated in the case of (La_{1-x}Ca_x)₂(Ni_{0.75}Cu_{0.25})O_{4+δ} for x ≥ 0.2.²³⁷

In addition to chemical stability with respect to the components of the gas phase, electrode materials should preferably exhibit good tolerance towards poisoning by volatile contaminants originating from chromium-based interconnects and silica-based glass-ceramic sealants. The available studies show that Ln₂NiO_{4+δ} electrodes exhibit fairly good tolerance with respect to Cr^{240–244} or Cr + Si^{245,246} poisoning in a dry atmosphere. Lee *et al.*²⁴⁰ reported that despite La₂NiO_{4+δ} and Cr₂O₃ readily reacting at 1000 °C with the formation of LaNiO₃ and LaCrO₃, the polarisation resistance of La₂NiO_{4+δ} electrodes at 520–800 °C is insensitive to chromium introduced by solution infiltration for Cr concentrations of up to 0.6 wt%. The Nd₂NiO_{4+δ} electrodes did not show an appreciable increase in polarisation resistance in the presence of gaseous chromium species at 850 °C and current density of 500 mA cm⁻² during 800 h of testing.²⁴¹ Oxygen surface exchange and electrochemical studies demonstrate the better stability of Ln₂NiO_{4+δ} compared to Sr-containing perovskite-type electrode materials^{242,243,245} due to chromium poisoning being correlated with the formation of strontium chromate at the surface. At the same time, deterioration of the electrode performance was observed due to the acceleration of Cr/Si poisoning as a result of humidity;^{243–246} moreover, the negative effect of humidity becomes stronger when the temperature decreased from 800 °C to 700 °C.^{245,246}

4. Electrical transport properties of Ln₂NiO_{4+δ}-based ceramics

4.1. Electronic conductivity

4.1.1. Undoped Ln₂NiO_{4+δ}. The electrical conductivity of Ln₂NiO_{4+δ} and its derivatives is predominantly p-type electronic. Undoped Ln₂NiO_{4+δ} exhibits thermally activated conductivity in the low-temperature range, but demonstrates a smooth transition from semiconducting to metallic-like behavior above 350–500 °C.^{51,53,57,81,82,86,93,96,97,116,144,156,247–253} The interpretation of the apparent “semiconductor–metal” transition is controversial. Goodenough proposed the coexistence of the localized d_{z²} electron state and itinerant d_{x²-y²} electron states, forming a narrow in-plane σ_{x²-y²} band in La₂NiO₄.^{254,255} The transition to semiconducting behavior in the low-temperature range was interpreted in terms of splitting of the σ_{x²-y²} band due to antiferromagnetic ordering,^{254,255} which was not confirmed, or due to intraatomic exchange interactions with localized d_{z²} electrons,⁴⁵ and also was correlated with an orthorhombic–tetragonal transition.²⁵⁶ These considerations did not account for temperature-dependent oxygen nonstoichiometry. Bassat *et al.*^{51,54} noted that the apparent “semiconductor–metal” transition coincides with the onset of oxygen loss on heating, and argued that the decrease in conductivity on heating in the high-temperature range is caused by a decrease in oxygen content and the hole concentration. Later, attempts to model the temperature dependence of electrical conductivity

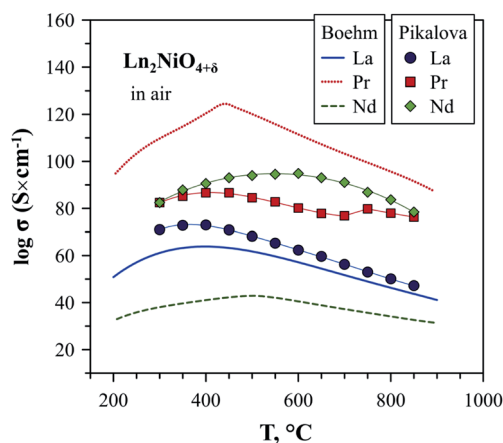


Fig. 7 Electrical conductivity of Ln₂NiO_{4+δ} ceramics in air. The data is from Boehm⁵³ and Pikalova.⁸²

showed that metallic-like behavior cannot be explained only by the decrease in the concentration of charge carriers.^{251,257} In recent works, Ln₂NiO_{4+δ} nickelates are discussed as degenerate p-type semiconductors^{63,64,258} with metal-like band conduction in the high-temperature range^{63,64,142,148,258} and nearly pO₂-independent hole mobility (0.14–0.25 cm² V⁻¹ s⁻¹), which slightly decreases on heating.^{60,63,142,148,258}

As expected for a layered structure, the electrical properties of Ln₂NiO_{4+δ} nickelates are highly anisotropic.^{71,259–261} Bassat *et al.*²⁶⁰ demonstrated that the electrical conductivity of La₂NiO_{4+δ} single crystals along the *a*–*b* plane is more than 3 orders of magnitude higher than that along the *c*-axis at room temperature. Anisotropic electrical properties were obtained for textured Nd₂NiO_{4+δ} ceramics:²⁶² the conductivity along and across the *a*–*b* plane at 500 °C was 270 and 16 S cm⁻¹, respectively, compared to 117 S cm⁻¹ for ceramics with randomly oriented grains.

The electronic conductivity of Ln₂NiO_{4+δ} is p-type and decreases with a reduction in the oxygen partial pressure due to oxygen release from the lattice and corresponding decrease in the concentration of electron holes according to eqn (2).^{52,57,63,139,140,142,148,258,263} Although there is some scattering in the reported conductivity values, which is apparently due to different synthesis techniques and porosity of ceramics, the electrical conductivity of Ln₂NiO_{4+δ} ceramics generally vary in the range of 40–120 S cm⁻¹ in air at 500–900 °C.^{51,53,57,81,82,86,93,96,97,116,140,144,148,247–250,252,253} Considering the relationship between oxygen nonstoichiometry and concentration of electronic charge carriers, eqn (3), the conductivity of Ln₂NiO_{4+δ} can be expected to increase in the sequence La < Pr < Nd. This was confirmed, in particular, by Pikalova *et al.*,⁸² although different relationships were reported in some other works,^{53,81,96} as shown in Fig. 7.

It is necessary to highlight that due to the phase instability in air at 700–900 °C, the reported data on the transport properties of Pr₂NiO_{4+δ} in this temperature range are mostly compromised. In fact, phase decomposition to a mixture of Pr₄Ni₃O_{10±δ} and PrO_x on cooling from higher temperatures was found to

result in a sharp increase in electrical conductivity due to the superior conductivity of RP-type $\text{Pr}_4\text{Ni}_3\text{O}_{10\pm\delta}$ nickelate.⁵² Thus, one may expect that reliable data on the electrical properties of undoped $\text{Pr}_2\text{NiO}_{4+\delta}$ in air include measurements done using fresh samples within the stability domain (≥ 925 °C in air) or quenched samples in a metastable region (up to 600–700 °C in air). The same considerations relate to solid solutions derived from $\text{Pr}_2\text{NiO}_{4+\delta}$ and their respective stability fields.

4.1.2. Effect of A-site deficiency. Bassat *et al.*^{51,264} reported that the electrical conductivity of $\text{La}_{2-x}\text{NiO}_{4+\delta}$ ($x = 0-0.15$) gradually decreases with an increase in the concentration of A-site cation vacancies. In the case of $\text{Nd}_{2-x}\text{NiO}_{4+\delta}$, the conductivity in air was found to increase in the sequence $x = 0 < 0.10 < 0.05$,⁵³ although the conductivity values for the parent material ($x = 0$) were much lower compared to other reports. Therefore, it can be concluded that A-site deficiency is charge-compensated by a decrease in both oxygen content and, to a lesser extent, hole concentration (eqn (5)) and results in a decline in electronic transport.

4.1.3. Mutual solid solutions. In mutual solid solutions, the electrical conductivity generally varies between that of the end members of the series. Increasing praseodymium content in $\text{La}_{2-x}\text{Pr}_x\text{NiO}_{4+\delta}$ was found to enhance the conductivity^{93,265} sharply until $x = 1.0$, and then weakly in the $1.0 \leq x \leq 2.0$ range. Electronic transport in the $(\text{Pr}_{1-x}\text{Nd}_x)_2\text{NiO}_{4+\delta}$ system was reported to decline gradually with an increase in neodymium fraction.⁹⁶ The electrical conductivity of the $\text{La}_{2-x}\text{Sm}_x\text{NiO}_{4+\delta}$ ($x = 0-1.1$) solid solution tended to increase with an increase in samarium content, although the observed variations of σ vs. x were not very systematic, and the highest conductivity was obtained for $x = 0.5$.⁹⁷

4.1.4. A-site doping by alkaline-earth metal cations. As a general trend, an increase in the content of alkaline-earth metal cation in the A sublattice of $\text{Ln}_{2-x}\text{A}_x\text{NiO}_{4+\delta}$ is accompanied by a decrease in the oxygen content, δ , and an increase in the electron-hole concentration according to eqn (6). Consequently, the electronic conductivity in $\text{Ln}_{2-x}\text{A}_x\text{NiO}_{4+\delta}$ ($\text{Ln} = \text{La}, \text{Pr}, \text{Nd}; \text{A} = \text{Ca}, \text{Sr}, \text{Ba}$) increases with x within the solid solution formation range (Fig. 3). This trend was observed in the high-temperature range for $\text{La}_{2-x}\text{Ca}_x\text{NiO}_{4+\delta}$,^{82,99,100,130,131} $\text{La}_{2-x}\text{Sr}_x\text{NiO}_{4+\delta}$,^{81,133,139,141,142,154,266,267} $\text{La}_{2-x}\text{Ba}_x\text{NiO}_{4+\delta}$,²⁶⁶ $\text{Pr}_{2-x}\text{Ca}_x\text{NiO}_{4+\delta}$,^{82,102,267} $\text{Pr}_{2-x}\text{Sr}_x\text{NiO}_{4+\delta}$,^{57,144,268} $\text{Nd}_{2-x}\text{Sr}_x\text{NiO}_{4+\delta}$,^{79,148} $\text{Nd}_{2-x}\text{Ca}_x\text{NiO}_{4+\delta}$,^{53,78,79,82,132} and $\text{Nd}_{2-x}\text{Ba}_x\text{NiO}_{4+\delta}$ (ref. 79) systems. Similar to the parent compounds, substituted $\text{Ln}_{2-x}\text{A}_x\text{NiO}_{4+\delta}$ exhibit a transition from low-temperature semiconducting to high temperature metallic-like behavior on heating.^{53,57,78,79,82,98-100,102,105,131-133,136,144,253,266-268} For Sr-doped (including Sm-based)¹⁴³ systems, this “semiconductor-metal transition” was observed to shift to lower temperatures with an increase in the strontium content, and the compositions with $x \geq 0.8-1.0$ show metallic-like behavior above room temperature.^{79,81,98,105,133,136,137,143,146,147,152,268}

In the case of Sr-rich compositions ($x \geq 1.0$), the electron-hole concentration and electronic conductivity in the high-temperature range reaches the maximum for $x = 1.2$ (Fig. 3), with conductivity values in the range of 340–470 S cm^{-1} at 700 °C, and then declines due to an increase in oxygen vacancy concentration.^{106-108,145} However, the strong anisotropic

expansion of the $\text{Ln}_{2-x}\text{Sr}_x\text{NiO}_{4+\delta}$ ($x > 1.0$) crystal lattice results in microcracking effects in ceramics and, consequently, in an apparent hysteresis in dilatometric and conductivity curves on temperature cycling.^{106,108,138,145}

Similar to undoped nickelates, $\text{Ln}_{2-x}\text{A}_x\text{NiO}_{4+\delta}$ are p-type electronic conductors. Variations in the electrical conductivity as a function of the oxygen partial pressure is directly correlated with the changes in oxygen nonstoichiometry. A decrease in oxygen content with a reduction in $p\text{O}_2$ is accompanied by a decrease in electrical conductivity for compositions with a moderate ($x \leq 0.3$) and large ($x \geq 1.0$) substitutional level, while solid solutions with intermediate dopant contents demonstrate nearly $p\text{O}_2$ -independent oxygen nonstoichiometry ($\delta \sim 0$) and electronic conductivity at 600–900 °C and $p\text{O}_2$ in the range of 10^{-5} to 1.0 atm.^{57,106,108,139,142,145,148,154,269} A reduction of Sr-rich $\text{La}_{2-x}\text{Sr}_x\text{NiO}_{4+\delta}$ ($x \geq 1.0$) at $p\text{O}_2 \sim 10^{-5}$ atm and associated structural changes were observed to result in a localization of electronic charge carriers and a transition to semi-conducting behavior at $T \leq 1000$ °C under mildly reducing conditions.^{152,155}

Shen *et al.*²⁶⁶ reported that the electrical conductivity of $\text{La}_{2-x}\text{A}_x\text{NiO}_{4+\delta}$ ($x = 0.1, 0.3$) is higher for $\text{A} = \text{Sr}$ compared to $\text{A} = \text{Ba}$, while the electronic transport in $\text{La}_{1.7}\text{A}_{0.3}\text{NiO}_{4+\delta}$ was found to increase in the sequence $\text{A} = \text{Sr} \sim \text{Ba} < \text{Ca}$.^{253,267} It should also

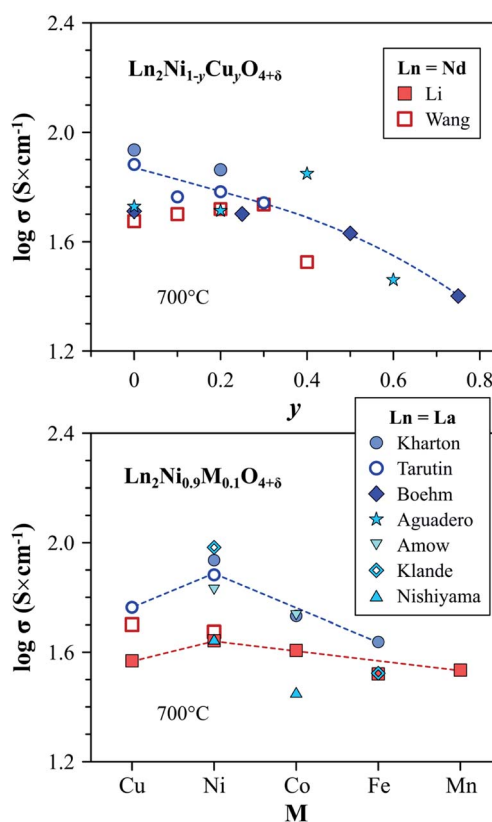


Fig. 8 Trends in the variation of electronic conductivity in the $\text{Ln}_2\text{Ni}_{1-y}\text{Cu}_y\text{O}_{4+\delta}$ and $\text{Ln}_2\text{Ni}_{0.9}\text{M}_{0.1}\text{O}_{4+\delta}$ series at 700 °C in air. Literature sources: Kharton,^{60,214} Tarutin,¹⁵⁷ Boehm,¹¹³ Aguadero,¹¹⁴ Amow,⁹⁷ Klандe,²⁷⁰ Nishiyama,²⁵⁰ Wang,¹¹⁶ and Li.¹¹⁹

be noted that the conductivity of $\text{Sm}_{1.4}\text{Sr}_{0.6}\text{NiO}_{4+\delta}$ ceramics was reported to be only slightly lower compared to their Pr-based analog,⁷³ which seems to imply that the trends in the $\text{Sm}_{2-x}\text{Sr}_x\text{NiO}_{4+\delta}$ system should be similar to other A-site-doped series.

4.1.5. B-site doping by transition metal cations. Substitution of nickel by copper generally results in a gradual moderate decrease in electrical conductivity in $\text{La}_2\text{Ni}_{1-y}\text{Cu}_y\text{O}_{4+\delta}$ (ref. 112–114 and 157) and $\text{Pr}_2\text{Ni}_{1-y}\text{Cu}_y\text{O}_{4+\delta}$ (ref. 45 and 52) systems within the solid solution formation range (Fig. 8), while a minor increase in the conductivity with an increase in copper content was reported for the $\text{Nd}_2\text{Ni}_{1-y}\text{Cu}_y\text{O}_{4+\delta}$ series.¹¹⁶ All the $\text{Ln}_2\text{Ni}_{1-y}\text{Cu}_y\text{O}_{4+\delta}$ exhibit a “metal–insulator” transition on heating in air, with metallic-like behavior in the high-temperature range. Analysis of the $p\text{O}_2$ – T – δ diagram of $\text{La}_2\text{Ni}_{0.8}\text{Cu}_{0.2}\text{O}_{4+\delta}$ employing a statistical thermodynamic approach showed that the lattice sites occupied by nickel and copper cations are essentially equivalent from an energetic point of view.^{61,62,65} Therefore, the decline in electronic transport with copper doping should be attributed to a decrease in oxygen nonstoichiometry and hole concentration.

Although substitution by cobalt or iron has a contrary effect on the δ and concentration of electron holes, as shown in eqn

(7), electronic conductivity of $\text{Ln}_2\text{Ni}_{1-y}\text{Co}_y\text{O}_{4+\delta}$ (ref. 60, 97, 118, 119 and 250) and $\text{Ln}_2\text{Ni}_{1-y}\text{Fe}_y\text{O}_{4+\delta}$ (ref. 52, 60, 119 and 270) decreases on doping. This is attributed to the hole localization and trapping of p-type charge carriers by the dopant cations, forming stable Co^{3+} and Fe^{3+} states.^{60–62,121,271}

Upon comparing the effect of different transition metal dopants, the electrical conductivity at 700 °C in air was reported to decrease from 44 to 33 S cm^{-1} in the sequence $\text{M} = \text{Ni} > \text{Co} > \text{Cu} > \text{Fe} \sim \text{Mn}$ for the $\text{Nd}_2\text{Ni}_{0.9}\text{M}_{0.1}\text{O}_{4+\delta}$ series¹¹⁹ and from 87 to 44 S cm^{-1} in the sequence $\text{M} = \text{Ni} > \text{Co} > \text{Fe}$ for $\text{La}_2\text{Ni}_{0.9}\text{M}_{0.1}\text{O}_{4+\delta}$ solid solutions⁶⁰ (Fig. 8). As in the case of the parent praseodymium nickelate, the data on the electrical conductivity of the doped $\text{Pr}_2\text{NiO}_{4+\delta}$ can be strongly affected by the instability of the lattice under oxidizing condition: the decomposition into $\text{Pr}_4\text{Ni}_3\text{O}_{10\pm\delta}$ and PrO_x phases was observed to result in a sharp increase in the conductivity of $\text{Pr}_2\text{Ni}_{0.9}\text{Fe}_{0.1}\text{O}_{4+\delta}$ and $\text{Pr}_2\text{Ni}_{0.9}\text{Cu}_{0.1}\text{O}_{4+\delta}$ on cooling in air.⁵²

B-site doping by transition metal cations is also known to suppress electronic transport in A-site co-doped compositions. The corresponding high-temperature conductivity data is available for $\text{La}_{1.9}\text{Sr}_{0.1}\text{Ni}_{1-y}\text{Fe}_y\text{O}_{4+\delta}$ ($y = 0.02$ – 0.10),^{272,273} $\text{La}_{2-x}\text{Sr}_x\text{Ni}_{1-y}\text{Fe}_y\text{O}_{4+\delta}$ ($x = 0.5$ – 0.8 , $y = 0$ – 0.5),^{168,172}

Table 2 Ionic conductivity of $\text{Ln}_2\text{NiO}_{4+\delta}$ -based ceramics in air. Visualisation of these data is presented in Fig. S1, ESI

Composition	σ_{O} , S cm^{-1}			t_{O} (800 °C)	E_{a}^b , eV	Ref.
	900 °C	800 °C	700 °C			
$\text{La}_2\text{NiO}_{4+\delta}$	—	0.037	0.015	8.0×10^{-4}	0.87	53, 85 and 277
$\text{La}_2\text{NiO}_{4+\delta}$	0.130	0.053	0.013	7.0×10^{-4}	1.15	263
$\text{La}_2\text{NiO}_{4+\delta}^a$	0.062	0.046	—	8.4×10^{-4}	—	278
$\text{La}_2\text{NiO}_{4+\delta}$	—	0.010	3.7×10^{-3}	1.6×10^{-4}	1.07	100
$\text{La}_{1.95}\text{NiO}_{4+\delta}$	—	0.019	8.7×10^{-3}	—	0.77	85
$\text{La}_{1.9}\text{Sr}_{0.1}\text{NiO}_{4+\delta}$	—	0.012	—	1.3×10^{-4}	—	154
$\text{La}_{1.9}\text{Sr}_{0.1}\text{NiO}_{4+\delta}^a$	0.017	0.010	—	7.8×10^{-5}	0.63	279
$\text{La}_{1.5}\text{Sr}_{0.5}\text{NiO}_{4+\delta}$	3.2×10^{-4}	5.8×10^{-5}	—	—	1.90	280
$\text{La}_{1.5}\text{Sr}_{0.5}\text{Ni}_{0.8}\text{Co}_{0.2}\text{O}_{4+\delta}$	1.9×10^{-4}	3.6×10^{-5}	6.0×10^{-6}	—	1.69	280
$\text{La}_{1.5}\text{Sr}_{0.5}\text{Ni}_{0.6}\text{Co}_{0.4}\text{O}_{4+\delta}$	1.3×10^{-4}	3.4×10^{-5}	4.8×10^{-6}	—	1.86	280
$\text{La}_{1.5}\text{Sr}_{0.5}\text{Ni}_{0.9}\text{Fe}_{0.1}\text{O}_{4+\delta}$	3.6×10^{-4}	1.5×10^{-4}	—	1.2×10^{-6}	1.21	172 and 281
$\text{La}_{1.5}\text{Sr}_{0.5}\text{Ni}_{0.6}\text{Fe}_{0.4}\text{O}_{4+\delta}$	9.7×10^{-4}	2.1×10^{-4}	3.7×10^{-5}	1.3×10^{-5}	1.58	172 and 281
$\text{La}_{1.9}\text{Ca}_{0.1}\text{NiO}_{4+\delta}^a$	0.038	0.022	—	1.7×10^{-4}	0.74	279
$\text{La}_{1.9}\text{Ca}_{0.1}\text{NiO}_{4+\delta}$	—	0.022	9.5×10^{-3}	2.8×10^{-4}	0.86	100
$\text{La}_{1.7}\text{Ca}_{0.3}\text{NiO}_{4+\delta}$	—	4.9×10^{-3}	2.7×10^{-3}	4.2×10^{-5}	0.62	100
$\text{La}_{1.7}\text{Ca}_{0.3}\text{NiO}_{4+\delta}$	—	8.4×10^{-4}	3.0×10^{-4}	1.0×10^{-4}	1.04	282
$\text{La}_2\text{Ni}_{0.5}\text{Cu}_{0.5}\text{O}_{4+\delta}$	—	—	7×10^{-3}	—	—	283
$\text{La}_2\text{Ni}_{0.9}\text{Fe}_{0.1}\text{O}_{4+\delta}$	0.258	—	—	—	—	60
$\text{La}_2\text{Ni}_{0.95}\text{Al}_{0.05}\text{O}_{4+\delta}^a$	0.109	0.085	—	2.5×10^{-3}	—	190
$\text{La}_2\text{Ni}_{0.95}\text{Al}_{0.05}\text{O}_{4+\delta}^a$	2.7×10^{-3}	—	—	—	—	284
$\text{Pr}_2\text{NiO}_{4+\delta}$	—	0.047	0.024	5.0×10^{-4}	0.70	53 and 277
$\text{Pr}_2\text{NiO}_{4+\delta}$	—	0.057	0.026	7.3×10^{-4}	0.84	282
$\text{Pr}_{1.7}\text{Ca}_{0.3}\text{NiO}_{4+\delta}$	—	7.9×10^{-4}	3.0×10^{-4}	9.4×10^{-6}	0.96	282
$\text{Pr}_{1.9}\text{Ni}_{0.75}\text{Cu}_{0.25}\text{O}_{4+\delta}$	—	0.075	0.040	—	0.65	276
$\text{Pr}_{1.9}(\text{Ni}_{0.75}\text{Cu}_{0.25})_{0.95}\text{Ga}_{0.05}\text{O}_{4+\delta}$	—	0.099	0.061	—	0.59	276
$\text{Nd}_2\text{NiO}_{4+\delta}$	—	0.045	0.015	1.3×10^{-3}	1.06	53 and 277
$\text{Nd}_2\text{NiO}_{4+\delta}^a$	2.0×10^{-3}	1.1×10^{-3}	4.4×10^{-4}	—	0.76	286
$\text{Nd}_2\text{NiO}_{4+\delta}$	—	0.076	0.017	9.1×10^{-4}	1.46	282
$\text{Nd}_{1.7}\text{Ca}_{0.3}\text{NiO}_{4+\delta}$	—	6.8×10^{-4}	2.2×10^{-4}	6.0×10^{-6}	1.08	282
$\text{Nd}_{1.9}\text{Ba}_{0.1}\text{NiO}_{4+\delta}$	—	0.040	9.4×10^{-3}	4.1×10^{-4}	1.28	207
$\text{Nd}_{1.9}\text{Ba}_{0.1}\text{NiO}_{4+\delta}\text{F}_{0.05}$	—	0.081	0.023	9.7×10^{-4}	1.17	207

^a $p\text{O}_2 = 0.1$ atm. ^b Calculated using Arrhenius model, $\sigma = (A_0/T)\exp(-E_{\text{a}}/(kT))$.

LaSrNi_{1-y}Mn_yO_{4-δ} (y = 0–0.3),¹⁷¹ La_{1.8}Sr_{0.2}Ni_{1-y}Mo_yO_{4+δ} (y = 0–0.05),¹⁶⁵ La_{1.6}Ca_{0.4}Ni_{1-y}Cu_yO_{4+δ} (y = 0–0.3),¹³¹ La_{1.6}Ca_{0.4}Ni_{1-y}Fe_yO_{4+δ} (y = 0–0.2),¹³¹ Nd_{0.8}Sr_{1.2}Ni_{1-y}M_yO_{4-δ} (M = Co, Fe, y = 0–0.2),²⁷⁴ La_{2-2x}Sr_{2x}Ni_{1-x}Ti_xO_{4+δ},⁴⁵ and La_{2-2x}Sr_{2x}Ni_{1-x}Mn_xO_{4+δ} (x = 0–0.3)¹⁶⁹ systems. On the contrary, Shen *et al.*²⁷⁵ reported an increase in electrical conductivity with an increase in copper content in La_{1.7}Ca_{0.3}Ni_{1-y}Cu_yO_{4+δ} (y = 0.1–0.3) series.

4.1.6. B-site doping by other metal cations. The incorporation of metal cations with a stable oxidation state, such as Mg²⁺ and Al³⁺, into the nickel sublattice of Ln₂NiO_{4+δ} reduces the hole concentration, breaks the Niⁿ⁺–O²⁻–Niⁿ⁺ chains, and therefore decreases the electronic conductivity,^{38,190} although the hole mobility in La₂Ni_{0.95}Al_{0.05}O_{4+δ} was reported to be slightly higher compared to undoped La₂NiO_{4+δ}.¹⁹⁰ The same trends in the variation of electrical conductivity were observed for co-doped compositions including LaSrNi_{1-y}Sc_yO_{4+δ} (y = 0–0.2)¹⁹² and Pr_{2-x}(Ni,Cu)_{1-y}Ga_yO_{4+δ} (y = 0–0.10).^{198,276}

4.2. Oxygen-ionic transport

Ln₂NiO_{4+δ}-based oxide materials are considered mixed ionic-electronic conductors. However, the oxygen-ionic conductivity (σ_O) in these phases is 3 or more orders of magnitude lower compared to electronic conductivity at 500–1000 °C (Table 2). In addition to σ_O, the important parameters used to describe oxygen transport processes include the oxygen diffusion coefficient, *D*, and oxygen surface exchange coefficient, *k* (Table 3). The diffusion coefficient is the measure of the oxygen diffusion rate in the oxide bulk and is interrelated with the oxygen-ionic conductivity *via* the Nernst–Einstein equation (for predominantly electronic conductors) as follows:^{190,286,299,307}

$$\sigma_{\text{O}} = \frac{4F^2 c_{\text{O}} D_{\text{O}}}{RT} \quad (8)$$

where *c*_O is the concentration of oxygen ions and *D*_O is the oxygen self-diffusion coefficient, while the surface exchange coefficient describes the kinetics of oxygen exchange at the oxide/gas interface.

Three main experimental techniques are employed to study oxygen transport in RP-type nickelates:

(i) Isotope exchange depth-profiling with secondary ion mass-spectrometry (IEDP/SIMS) is based on analysis of the concentration profile of traced ¹⁸O ionic species in an oxide sample (polycrystalline ceramics,^{160,276,290,292,294,298–301} single crystals^{277,302,303} or thin films)³⁰⁴ after exposure to an environment enriched with an ¹⁸O isotopic tracer (¹⁸O₂/¹⁶O₂ gas mixtures) at different temperatures. This method yields the oxygen tracer diffusion (*D*^{*}) and surface exchange (*k*^{*}) coefficients. The oxygen tracer and self-diffusion coefficients are related as follows:^{85,282,283,289,299}

$$D^* = f \times D_{\text{O}} \quad (9)$$

where *f* is the tracer correlation factor (or, more generally, the Haven ratio). The values of *f* are ≤1 and depend on the mechanism of diffusion. In the case of RP-type Ln₂NiO_{4+δ} nickelates, it is typically assumed that *f* ~ 1.^{85,282,283,289,299}

(ii) The electrical conductivity relaxation (ECR) method involves the analysis of the transient change in the conductivity of the sample (ceramics^{86,87,92,118,227,286,289,299,305–307} or thin films^{308,309}) induced by an instant change in *p*O₂ at a constant temperature. The oxygen chemical diffusion (*D*_O or *D*_{chem}) and surface exchange (*k*_{chem}) coefficients are obtained by fitting the relaxation data. The chemical diffusion coefficient, *D*_{chem}, is interrelated with the self-diffusion coefficient, *D*_O, *via* the thermodynamic enhancement factor, γ_O.^{190,286,289,299,306,307}

$$\gamma_{\text{O}} = \frac{1}{2} \frac{\partial \ln p\text{O}_2}{\partial \ln c_{\text{O}}} = \frac{D_{\text{chem}}}{D_{\text{O}}} \quad (10)$$

which can be obtained from the analysis of the δ-*p*O₂ dependence.

(iii) Oxygen permeability (OP) studies represent the measurements of oxygen permeation flux, *j*_{O₂}, through a dense ceramic membrane under an applied gradient of oxygen chemical potential. The *j*_{O₂} values obtained under similar conditions can be used as a measure for the rough comparative analysis of the oxygen transport in mixed-conducting ceramics.^{162,163,185,194,195} The oxygen-ionic conductivity, σ_O, oxygen self-diffusion coefficient, *D*_O, and surface exchange coefficient, *k*_O, can be extracted from the oxygen permeation data employing the Wagner equation for bulk diffusion and considering the surface exchange kinetics.^{65,154,263,280,281,283,297,301,310,311} For a mixed conductor with predominately p-type electronic conductivity, the exchange coefficients obtained by different methods are related by:^{286,306,307}

$$k_{\text{O}} \approx k^* \approx \frac{k_{\text{chem}}}{\gamma_{\text{O}}} \quad (11)$$

The other less commonly used experimental techniques are the electrochemical ion/electron blocking cell methods,^{100,207,279–281,284,312} mass⁹² or lattice parameter^{92,305,313,314} relaxation after instant *p*(O₂) change, analysis of electrochemical impedance spectroscopy (EIS) and distribution of relaxation times (DRT) data,^{169,296,315,316} and different methods based on the oxygen isotope exchange with the gas phase, including isotope exchange with the gas phase equilibration (IE-GPE),^{130,291,317,318} pulse isotopic exchange (PIE),^{227,319} and temperature-programmed isotope exchange (TPIE) with ¹⁸O₂ or C¹⁸O₂.^{82,102,276,282,317}

4.2.1. Mechanisms of oxygen-ion transport in RP-type Ln₂NiO_{4+δ}. Similar to the case of electronic conduction, the layered structure of Ln₂NiO_{4+δ} oxides determines the strong anisotropy of oxygen-ionic transport in these phases. Studies on Ln₂NiO_{4+δ} single crystals and oriented thin films by IEDP/SIMS at 340–900 °C demonstrated that the oxygen diffusivity along the *a*–*b* plane is ~3 orders of magnitude faster than along *c* axis.^{277,302–304} The *D*_{*a*–*b*}^{*} values were found to be comparable (slightly higher) to that of the bulk polycrystalline samples, implying that oxygen transport in Ln₂NiO_{4+δ} ceramics is governed by the oxygen diffusion along the basal plane. A large anisotropy was also observed for the surface exchange coefficient with higher *k* values for the *a*–*b* plane.^{277,302–304}

Table 3 Oxygen surface exchange and diffusion processes and the corresponding apparent activation energy values for Ln₂NiO_{4+δ}-based compounds. Visualisation of these data is presented in Fig. S2, ESI

Composition	Method ^a	$D_{\text{chem}}, \text{cm}^2 \text{s}^{-1}$		$k_{\text{chem}}, \text{cm s}^{-1}$		E_{a}, eV		Ref.
		600 °C	700 °C	600 °C	700 °C	D_{chem}	k_{chem}	
La ₂ NiO _{4+δ}	ECR	3.9×10^{-5}	8.3×10^{-5}	2.8×10^{-5}	2.6×10^{-5}	0.53	1.36	287
La ₂ NiO _{4+δ}	EIS	—	—	—	8.6×10^{-7}	—	1.21	169
La ₂ NiO _{4+δ}	ECR	—	2.1×10^{-6}	—	1.2×10^{-6}	2.82	1.99	258
La ₂ NiO _{4+δ}	EIS	—	—	1.6×10^{-7}	8.6×10^{-7}	—	1.21	288
La ₂ NiO _{4+δ}	ECR	4.4×10^{-6}	2.1×10^{-5}	1.2×10^{-4}	8.2×10^{-4}	1.06	1.68	289
La ₂ Ni _{0.95} Al _{0.05} O _{4.025+δ}	ECR	7.9×10^{-6}	2.1×10^{-5}	1.7×10^{-5}	4.4×10^{-5}	0.92	0.84	190
La _{1.8} Sr _{0.2} NiO _{4+δ}	EIS	—	—	4.0×10^{-8}	2.7×10^{-7}	—	1.31	288
La _{1.6} Sr _{0.4} NiO _{4+δ}	EIS	—	—	—	1.7×10^{-7}	—	1.40	288
La _{1.8} Sr _{0.2} Ni _{0.95} Mo _{0.05} O _{4+δ}	ECR	8.0×10^{-6}	12.6×10^{-6}	—	2.0×10^{-4}	0.51	1.31	165
Nd ₂ NiO _{4+δ}	ECR	—	—	3.2×10^{-8}	1.3×10^{-7}	—	1.10	286
Nd ₂ NiO _{4+δ}	ECR	—	—	—	1.2×10^{-4}	—	—	295
Nd ₂ NiO _{4+δ}	EIS	1.8×10^{-8}	5.6×10^{-8}	3.0×10^{-6}	1.8×10^{-7}	0.90	1.43	296
Pr ₂ NiO _{4+δ}	ECR	—	—	2.9×10^{-6}	4.7×10^{-5}	—	1.84	118
Pr ₂ Ni _{0.9} Co _{0.1} O _{4+δ}	ECR	—	—	3.1×10^{-5}	9.9×10^{-5}	—	0.83	118

Composition	Method ^a	$D^*, \text{cm}^2 \text{s}^{-1}$		$k^*, \text{cm s}^{-1}$		E_{a}, eV		Ref.
		600 °C	700 °C	600 °C	700 °C	D^*	k^*	
La ₂ NiO _{4+δ}	IEDP/SIMS	1.3×10^{-8}	3.0×10^{-8}	2.8×10^{-8}	1.9×10^{-7}	0.59	1.24	160
La ₂ NiO _{4+δ}	IE-GPE	—	5.5×10^{-10}	—	7.7×10^{-5}	1.04	1.04	82
La ₂ NiO _{4+δ}	IE-GPE	1.2×10^{-9}	1.1×10^{-8}	1.5×10^{-8}	1.4×10^{-7}	1.34	1.39	130
La ₂ NiO _{4+δ}	IEDP/SIMS	—	3.4×10^{-8}	—	1.8×10^{-7}	0.85	1.61	290
La ₂ NiO _{4+δ}	IE-GPE	1.1×10^{-9}	9.6×10^{-9}	—	1.4×10^{-8}	1.41	1.43	291
La ₂ NiO _{4+δ}	IEDP/SIMS	—	4.8×10^{-8}	—	2.1×10^{-7}	0.88	0.42	53
La ₂ Ni _{0.9} Fe _{0.1} O _{4+δ}	IEDP/SIMS	—	3.5×10^{-8}	—	4.5×10^{-7}	0.99	1.17	53
La ₂ Ni _{0.9} Co _{0.1} O _{4+δ}	IEDP/SIMS	1.0×10^{-8}	2.6×10^{-8}	5.9×10^{-7}	6.4×10^{-7}	0.69	0.57	160
La ₂ Ni _{0.8} Co _{0.2} O _{4+δ}	IEDP/SIMS	1.3×10^{-8}	4.0×10^{-8}	7.3×10^{-7}	1.4×10^{-6}	0.62	0.50	160
La ₂ Ni _{0.5} Co _{0.5} O _{4+δ}	IEDP/SIMS	2.6×10^{-8}	4.7×10^{-8}	7.1×10^{-7}	1.4×10^{-6}	0.62	0.26	160
La ₂ Ni _{0.75} Cu _{0.25} O _{4+δ}	IEDP/SIMS	—	3.5×10^{-8}	—	1.3×10^{-6}	0.62	1.24	113
La ₂ Ni _{0.5} Cu _{0.5} O _{4+δ}	IEDP/SIMS	—	3.0×10^{-8}	—	6.0×10^{-7}	0.51	1.24	113
La _{1.9} Sr _{0.1} NiO _{4+δ}	IEDP/SIMS	—	1.0×10^{-8}	—	1.7×10^{-7}	0.57	1.29	290
La _{1.8} Sr _{0.2} NiO _{4+δ}	IEDP/SIMS	—	6.1×10^{-10}	—	1.2×10^{-7}	0.60	1.06	293
La _{1.8} Sr _{0.3} NiO _{4+δ}	IE-GPE	—	1.4×10^{-9}	—	6.1×10^{-6}	1.04	1.24	267
La _{1.9} Ca _{0.1} NiO _{4+δ}	IE-GPE	—	1.6×10^{-10}	—	1.5×10^{-7}	1.75	0.71	291
La _{1.7} Ca _{0.3} NiO _{4+δ}	IE-GPE	—	1.5×10^{-9}	—	6.0×10^{-6}	1.04	1.24	82
La _{1.7} Ba _{0.3} NiO _{4+δ}	IE-GPE	—	3.3×10^{-9}	—	1.5×10^{-5}	1.04	1.24	267
Nd ₂ NiO _{4+δ}	IE-GPE	—	4.5×10^{-8}	—	—	1.45	—	82
Nd ₂ NiO _{4+δ}	IEDP/SIMS	—	4.5×10^{-8}	—	3.4×10^{-7}	1.06	0.77	53
Nd _{1.95} NiO _{4+δ}	IEDP/SIMS	—	3.5×10^{-8}	—	9.0×10^{-7}	0.65	0.94	53
Nd _{1.8} Ca _{0.2} NiO _{4+δ}	IEDP/SIMS	—	1.0×10^{-8}	—	1.9×10^{-7}	0.72	0.74	53
Nd _{1.7} Ca _{0.3} NiO _{4+δ}	IE-GPE	—	6.3×10^{-10}	—	—	1.09	—	82
Pr ₂ NiO _{4+δ}	IE-GPE	—	7.0×10^{-8}	—	9.5×10^{-5}	0.83	1.19	82
Pr ₂ NiO _{4+δ}	IEDP/SIMS	—	7.2×10^{-8}	—	1.4×10^{-6}	0.73	1.34	53
Pr _{1.7} Ca _{0.3} NiO _{4+δ}	IE-GPE	—	7.6×10^{-10}	—	2.4×10^{-4}	0.93	1.35	82
Pr _{1.9} Ni _{0.75} Cu _{0.25} O _{4+δ}	IEDP/SIMS	4.9×10^{-8}	1.1×10^{-7}	1.8×10^{-7}	5.0×10^{-7}	0.64	0.77	276
Pr _{1.9} Ni _{0.71} Cu _{0.24} Ga _{0.05} O _{4+δ}	IEDP/SIMS	4.3×10^{-8}	—	2.2×10^{-7}	—	—	0.72	297
Pr _{1.9} (Ni _{0.75} Cu _{0.25}) _{0.95} Ga _{0.05} O _{4+δ}	IEDP/SIMS	4.2×10^{-8}	1.8×10^{-7}	2.8×10^{-7}	1.9×10^{-6}	0.57	0.62	276
Pr _{0.85} La _{0.85} Ca _{0.3} NiO _{4+δ}	IE-GPE	—	5.1×10^{-10}	—	7.6×10^{-5}	1.04	1.24	267

^a Abbreviations: ECR – electrical conductivity relaxation; EIS – electrochemical impedance spectroscopy analysis; IEDP/SIMS – isotope exchange depth profiling combined with secondary ion mass-spectrometry; and IE-GPE – isotope exchange with gas phase equilibration.

Oxygen hyperstoichiometry of Ln₂NiO_{4+δ} phases under oxidizing conditions implies that oxygen migration in these materials may involve either oxygen interstitials or oxygen vacancies, or both. Furthermore, interstitial oxygen ions are highly mobile. Temperature-programmed oxygen desorption

studies demonstrate that the release of weakly bonded interstitial oxygen on heating in inert gas starts at temperatures as low as ~200 °C, while desorption processes associated with the formation of oxygen vacancies in the perovskite layers occur at ≥700 °C (ref. 129, 140, 317 and 320) (except Sr-rich oxygen-

deficient $\text{Ln}_{2-x}\text{Sr}_x\text{NiO}_{4-\delta}$ with the onset of oxygen loss from the perovskite layers at lower temperatures).^{108,140,155} This agrees with the results of the TPIE investigations, also showing that the exchange of interstitial oxygen initiates at ~ 200 °C.^{82,102,267}

Several mechanisms of oxygen migration in $\text{Ln}_2\text{NiO}_{4+\delta}$ lattice were considered and modeled employing static lattice simulations (SLS),^{321–324} molecular dynamics simulations (MDS),^{324–327} and density functional theory (DFT) calculations.^{47,328–332}

(A) *Direct interstitial diffusion* pathway involving direct jumps of interstitial oxygen ions between vacant adjacent interstitial sites within rock-salt-type LnO layers. SLS and DFT calculations showed that this pathway is characterized by an excessive energy barrier of 1.2–1.4 eV,^{47,324} and therefore, is least probable compared to other mechanisms of diffusion along the a - b plane.

(B) *Interstitialcy mechanism*, also referred to as a *push-pull* or *cooperative* mechanism. In this mechanism, the oxygen interstitial displaces an apical oxygen ion from the NiO_6 octahedron, which in turn move to an adjacent oxygen interstitial site. Oxygen diffusion in the a - b plane by the interstitialcy mechanism is considered as the main pathway of oxygen transport in $\text{Ln}_2\text{NiO}_{4+\delta}$ phases.^{321,324–327} The calculated E_a values for oxygen migration by this mechanism were reported to be in the range of 0.50–0.65 eV for $\text{La}_2\text{NiO}_{4+\delta}$ and $\text{Pr}_2\text{NiO}_{4+\delta}$ in the high-temperature range,^{324,325,327} which is in good agreement with the oxygen diffusion activation energy values obtained experimentally in most works (Table 3). The interstitialcy diffusion pathway in the a - b plane is also supported by the results of high-temperature neutron diffraction experiments combined with the analysis by the maximum-entropy method.^{328,333,334}

(C) *Vacancy diffusion* mechanism involving oxygen vacancies in equatorial and/or apical oxygen positions in the perovskite layers. Anion Frenkel disorder, as shown by eqn (4), was predicted to be a dominant intrinsic defect formation mechanism in La_2NiO_4 , with oxygen vacancies at the equatorial sites of the NiO_6 octahedra energetically more favorable than that at the apical sites.^{321,323,329} Cleave *et al.*³²³ performed static lattice simulations of La_2NiO_4 and reported that all the considered vacancy mechanisms exhibited lower activation energies than the direct interstitial process, and that oxygen anion diffusion between the equatorial positions is energetically most preferable with the calculated $E_a = 0.55$ eV. However, the formation of oxygen vacancies in the perovskite layers of oxygen-hyperstoichiometric $\text{La}_2\text{NiO}_{4+\delta}$ *via* Frenkel disorder is likely to be suppressed due to the saturation of oxygen interstitials. The thermodynamic analysis of the $p\text{O}_2$ - T - δ diagrams of undoped and B-site-substituted $\text{La}_2\text{NiO}_{4+\delta}$ (ref. 61, 62 and 271) showed that the vacancy formation processes under thermodynamic equilibrium conditions are statistically insignificant when $\delta \geq 0$. Furthermore, the MD simulations carried out on stoichiometric La_2NiO_4 and Nd_2NiO_4 demonstrated insignificant oxygen diffusivities in the high-temperature range.^{325,326} Nonetheless, the vacancy mechanism must be involved in oxygen diffusion across the perovskite layers (along the c axis).^{277,303} A limited vacancy transport mechanism was identified along the c axis in the MD simulations of $\text{Pr}_2\text{NiO}_{4+\delta}$.³²⁷ Furthermore, the role of oxygen vacancies is expected to increase as a result of

acceptor-type A-site substitutions in $\text{Ln}_{2-x}\text{A}_x\text{NiO}_{4+\delta}$ (A = alkaline-earth cation) accompanied by a reduction in the overall oxygen content and a gradual transition to oxygen deficiency with an increase in x (ref. 145 and 329) and with a reduction in $p\text{O}_2$.³³⁵ This seems to be supported by the results of TPIE studies, which were interpreted as an indication of two distinguishable oxygen diffusion pathways in some $\text{Ln}_{2-x}\text{A}_x\text{NiO}_{4+\delta}$ nickelates.^{82,102,276,282,330}

In addition to O^{2-} transport, the involvement of interstitial peroxide O_2^- ions in different diffusion mechanisms is considered.^{277,321,329,331} In particular, the DFT calculations predict that O_1^- species may be more stable compared to O_1^{2-} ions and oxygen vacancies at certain strontium contents in $\text{La}_{2-x}\text{Sr}_x\text{NiO}_{4+\delta}$,^{329,331} while the diffusion of O_1^- by the interstitialcy mechanism may be more energetically favorable.^{321,331}

4.2.2. Undoped $\text{Ln}_2\text{NiO}_{4+\delta}$. The IEDP/SIMS studies of single crystals at 450–700 °C demonstrated comparable oxygen diffusivity along the a - b plane for $\text{La}_2\text{NiO}_{4+\delta}$ and $\text{Pr}_2\text{NiO}_{4+\delta}$ with an activation energy of 0.67 eV for Ln = Pr, whereas higher activation energy (1.4 eV) in the case of $\text{Nd}_2\text{NiO}_{4+\delta}$ results in lower D^* values at temperatures ≤ 600 °C,^{302,303} as shown in Fig. 9. All the $\text{Ln}_2\text{NiO}_{4+\delta}$ single crystals also have comparable k_{a-b}^* , which is 0.5–1.0 orders of magnitude higher than D_{a-b}^* .^{302,303} Similar trends are generally observed for undoped polycrystalline $\text{Ln}_2\text{NiO}_{4+\delta}$.⁵³ The ionic conductivity of $\text{Ln}_2\text{NiO}_{4+\delta}$ ceramics is around 0.05 S cm^{-1} at 800 °C in air (Table 2). Furthermore, $\text{La}_2\text{NiO}_{4+\delta}$ and $\text{Pr}_2\text{NiO}_{4+\delta}$ ceramic membranes show similar oxygen permeability at ≥ 900 °C.^{52,225}

Compared to the oxygen diffusion coefficients, there is a substantially larger variation in the reported values of k and corresponding activation energies, as noted in a number of works.^{53,300,302} It was highlighted that the scattering in measured surface exchange coefficients can be caused by the differences in surface chemistry (surface termination, near-surface rearrangement, and presence of extrinsic impurities) as a result of different thermal pre-history.³⁰² Generally, the oxygen diffusion

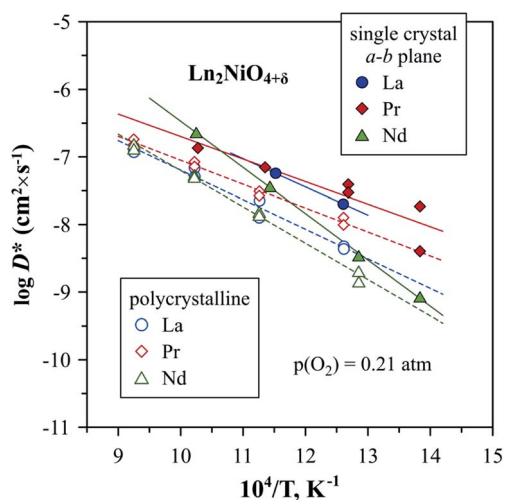


Fig. 9 Temperature dependence of oxygen tracer diffusion coefficient, D^* , reported for $\text{Ln}_2\text{NiO}_{4+\delta}$ single crystals (a - b plane) and polycrystalline samples.^{53,302,303}

and surface exchange coefficients of $\text{Ln}_2\text{NiO}_{4+\delta}$ ceramics are higher compared to many perovskite systems, such as $\text{La}_{0.6}\text{Sr}_{0.4}\text{Fe}_{0.8}\text{Co}_{0.2}\text{O}_{3-\delta}$ and $\text{La}_{0.6}\text{Sr}_{0.4}\text{Fe}_{0.8}\text{Ni}_{0.2}\text{O}_{3-\delta}$, but lower compared to the best $(\text{La,Sr})\text{CoO}_{3-\delta}$ mixed conductors.^{53,113,290,307,317}

Since interstitial oxygen ions are the dominant ionic charge carriers in $\text{Ln}_2\text{NiO}_{4+\delta}$ under oxidizing conditions, the ionic conductivity,^{65,263,278,279,286,307,311} oxygen diffusion coefficient^{278,279,301,307,311,312} and surface exchange coefficient^{286,301,307} decrease with a reduction in $p\text{O}_2$ due to the decrease in the interstitial oxygen concentration, as shown by eqn (2).

The instability of the RP-type $\text{Pr}_2\text{NiO}_{4+\delta}$ lattice under oxidizing conditions has a strong impact on the experimentally measured ionic transport parameters in the temperature range of 700–900 °C. In particular, it has been demonstrated that the decomposition of $\text{Pr}_2\text{NiO}_{4+\delta}$ ceramics into $\text{Pr}_4\text{Ni}_3\text{O}_{10+\delta}$, PrO_x and PrNiO_3 at 750 °C in air results in an increase in the oxygen permeation flux and apparent values of oxygen diffusion and surface exchange coefficients by 1–2 orders of magnitude within 120 h.²²⁷ A similar increase in the oxygen permeability of $\text{Pr}_2\text{NiO}_{4+\delta}$ membranes with time caused by phase decomposition at temperatures below 900 °C was reported in ref. 52 and 225. On the contrary, phase separation resulted in a deterioration of the oxygen permeation flux through $(\text{Pr}_{0.9}\text{La}_{0.1})_{2-x}\text{Ni}_{0.74}\text{Cu}_{0.21}\text{Ga}_{0.05}\text{O}_{4+\delta}$ membranes at 800–900 °C.²³⁰ Berger *et al.*¹¹⁸ observed the exsolution of PrO_x particles on the surface of $\text{Pr}_2\text{NiO}_{4+\delta}$ and $\text{Pr}_2\text{Ni}_{0.9}\text{Co}_{0.1}\text{O}_{4+\delta}$ ceramic samples in the course of ECR at 600–800 °C and $p\text{O}_2 = 10^{-3}$ atm, and correlated this with an increase in the measured oxygen exchange coefficients upon temperature cycling.

4.2.3. A-site cation deficiency. The data on ionic transport in A-site-deficient nickelates is scarce and somewhat contradictory, although one may expect a decline in oxygen diffusivity considering the trends in oxygen nonstoichiometry (see Subsection 2.2.1). Zhao *et al.*⁸⁵ observed that the introduction of A-site cation vacancies in $\text{La}_{2-x}\text{NiO}_{4+\delta}$ ($x = 0.5$) results in a slight decrease in the oxygen diffusion coefficient, D^* , and ionic conductivity, but also increases the activation energy for k^* , thus suppressing oxygen exchange at temperatures below 800 °C compared to $\text{La}_2\text{NiO}_{4+\delta}$. In the $\text{Nd}_{2-x}\text{NiO}_{4+\delta}$ system,⁵³ a minor neodymium deficiency ($x = 0.05$) was found to have a negligible effect on the oxygen diffusivity and slightly improved the oxygen exchange, while a further increase in A-site vacancy concentration up to $x = 0.10$ resulted in a decline in both D^* and k^* compared to the cation-stoichiometric $\text{Nd}_2\text{NiO}_{4+\delta}$. Sadykov *et al.*³¹⁷ found no substantial effect of A-site deficiency on the oxygen self-diffusion coefficients and exchange rates of $\text{Pr}_{1-x}\text{NiO}_{4+\delta}$ at 600–850 °C, but later reported more than an order of magnitude increase in D_{chem} and k_{chem} at 500 °C for $\text{Pr}_{1.9}\text{NiO}_{4+\delta}$ compared to the parent $\text{Pr}_2\text{NiO}_{4+\delta}$.⁹² The introduction of A-site cation vacancies in $\text{Nd}_{2-x}\text{Ni}_{0.75}\text{Cu}_{0.25}\text{O}_{4+\delta}$ ($x = 0-0.10$) was found to improve the oxygen diffusivity and oxygen permeation flux through ceramic membranes at 750–880 °C despite a decrease in oxygen content,⁸⁷ which was accompanied by some decline in surface exchange rates. Similarly, the oxygen permeability of $(\text{Pr}_{0.9}\text{La}_{0.1})_{2-x}\text{Ni}_{0.74}\text{Cu}_{0.21}\text{Ga}_{0.05}\text{O}_{4+\delta}$ ($x = 0-$

0.10) membranes was reported to increase 2 times with the introduction of A-site cation vacancies,^{285,336} while oxygen excess in the lattice was suppressed.²⁸⁵ This effect was attributed to the contribution of highly mobile oxygen vacancies to ionic transport.²⁸⁵

4.2.4. Mutual solid solutions. Vibhu *et al.*⁹³ performed IEDP/SIMS studies of $\text{La}_{2-x}\text{Pr}_x\text{NiO}_{4+\delta}$ ($x = 0.5, 1.0$ and 1.5) ceramics. They found that the oxygen diffusion coefficient, D^* , of solid solutions at 500–700 °C is close to that reported for $\text{La}_2\text{NiO}_{4+\delta}$ and $\text{Pr}_2\text{NiO}_{4+\delta}$ and moderately increases with an increase in praseodymium content. The values of the surface exchange coefficient, k^* , did not show a systematic change with the composition and varied in a narrow range.

4.2.5. A-site substitutions. The studies on the oxygen transport parameters using different techniques revealed that the partial substitution of Ln^{3+} by alkaline-earth cations in $\text{Ln}_{2-x}\text{A}_x\text{NiO}_{4+\delta}$ generally suppresses the oxygen diffusivity, ionic conductivity, surface exchange kinetics, and oxygen permeability (*e.g.* Tables 2 and 3). The corresponding literature data is available for the $\text{La}_{2-x}\text{Sr}_x\text{NiO}_{4+\delta}$,^{140,269,279,290,298,337,338} $\text{La}_{2-x}\text{Ca}_x\text{NiO}_{4+\delta}$,^{82,100,130,279,282,291} $\text{Nd}_{2-x}\text{Ca}_x\text{NiO}_{4+\delta}$,^{53,82,282} and $\text{Pr}_{2-x}\text{Ca}_x\text{NiO}_{4+\delta}$ ^{82,102,276,282,330} systems. In particular, the substitution of 5 and 10 at% of lanthanum by strontium in $\text{La}_{2-x}\text{Sr}_x\text{NiO}_{4+\delta}$ was reported to decrease the oxygen diffusion coefficient at 640–1000 °C by *ca.* 1 and 2 orders of magnitude, respectively.^{279,290,298,337} The negative effect of acceptor-type doping on oxygen ionic transport and exchange is mainly attributed to the decrease in the concentration of ionic charge carriers (interstitial oxygen ions) with an increase in x in $\text{Ln}_{2-x}\text{A}_x\text{NiO}_{4+\delta}$ (see Subsection 2.2.3). Possible steric effects are considered as an additional factor.^{53,82,102,279,282} The interstitialcy mechanism involves the movement of interstitial oxygen ions through Ln_3 triangles in the rock-salt-type layers. The substitution of Ln^{3+} by larger A^{2+} cations (*e.g.* La^{3+} by Sr^{2+}) reduces the free volume available for interstitial migration in the LnO layers²⁷⁹ and the radius of diffusion channels through $(\text{Ln,A})_3$ triangles,^{53,82,102,282} thus contributing to the decline in ionic mobility.

Contrary to other works, Shen *et al.*¹⁰⁰ reported that the ionic conductivity of $\text{La}_{2-x}\text{Ca}_x\text{NiO}_{4+\delta}$ ($x = 0-0.3$) at 600–800 °C increases with moderate Ca doping ($x = 0.1$), despite the decrease in oxygen overstoichiometry, and then declines upon further doping. However, it should be noted that the value of σ_{O} obtained for undoped $\text{La}_2\text{NiO}_{4+\delta}$ in that work is lower compared to other literature data (Table 2). Zhu *et al.*³³⁹ found that substitution of 5 at% of lanthanum by bismuth enhances the oxygen chemical diffusion and surface exchange coefficient of $\text{La}_{1.65}\text{Bi}_{0.1}\text{Sr}_{0.25}\text{NiO}_{4+\delta}$ by a factor of 2–3 compared to $\text{La}_{1.75}\text{Sr}_{0.25}\text{NiO}_{4+\delta}$ at 700–800 °C. This was attributed to the minor increase in oxygen excess with bismuth doping and higher oxygen diffusivity in the doped material associated with the high polarizability of bismuth cations.

4.2.6. B-site doping by transition metal cations. IEDP/SIMS and oxygen permeation studies^{113,283,299,306} demonstrated that the ionic transport parameters in $\text{La}_2\text{Ni}_{1-y}\text{Cu}_y\text{O}_{4+\delta}$ ($y = 0-0.75$) tend to deteriorate with an increase in copper concentration in the nickel sublattice, and consequently, a decrease in oxygen

interstitial concentration (see Subsection 2.2.4). $\text{La}_2\text{Ni}_{0.9}\text{Cu}_{0.1}\text{O}_{4+\delta}$ was reported to exhibit a slightly higher oxygen self-diffusion coefficient, D_{O} , and a similar surface exchange coefficient, k , compared to undoped $\text{La}_2\text{NiO}_{4+\delta}$ at 800–950 °C.³⁰⁶ A further increase in copper content ($y \geq 0.25$) results in a gradual decrease in the oxygen tracer diffusion coefficient, D^* , at 490–810 °C, although the changes in oxygen diffusivity do not exceed one order of magnitude^{113,283} and moderate copper doping may still be favorable at lower temperatures of ~ 500 °C.¹¹³ Simultaneously, the substitution of nickel by copper ($y = 0.25$ – 0.75) was found to increase the activation energy for the exchange coefficient, k^* , thus substantially suppressing the oxygen surface exchange at temperatures below 750 °C compared with that for undoped lanthanum nickelate.¹¹³

Moderate copper doping was found to be favorable for oxygen transport in $\text{Pr}_2\text{NiO}_{4+\delta}$. In particular, Miyoshi *et al.*¹⁶² reported that the oxygen permeability of $\text{Pr}_2\text{Ni}_{1-y}\text{Cu}_y\text{O}_{4+\delta}$ ($y = 0.1$ – 0.5) ceramic membranes at 600–1000 °C reached the maximum at $y = 0.2$ and declines upon further doping. IEDP/SIMS studies revealed that the oxygen tracer diffusion coefficient, D^* , and ionic conductivity, σ_{O} , of copper-doped $\text{Pr}_{1.9}\text{Ni}_{0.75}\text{Cu}_{0.25}\text{O}_{4+\delta}$ at 730–800 °C is ~ 2 times higher compared to undoped praseodymium nickelate.²⁷⁶

Static lattice and molecular dynamics simulations³²⁴ showed that although the incorporation of transition metal cations with the 3+ oxidation state (such as Co^{3+} or Fe^{3+}) into the nickel sublattice increases the concentration of ionic charge carriers, these dopants simultaneously tend to reduce the ionic mobility. This generally agrees with the reported experimental results. Kilner and Shaw¹⁶⁰ performed IEDP/SIMS studies of $\text{La}_2\text{Ni}_{1-y}\text{Co}_y\text{O}_{4+\delta}$ ceramics and found that within the solid solution formation range under oxidizing conditions ($y = 0$ – 0.2), cobalt doping has a rather minor impact on the oxygen diffusivity with similar values of D^* for all compositions (despite the increase in δ with doping). Simultaneously, the substitution of Ni by Co decreases E_{a} for the surface exchange coefficient, k^* , and enhances oxygen exchange, especially at lower temperatures.¹⁶⁰ Similarly, the studies of co-substituted $\text{La}_{1.5}\text{Sr}_{0.5}\text{Ni}_{1-y}\text{Co}_y\text{O}_{4+\delta}$ ($y = 0$ – 0.4) nickelates by oxygen permeation and Hebb–Wagner polarization methods at 800–1000 °C revealed that although doping by cobalt increases the interstitial oxygen content and improves the surface oxygen exchange, it also deteriorates the oxygen diffusivity, and to a lesser extent, the ionic conductivity.²⁸⁰ Berger *et al.*¹¹⁸ reported based on the ECR studies at $p\text{O}_2 = 10^{-3}$ atm at 600–800 °C that doping with cobalt in $\text{Pr}_2\text{Ni}_{0.9}\text{Co}_{0.1}\text{O}_{4+\delta}$ decreases the activation energy for surface oxygen exchange and substantially improves k_{chem} at temperatures below 800 °C, which is *ca.* one order of magnitude at 600 °C. Later, they confirmed³¹⁶ by analysis of the EIS data for $\text{Pr}_2\text{Ni}_{1-y}\text{Co}_y\text{O}_{4+\delta}$ ($y = 0$ and 0.1) microelectrodes at 550–850 °C that the substitution by cobalt improves the oxygen exchange at $T < 800$ °C and $p(\text{O}_2) = 10^{-3}$ – 10^{-2} atm, while the effect was opposite at atmospheric oxygen pressure.

Substitution of 10 at% of nickel by iron has a comparatively minor effect on the oxygen transport, as revealed by IEDP/SIMS studies at 700–840 °C.²⁹⁸ Specifically, D^* and k^* of $\text{La}_2\text{Ni}_{0.9}\text{Fe}_{0.1}\text{O}_{4+\delta}$ are similar to that of undoped lanthanum nickelate at higher temperatures (despite the higher δ), but the

oxygen diffusivity tends to decline to some extent upon cooling with respect to $\text{La}_2\text{NiO}_{4+\delta}$, and the opposite effect was observed for the surface exchange. Analysis of the oxygen permeation data for $\text{La}_2\text{Ni}_{0.9}\text{Fe}_{0.1}\text{O}_{4+\delta}$ ceramic membranes^{60,161} showed that doping by iron results in a slightly higher ionic mobility compared to $\text{La}_2\text{NiO}_{4+\delta}$ at 900–950 °C, but deteriorates the oxygen transport at lower temperatures. Furthermore, Klante *et al.*¹⁶³ reported that the oxygen permeability of $\text{La}_2\text{NiO}_{4+\delta}$ membranes exceeds that of $\text{La}_2\text{Ni}_{0.9}\text{Fe}_{0.1}\text{O}_{4+\delta}$ in the entire studied temperature range (750–950 °C). Gilev *et al.*²⁸¹ studied the oxygen transport in the $\text{La}_{2-x}\text{Sr}_x\text{Ni}_{1-y}\text{Fe}_y\text{O}_{4+\delta}$ ($x = 0.5$ and 0.8 , $y = 0.1$ – 0.4) system employing the oxygen permeation and Hebb–Wagner polarizations techniques and found that co-substitution by iron (up to 40 at% in the nickel sublattice) enhances the oxygen permeability, bulk ionic diffusion and oxygen surface exchange, while the oxygen self-diffusion coefficient D_{O} is lower compared to that of Fe-free $\text{La}_{1.5}\text{Sr}_{0.5}\text{NiO}_{4+\delta}$.²⁸⁰ Miyoshi *et al.*³⁴⁰ reported that co-doping by iron improves the oxygen permeability of $\text{Pr}_2\text{Ni}_{0.8-y}\text{Cu}_{0.2}\text{Fe}_y\text{O}_{4+\delta}$ ($y = 0$ – 0.20) ceramics at 600–1000 °C with the best results obtained for $y = 0.05$.

The positive effects of co-substitutions by transition metal cations on oxygen transport were also reported for other $(\text{La},\text{Sr})_2(\text{Ni},\text{M})\text{O}_{4+\delta}$ systems. Gómez *et al.*¹⁶⁵ performed ECR measurements of $\text{La}_{1.8}\text{Sr}_{0.2}\text{Ni}_{0.95}\text{Mo}_{0.05}\text{O}_{4+\delta}$ at 600–900 °C and found that D_{chem} is almost an order of magnitude higher than that of $\text{La}_{1.8}\text{Sr}_{0.2}\text{NiO}_{4+\delta}$ and comparable to that of undoped $\text{La}_2\text{NiO}_{4+\delta}$ (although with a two times lower activation energy, leading to a higher oxygen diffusivity at $T < 700$ °C), while the surface exchange coefficient, k_{chem} , exceeds that of the undoped nickelate by more than an order of magnitude. Li *et al.*¹⁶⁹ performed an analysis of EIS data obtained for $\text{La}_{2-2x}\text{Sr}_{2x}\text{Ni}_{1-x}\text{Mn}_x\text{O}_{4+\delta}$ electrodes ($x = 0$ – 0.30) at 600–800 °C and demonstrated that co-substitution by manganese promotes the surface exchange kinetics: the surface exchange coefficient, k , reaches the maximum for $x = 0.10$, but declines upon further doping.

Comparing the available oxygen permeation data for RP-type nickelate membranes with different dopants, one may also find the following trends:

- The oxygen transport in $\text{La}_2\text{Ni}_{0.9}\text{M}_{0.1}\text{O}_{4+\delta}$ at temperatures below 850–900 °C decreases in the sequence $\text{M} = \text{Ni} > \text{Co} > \text{Fe}$;^{60,163}
- In the $\text{La}_2\text{Ni}_{0.8}\text{M}_{0.2}\text{O}_{4+\delta}$ series, the oxygen transport at 600–1000 °C was reported to decrease in the sequence $\text{M} = \text{Cu} > \text{Co} > \text{Fe} > \text{Mn}$;¹⁶²
- The oxygen permeability of $\text{La}_2\text{Ni}_{0.8}\text{Cu}_{0.2}\text{O}_{4+\delta}$ is slightly lower compared to that of $\text{La}_2\text{Ni}_{0.9}\text{Co}_{0.1}\text{O}_{4+\delta}$ at 850–950 °C and similar at 700–800 °C;^{214,341}
- Oxygen permeability in the $\text{PrNi}_{0.75}\text{Cu}_{0.20}\text{M}_{0.05}\text{O}_{4+\delta}$ series at 600–1000 °C was found to decline in the sequence $\text{M} = \text{Fe} > \text{Cr} > \text{V}$.¹⁸⁵

4.2.7. B-site doping by other metal cations. Jeon *et al.*¹⁹⁰ studied aluminum-doped $\text{La}_2\text{Ni}_{0.95}\text{Al}_{0.05}\text{O}_{4+\delta}$ by the ECR method at 800–1000 °C and reported a non-negligible improvement in the oxygen self-diffusion coefficient, D_{O} , and ionic conductivity, σ_{O} , compared to the literature data on

undoped $\text{La}_2\text{NiO}_{4+\delta}$ (Table 2). Later they reinvestigated this material employing the electrochemical blocking cell method at 900–1000 °C.²⁸⁴ Although the updated D_{chem} and k_{chem} values were similar to that in the first report and slightly exceeded the corresponding parameters for undoped lanthanum nickelate, doping with aluminum was shown to suppress the self-diffusion coefficient, D_{O} , and oxygen-ionic conductivity by ~ 1.5 orders of magnitude (Tables 2 and 3). This was attributed to the steric effects, namely shrinkage of the lattice and reduction of free volume for oxygen diffusion caused by aluminum doping.²⁸⁴ However, it should be noted that the aluminum doping also was found to decrease the concentration of interstitial oxygen.¹⁸⁹

Klande *et al.*¹⁶³ reported that partial substitution of nickel by aluminum or magnesium resulted in the lower oxygen permeability of $\text{La}_2\text{Ni}_{0.9}\text{M}_{0.1}\text{O}_{4+\delta}$ ($\text{M} = \text{Al}$ or Mg) ceramic membranes compared to the parent $\text{La}_2\text{NiO}_{4+\delta}$, although this may be partly attributed to the presence of phase impurities.

Ishihara *et al.*^{194,195,198} performed extensive oxygen permeability screening tests at 600–1000 °C and found that the introduction of gallium into the nickel sublattice of $\text{Ln}_2\text{Ni}_{0.75}\text{Cu}_{0.25}\text{O}_{4+\delta}$ ($\text{Ln} = \text{Nd}$ or Pr) combined with the introduction of A-site vacancies is a suitable approach to improve the oxygen permeability of nickelate membranes. The optimum composition was claimed to be $\text{Ln}_{2-2x}(\text{Ni}_{0.75}\text{Cu}_{0.25})_{1-x}\text{Ga}_x\text{O}_{4+\delta}$ with $x = 0.05$ and with better transport properties in the case of $\text{Ln} = \text{Pr}$.^{194,195,198} However, it should be noted that it is hard to distinguish between the effects of cation deficiency and gallium doping without detailed studies. As mentioned above, the oxygen permeability of A-site-deficient

$(\text{Pr}_{0.9}\text{La}_{0.1})_{1.90}\text{Ni}_{0.74}\text{Cu}_{0.21}\text{Ga}_{0.05}\text{O}_{4+\delta}$ membranes was found to be more than 2 times that of the cation-stoichiometric analog $(\text{Pr}_{0.9}\text{La}_{0.1})_2\text{Ni}_{0.74}\text{Cu}_{0.21}\text{Ga}_{0.05}\text{O}_{4+\delta}$.²⁸⁵ Hyodo *et al.*²⁷⁶ performed IEDP/SIMS studies of $\text{Pr}_{1.9}(\text{Ni}_{0.75}\text{Cu}_{0.25})_{1-y}\text{Ga}_y\text{O}_{4+\delta}$ ($y = 0$ and 0.05) nickelates and found that gallium doping results in a slight improvement in the oxygen tracer diffusion coefficient, D^* , and ionic conductivity (~ 1.5 times, Table 3), and also results in some enhancement in oxygen exchange. This composition exhibits the highest ionic conductivity among the $\text{Ln}_2\text{NiO}_{4+\delta}$ -based phases reported thus far.

Based on the oxygen permeation screening tests at 600–1000 °C, the following trends should also be mentioned:

- The oxygen transport in $\text{Pr}_2\text{Ni}_{0.9}\text{M}_{0.1}\text{O}_{4+\delta}$ was reported to decrease in the sequence $\text{M} = \text{Mg} > \text{Ga} > \text{Al}$.¹⁶² Besides, the oxygen permeability of $\text{Pr}_2\text{Ni}_{0.9}\text{Mg}_{0.1}\text{O}_{4+\delta}$ membranes was also higher compared to that of $\text{Pr}_2\text{Ni}_{0.8}\text{M}_{0.2}\text{O}_{4+\delta}$ ($\text{M} = \text{Cu}$ or Zn);¹⁶²

- The oxygen permeability of $\text{PrNi}_{0.75}\text{Cu}_{0.20}\text{M}_{0.05}\text{O}_{4+\delta}$ membranes decreases in the sequence $\text{Al} > \text{In} > \text{Zr}$, in all cases being lower compared to $\text{M} = \text{Fe}$.¹⁸⁵

- The oxygen transport in $\text{Pr}_{1.90}(\text{Ni}_{0.75}\text{Cu}_{0.25})_{0.95}\text{M}_{0.05}\text{O}_{4+\delta}$ decreases in the sequence $\text{M} = \text{Ga} > \text{Al} > \text{In}$.¹⁹⁵

4.2.8. Substitutions in the oxygen sublattice. Tarutin *et al.*²⁰⁷ studied $\text{Nd}_{1.9}\text{Ba}_{0.1}\text{NiO}_{4+\delta}\text{F}_\gamma$ ($\gamma = 0$ – 0.10) nickelates employing the Hebb–Wagner electron blocking method and found that the moderate introduction of fluorine into the oxygen sublattice may be favorable for oxygen-ionic transport, leading to an increase in ionic conductivity by a factor of 2 for $\gamma = 0.05$. This was attributed to the mixed anion lattice effect.^{342–348}

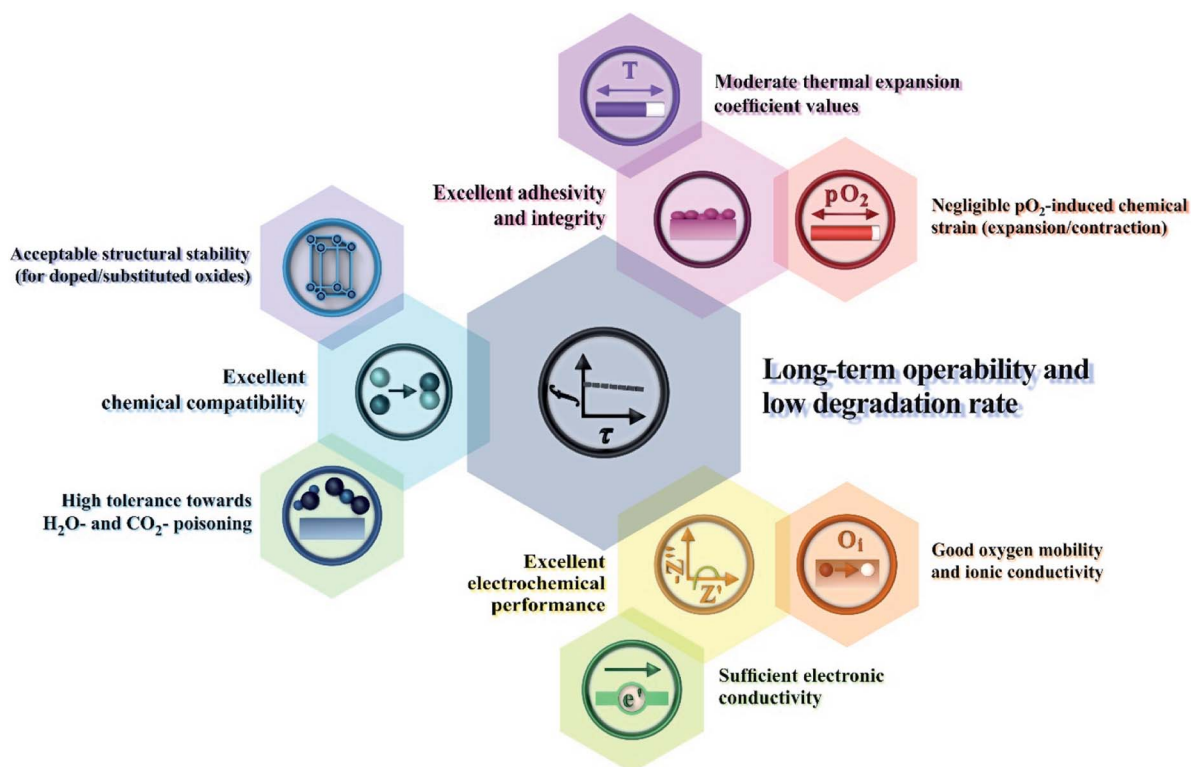


Fig. 10 Main correlations between the performance of $\text{Ln}_2\text{NiO}_{4+\delta}$ electrode materials and their functional properties.

5. Ln₂NiO_{4+δ}-based materials as electrodes for proton-conducting electrochemical cells

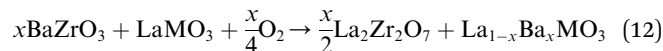
In this section, we discuss the results of research regarding the utilisation of Ln₂NiO_{4+δ}-based materials as electrodes of protonic ceramic electrochemical cells. The success of this application depends on many factors (Fig. 10), where the inherent properties of the RP phases (considered in detail in the previous sections) and their behaviour upon contact with proton-conducting electrolytes, including chemical reactivity, thermal compatibility and electrochemical activity.

5.1. Chemical compatibility with proton-conducting electrolytes

In terms of their thermodynamic stability, Ln₂NiO_{4+δ}-based phases exhibit considerable chemical tolerance towards interaction with state-of-the-art proton-conducting materials. This may be due to two main factors, *i.e.* their wide structural flexibility upon cationic interdiffusion, and the low number of impurity phases capable of being formed at interfaces upon long-term treatment.

Lyagaeva *et al.*³⁴⁹ studied the chemical interaction features of 13 cathode materials with BaCe_{0.9}Y_{0.1}O_{3-δ} (BCY) and BaZr_{0.8}Y_{0.2}O_{3-δ} (BZY) electrolytes using 50 : 50 wt% mixtures calcined at 1100 °C for 10 h. The Co-containing cathodes and manganites, comprising simple cobaltites (Ba_{0.5}Sr_{0.5}CoO_{3-δ}), layered cobaltites (GdBaCo₂O_{5+δ}, NdBaCo₂O_{5+δ}, and Y_{0.8}Ca_{0.2}BaCo₄O_{7+δ}), simple cobaltite-ferrites (Ba_{0.5}Sr_{0.5}Co_{0.2}Fe_{0.8}O_{3-δ}, Ba_{0.5}Sr_{0.5}Co_{0.8}Fe_{0.2}O_{3-δ}, and La_{0.6}Sr_{0.4}Co_{0.2}Fe_{0.8}O_{3-δ}), layered cobaltite-ferrites (GdBaCoFeO_{5+δ} and NdBa_{0.5}Sr_{0.5}Co_{1.5}Fe_{0.5}O_{5+δ}) and manganites (La_{0.75}Sr_{0.25}MnO_{3-δ}), are chemically incompatible either with one of the BCY and BZY phases or with both of them. However, the studied ferrites (Ba_{0.5}Sr_{0.5}FeO_{3-δ}) and nickelates (LaNi_{0.6}Fe_{0.4}O_{3-δ} and La₂NiO_{4+δ}) showed no interaction with both the BCY and BZY phases.

Tolchard and Grande³⁵⁰ applied more stringent conditions (1100 °C for 72 h) to reveal the interaction abilities of LaMnO₃, LaFeO₃, LaCoO₃, and La₂NiO₄ phases with BaZrO₃. Using XRD and SEM and EDX analyses, they found that LaMnO₃ is the most unsuitable oxide, which results in the formation of 12.2 wt% of an La₂Zr₂O₇ impurity phase according to the simplified reaction:



where M = Mn, Co or Fe.

For the couples of LaFeO₃/BaZrO₃ and La₂NiO₄/BaZrO₃, this impurity phase was also detected in amounts of 0.7 and 2.2 wt%, respectively. The highest chemical tolerance was reported for LaCoO₃/BaZrO₃, where no La₂Zr₂O₇ was formed after prolonged high-temperature calcination. However, this does not lead to the conclusion that LaCoO₃ is the most suitable for BaZrO₃ since cationic interdiffusion (without decomposition of the original phases or appearance of new ones) can also occur. For example, cobalt-based solutions in a wide concentration range, *i.e.* BaZr_{1-x}Co_xO_{3-δ} (0 ≤ x ≤ 0.4), can be formed,^{27,351} leading to significant disruption of the chemical compositions for both the basic LaCoO₃ and BaZrO₃ phases without the formation of any impurities. A similar situation has been described in other works,^{352,353} where Ba-enriched Ba_{0.5}Sr_{0.5}Co_{0.8}Fe_{0.2}O_{3-δ}/Ba-deficient BaCe_{0.9}Y_{0.1}O_{3-δ} and Co-enriched BaCe_{0.7}Zr_{0.1}Y_{0.2}O_{3-δ}/Y-enriched PrBaCo₂O_{5+δ} compositions were observed after prolonged high-temperature calcination.

Considering the model BaCeO₃/Ln₂NiO_{4+δ} pair as an example, Ni-dissolution in BaCeO₃ is limited to ~1 mol%;³⁵⁴ Ln-dissolution may be also minimised if BaCeO₃ is doped by acceptor dopants; Ba-dissolution in Ln₂NiO_{4+δ} is possible,³⁵⁵ but this improves the catalytic activity of the modified electrodes³⁵⁶ and is limited in the case of already Ba-doped nickelates (*i.e.* (Ln,Ba)₂NiO_{4+δ}); and finally, Ce-dissolution in the Ln₂NiO_{4+δ} parent phase is negligible. These features constitute quite

Table 4 Chemical compatibility of Ln₂NiO₄-based electrodes with Ba- and La-based proton-conducting electrolytes

Electrolyte	Electrode	Weight ratio	Calcination condition, T, °C/τ, h	Impurity phases (from XRD data)	Ref.
BaZrO ₃	La ₂ NiO _{4+δ}	1 : 1	1100/72	La ₂ Zr ₂ O ₇ (trace)	350
La _{28-x} W _{4+x} O _{54+3x/2}	Pr ₂ NiO _{4+δ}	1 : 1	800/2	Pr ₆ O ₁₁ (trace)	357
La _{5.5} WO _{11.25-δ}	La ₂ NiO _{4+δ}	1 : 1	1150/5	La ₆ W ₂ O ₁₅ (trace)	265
BaCe _{0.9} Y _{0.1} O _{3-δ}	Pr ₂ NiO _{4+δ}	1 : 1	1200/1	(Ce,Pr)O ₂ and NiO	231
BaCe _{0.7} Zr _{0.1} Y _{0.1} Yb _{0.1} O _{3-δ}	Nd ₂ NiO _{4+δ}	1 : 1	1200/3	No interaction	358
BaCe _{0.89} Gd _{0.1} Cu _{0.01} O _{3-δ}	La _{1.7} Ba _{0.3} NiO _{4+δ}	1 : 1	700/1000	BaO (trace)	359
BaCe _{0.8} Y _{0.2} O _{3-δ}	La ₂ NiO _{4+δ}	1 : 1	1100/10	No interaction	349
BaZr _{0.8} Y _{0.2} O _{3-δ}	La ₂ NiO _{4+δ}	1 : 1	1100/10	No interaction	349
BaZr _{0.1} Ce _{0.7} Y _{0.2} O _{3-δ}	Pr _{1.8} La _{0.2} Ni _{0.74} Cu _{0.21} Nb _{0.05} O _{4+δ}	1 : 1	950/3	No interaction	360
BaCe _{0.5} Zr _{0.3} Dy _{0.2} O _{3-δ}	Nd _{1.95} Ba _{0.05} NiO _{4+δ}	1 : 1	1100/10	No interaction	361
BaCe _{0.55} Zr _{0.3} Y _{0.15} O _{3-δ}	Pr ₂ NiO _{4+δ}	1 : 1	800, 900 1000, 1100 1200/2	(Ce,Pr)O ₂ (at T ≥ 900 °C)	362
BaZr _{0.1} Ce _{0.7} Y _{0.2} O _{3-δ}	La _{1.2} Sr _{0.8} Ni _{0.6} Fe _{0.4} O _{4+δ}	1 : 1	900/5	No interaction	363
BaCe _{0.5} Zr _{0.3} Dy _{0.2} O _{3-δ}	Pr _{1.9} Ba _{0.1} NiO _{4+δ}	1 : 1	1350/5	NiO	364
La ₂ Ce ₂ O _{7-δ}	Pr ₂ NiO _{4+δ}	1 : 1	1150	Pr ₆ O ₁₁ and La ₂ NiO _{4+δ}	365

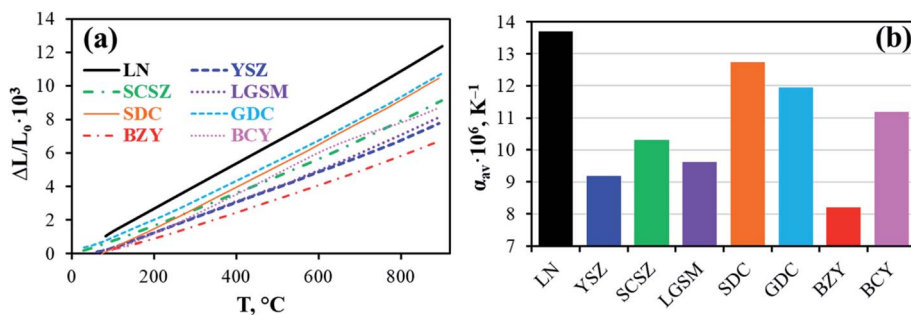


Fig. 11 Thermal expansion behaviour (a) and average TEC values (b) of some oxygen-ionic and proton-conducting electrolytes compared with LN. These data were taken from ref. 157 for LN, ref. 367 for YSZ and LGSM, ref. 368 for SDC, ref. 369 for GDC and SCSZ, and ref. 370 for BZY and BCY. Abbreviations: LN = $\text{La}_2\text{NiO}_{4+\delta}$, YSZ = $\text{Zr}_{0.9}\text{Y}_{0.1}\text{O}_{2-\delta}$, LGSM = $\text{La}_{0.9}\text{Sr}_{0.1}\text{Ga}_{0.8}\text{Mg}_{0.2}\text{O}_{3-\delta}$, SDC = $\text{Ce}_{0.8}\text{Sm}_{0.2}\text{O}_{2-\delta}$, GDC = $\text{Ce}_{0.9}\text{Gd}_{0.1}\text{O}_{2-\delta}$, SCSZ = $(\text{Sc}_2\text{O}_3)_{0.1}(\text{CeO}_2)_{0.01}(\text{ZrO}_2)_{0.89}$, BZY = $\text{BaZr}_{0.8}\text{Y}_{0.2}\text{O}_{3-\delta}$, and BCY = $\text{BaCe}_{0.8}\text{Y}_{0.2}\text{O}_{3-\delta}$.

encouraging results regarding the chemical compatibility of nickelates with state-of-the-art proton-conducting oxides, as shown in Table 4.

5.2. Mechanical compatibility with proton-conducting electrolytes

Components of solid oxide electrochemical systems are typically subjected to severe conditions under both fabrication of the cells (very high co-sintering temperatures) and their operation (reduced temperatures, but high gradients of electrochemically active components). Thus, to achieve excellent integrity of multi-layered structures with no further unacceptable consequences (electrode delamination, cracking and other failures), materials should be selected based on their thermo-(chemico-) mechanical properties. Generally, this issue has been thoroughly described by Løken *et al.*,³⁶⁶ who reviewed the thermal and chemical expansion features of proton-conducting electrolytes together with the compatibility aspects of their use with different electrode materials. To briefly summarise their main conclusions, suitable electrodes should exhibit TEC values close to that of the widely studied protonic conductors ($(8\text{--}12) \times 10^{-6} \text{ K}^{-1}$), featuring a low contribution from chemical expansion.

5.2.1. Thermomechanical expansion. A comparative analysis (Fig. 11) shows that nickelate materials are attractive electrodes, which demonstrate TECs closest to that of various solid oxide electrolytes, including proton-conducting materials. Although the TEC difference comprises about 2–3 respective units for a BCY/LN couple and 5–6 respective units for a BZY/LN couple, further adjustment of their thermal compatibility can be realised through the design of composite materials. These composites (combination of an electrode and an electrolyte with 10–50 wt% of the latter phase) have decreased TECs that follow an additive rule,

$$\alpha_{\text{composite}} = (1 - x)\alpha_{\text{electrode}} + x\alpha_{\text{electrolyte}}$$

where x is the weight fraction.

Together with composite materials, the TEC levels of $\text{Ln}_2\text{-NiO}_{4+\delta}$ -based materials can be widely tuned *via* the doping

approach. Table 5 lists some doped oxides and their average TECs determined within the entire studied temperature range.

5.2.2. Chemical expansion. Fairly low absolute levels of TECs achieved for $\text{Ln}_2\text{NiO}_{4+\delta}$ -based ceramics are combined with the very weak temperature dependence of TECs (as a differential form of dilatometry curve, Fig. 12). This implies that the chemical-induced effects (or an orthorhombic/tetragonal phase transition, if existing) insignificantly affect the overall expansion of nickelate materials compared to some widely studied Co- and Fe-based oxides. The latter can suffer from phase transition(s) or chemical-induced expansion, either leading to the corresponding local TEC burst within a narrow temperature range or increase in TEC in the high-temperature range compared with that at lower temperatures, as shown in Fig. 12b. For example, $\text{GdBaCo}_2\text{O}_{5+\delta}$ exhibits a close-to-linear dilatometry curve with a TEC of $(20 \pm 1) \times 10^{-6} \text{ K}^{-1}$; however, the structure of this double cobaltite is transformed from orthorhombic to tetragonal between 450 °C and 500 °C.^{386,387} At temperatures above 300 °C, $\text{Ba}_{0.5}\text{Sr}_{0.5}\text{Co}_{0.8}\text{Fe}_{0.2}\text{O}_{3-\delta}$ has a cubic-type perovskite structure,^{388–390} but chemical expansion occurs upon heating from 500 °C, increasing the TEC value by 2 times from $(11 \pm 1) \times 10^{-6} \text{ K}^{-1}$ at 100–400 °C to $(22 \pm 1) \times 10^{-6} \text{ K}^{-1}$ at 650–850 °C. The complex oxide of $\text{Y}_{0.8}\text{Ca}_{0.2}\text{BaCo}_4\text{O}_{7+\delta}$ with a swedenborgite structure type shows very low TECs of $(8\text{--}11) \times 10^{-6} \text{ K}^{-1}$; nevertheless, two specific temperatures (around 400 °C and 800 °C) can be distinguished when oxygen adsorption processes with subsequent oxygen desorption occur.^{391–393} This leads to an increase in TEC of up to 17×10^{-6} and $12 \times 10^{-6} \text{ K}^{-1}$, respectively.

The Ni-based Ruddlesden–Popper phases are attractive from the viewpoint of chemical-induced strain effects (Fig. 13), showing an inappreciable response in dimensional changes towards oxygen deviation (δ) from the stoichiometric values or oxygen partial pressure variations. This unique $p\text{O}_2$ -tolerance strain originates from the structural features of nickelates.³⁷⁶ Oxygen desorption of $\text{Ln}_2\text{NiO}_{4+\delta}$ results in two opposite effects, *i.e.* contraction of the c -parameters owing to the release of interstitial oxygen from the rock-salt layers and expansion of the perovskite-like layers (a – b plane) due to charge compensation by the partial reduction of existing cations (Ni^{3+}). The combination of these effects results in negligible overall expansion.

Table 5 Average thermal expansion coefficient values (α_{av}) of Ln₂-NiO_{4+δ}-based materials. In most cases, dilatometry measurements were performed in ambient air atmosphere between RT and 1000 °C. Visualisation of the data is presented in Fig. S3, ESI

Composition	$\alpha_{av} \times 10^6, K^{-1}$	Ref.
La₂NiO_{4+δ}		
La ₂ NiO _{4+δ}	12.6	114
	13.0	53, 72 and 371
	13.1	340
	13.5	372
	13.8	218
La _{1.95} Ba _{0.05} NiO _{4+δ}	13.2	373
La _{1.8} Sr _{0.2} NiO _{4+δ}	12.6	371 and 374
La _{1.75} Sr _{0.25} NiO _{4+δ}	11.2	339
La _{1.7} Sr _{0.3} NiO _{4+δ}	13.9	359
La _{1.7} Sr _{0.3} Ni _{0.9} Mn _{0.1} O _{4+δ}	15.3	171
La _{0.2} Sr _{1.8} NiO _{4+δ}	13.8	374
La _{1.8} Ca _{0.2} NiO _{4+δ}	14.5	131
La _{1.7} Ca _{0.3} NiO _{4+δ}	13.9	359
	14.2	132
La _{1.6} Ca _{0.4} Ni _{0.9} Fe _{0.1} O _{4+δ}	14.6	131
La _{1.6} Ca _{0.4} Ni _{0.9} Cu _{0.1} O _{4+δ}	14.9	131
La _{1.7} Ba _{0.3} NiO _{4+δ}	15.2	359
La ₂ Ni _{0.6} Cu _{0.4} O _{4+δ}	13.0	375
La ₂ Ni _{0.9} Co _{0.1} O _{4+δ}	12.8	204 and 205
La ₂ Ni _{0.9} Fe _{0.1} O _{4+δ}	13.8	376
	12.7	377
La ₂ Ni _{0.8} Cu _{0.2} O _{4+δ}	14.2	376
Pr₂NiO_{4+δ}		
Pr ₂ NiO _{4+δ}	13.2	378
	13.3	372
	13.4	72
	13.6	53
	13.9	379
	15.5	101
Pr _{1.95} Ba _{0.05} NiO _{4+δ}	13.9	373
PrLaNiO _{4+δ}	14.1	380
Pr _{1.7} Sr _{0.3} NiO _{4+δ}	12.0	268
	15.0	201
Pr _{1.2} Sr _{0.8} NiO _{4+δ}	12.9	268
Pr _{1.5} Sr _{0.5} Ni _{0.5} Co _{0.5} O _{4+δ}	13.1	177
Pr _{1.7} Sr _{0.3} Ni _{0.6} Cu _{0.4} O _{4+δ}	13.8	381
Pr ₂ Ni _{0.75} Cu _{0.25} Gd _{0.05} O _{4+δ}	12.7	382
Pr _{1.7} Ca _{0.3} NiO _{4+δ}	14.5	132
Pr _{1.6} Ca _{0.4} NiO _{4+δ}	13.7	101
Pr ₂ Ni _{0.9} Co _{0.1} O _{4+δ}	16.2	118
Pr ₂ Ni _{0.9} Mo _{0.1} O _{4+δ}	13.5	379
Nd₂NiO_{4+δ}		
Nd ₂ NiO _{4+δ}	12.7	53
	13.4	383
	14.5	384
	15.0	132
Nd _{1.95} Ba _{0.05} NiO _{4+δ}	13.4	373
Nd _{1.8} Sr _{0.2} NiO _{4+δ}	12.9	91
Nd _{1.6} Sr _{0.4} NiO _{4+δ}	13.0	385
Nd _{1.2} Sr _{0.8} NiO _{4+δ}	14.4	385
NdSrNiO _{4+δ}	12.3	108
Nd _{1.9} Ca _{0.1} NiO _{4+δ}	15.1	132
Nd _{1.8} Ca _{0.2} NiO _{4+δ}	14.3	132
Nd _{1.7} Ca _{0.3} NiO _{4+δ}	13.5	132

Conversely, defect formation and interaction upon oxygen desorption occur within the sole structure of the conventional perovskite- and fluorite-related materials. For Co- and Fe-based oxides, oxygen vacancies are also formed (that should contract the cell), but cation reduction and cation–cation repulsion have a greater influence, leading to overall chemical expansion.

Interesting results were obtained by Flura *et al.*⁷² in their study on the structural parameters of basic nickelates (La₂NiO_{4+δ}, Nd₂NiO_{4+δ}, and Pr₂NiO_{4+δ}) utilising high-temperature XRD analysis, revealing the effects of temperature, measurement atmosphere and phase transitions on the thermo-chemical response of the corresponding ceramics (Fig. 13c). Based on this analysis, decreasing *p*O₂ from the conventional value of air to $\sim 1 \times 10^{-4}$ atm (helium atmosphere) resulted in an apparent decrease in TEC across the entire temperature range. Simultaneously, the TEC behaviour of Pr₂NiO_{4+δ} was distinct from that of other nickelates, where its phase transition (*Bmab* → *I4/mmm*) decreased the TECs, while the phase transitions for La₂NiO_{4+δ} and Nd₂NiO_{4+δ} (*Fmmm* → *I4/mmm* occurred around 150 and 500 °C, respectively) were found to increase the TECs with respect to the low-temperature range. The dilatometry data of Berger *et al.*¹¹⁸ confirm that the TECs decreased with a reduction in *p*O₂ for a Pr-based nickelate (Pr₂Ni_{0.9}Co_{0.1}O_{4+δ}) within the low-temperature range of $12.2 \times 10^{-6} K^{-1}$ at *p*O₂ = 1 atm to $10.8 \times 10^{-6} K^{-1}$ at *p*O₂ = 1×10^{-2} atm. However, the TECs increased for the high-temperature range of 15.9×10^{-6} to $16.9 \times 10^{-6} K^{-1}$ due to the oxygen desorption mechanism. The difference between these two works is the low-temperature structure of praseodymium nickelate (*Bmab*⁷² and *Fmmm*¹¹⁸), implying that this can also affect the achieved TECs and their relation relative to each other in different temperature regions.

5.3. Proton transportation

The RP phases of the first order, A₂BO_{4+δ}, are typically hyperstoichiometric compounds having an excess of interstitial oxygen in their structure. It is evident that the appearance of proton transport (if existing) in A₂BO_{4+δ} occurs with different mechanism(s) compared with the conventional acceptor-doped perovskites, where proton defects are formed under dissociative adsorption of water molecules by existing oxygen vacancies:^{402–404}



In contrast, the interstitial sites in the classical Ln₂NiO_{4+δ} compounds are important for proton transportation since H₂O is more favourable for insertion at the interstitial sites, as shown in Fig. 14.

The protonation of oxides is generally achieved within a hydration process. The hydration equation for Ln₂BO_{4+x} can be written as:¹⁴⁴



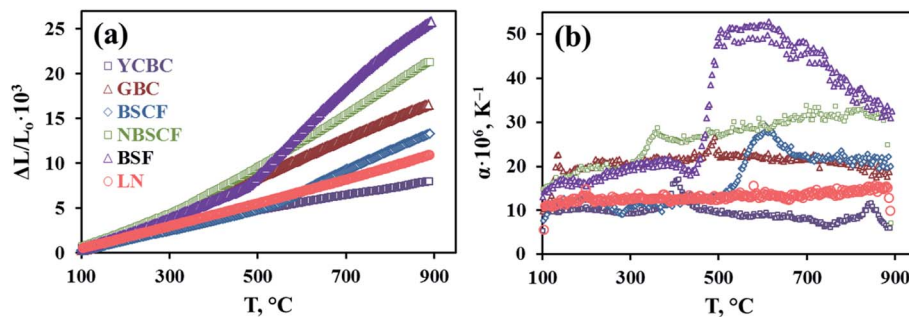


Fig. 12 Thermal expansion (a) and TEC values (b) of some electrode materials as a function of temperature (ambient air atmosphere). Data is presented based on experiments. Abbreviations: LN = $\text{La}_2\text{NiO}_{4+\delta}$, YCBC = $\text{Y}_{0.8}\text{Ca}_{0.2}\text{BaCo}_4\text{O}_{7+\delta}$, GBC = $\text{GdBaCo}_2\text{O}_{5+\delta}$, BSCF = $\text{Ba}_{0.5}\text{Sr}_{0.5}\text{Co}_{0.8}\text{Fe}_{0.2}\text{O}_{3-\delta}$, BSF = $\text{Ba}_{0.5}\text{Sr}_{0.5}\text{FeO}_{3-\delta}$, and NBSCF = $\text{NdBa}_{0.5}\text{Sr}_{0.5}\text{Co}_{1.5}\text{Fe}_{0.5}\text{O}_{5+\delta}$. Reproduced with permission.³⁴⁹ Copyright 2017, Elsevier.

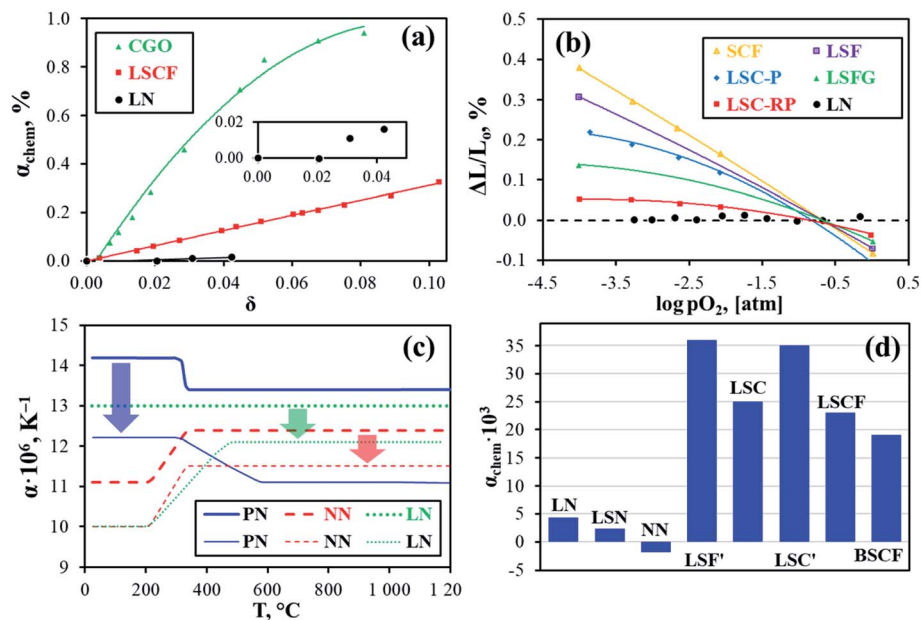


Fig. 13 Chemical strain effects for some oxide materials: (a) chemical expansion coefficient as a function of the oxygen non- (over-) stoichiometry and (b) dimensional change as a function of oxygen partial pressure at 800 °C. These graphs presented in ref. 376 and 394 were prepared based on the data in ref. 395–400. (c) Temperature dependence of TECs for nickelates under oxidising ($p\text{O}_2 = 0.2$ atm) and reducing (He, $p\text{O}_2 = 1 \times 10^{-4}$ atm) atmospheres.⁷² (d) Chemical expansion coefficients for some oxygen electrodes at 800 °C in air.^{91,120,401} Abbreviations: LN = $\text{La}_2\text{NiO}_{4+\delta}$, NN = $\text{Nd}_2\text{NiO}_{4+\delta}$, PN = $\text{Pr}_2\text{NiO}_{4+\delta}$, LSN = $\text{La}_{1.8}\text{Sr}_{0.2}\text{NiO}_{4+\delta}$, CGO = $\text{Ce}_{0.9}\text{Gd}_{0.1}\text{O}_{1.95-\delta}$, LSCF = $\text{La}_{0.6}\text{Sr}_{0.4}\text{Co}_{0.2}\text{Fe}_{0.8}\text{O}_{3-\delta}$, SCF = $\text{SrCo}_{0.8}\text{Fe}_{0.2}\text{O}_{3-\delta}$, LSF = $\text{La}_{0.3}\text{Sr}_{0.7}\text{FeO}_{3-\delta}$, LSF' = $\text{La}_{0.6}\text{Sr}_{0.4}\text{FeO}_{3-\delta}$, LSC-P = $\text{La}_{0.5}\text{Sr}_{0.5}\text{CoO}_{3-\delta}$, LSC = $\text{La}_{0.6}\text{Sr}_{0.4}\text{CoO}_{3-\delta}$, LSC' = $\text{La}_{0.3}\text{Sr}_{0.7}\text{CoO}_{3-\delta}$, LSFSG = $\text{La}_{0.3}\text{Sr}_{0.7}\text{Fe}_{0.6}\text{Ga}_{0.4}\text{O}_{3-\delta}$, LSC-RP = $\text{LaSrCoO}_{4+\delta}$, and BSCF = $\text{Ba}_{0.5}\text{Sr}_{0.5}\text{Co}_{0.2}\text{Fe}_{0.8}\text{O}_{3-\delta}$.

According to the equation, it seems that H_2O is split into OH and H, while OH occupies the interstitial site and H attaches to the lattice oxygen. It should be noted that this is only an assumption since little research activity has been carried out to determine the exact mechanism for hydration and proton transportation in $\text{Ln}_2\text{NiO}_{4+\delta}$ materials. However, this assumption is reasonable if one considers the loss of the interstitial oxygen in the classical $\text{Ln}_2\text{NiO}_{4+\delta}$ (such as $\text{La}_2\text{NiO}_{4+x}$) at high temperatures,⁶⁷ leaving the interstitial sites to be compensated by H_2O . Although the loss of the interstitial oxygen was observed in $\text{La}_2\text{NiO}_{4+x}$, no observation of oxygen vacancy was reported in this study. Li *et al.*²³² arrived at a similar conclusion. They studied the hydration ability of $\text{Pr}_2\text{NiO}_{4+x}$ and found that

the insertion of H_2O at the interstitial sites is the most likely explanation for the protonation of this material. Although there are three possible ways for the formation of proton defects in $\text{Pr}_2\text{NiO}_{4+x}$, the very low H_2 partial pressure at the cathode side eliminates the possibility of the direct combination of H_2 with interstitial oxygen. They also revealed that the insertion of H_2O at the oxygen vacancies through eqn (13) is not significant due to the very low oxygen vacancy content in the oxygen-rich environment for $\text{Pr}_2\text{NiO}_{4+x}$. Therefore, protonation can only occur with the insertion of H_2O at the interstitial sites. However, differing from the opinion of Grimaud *et al.*¹⁴⁴ that proton defects form at both interstitial sites and with lattice oxygen, Li

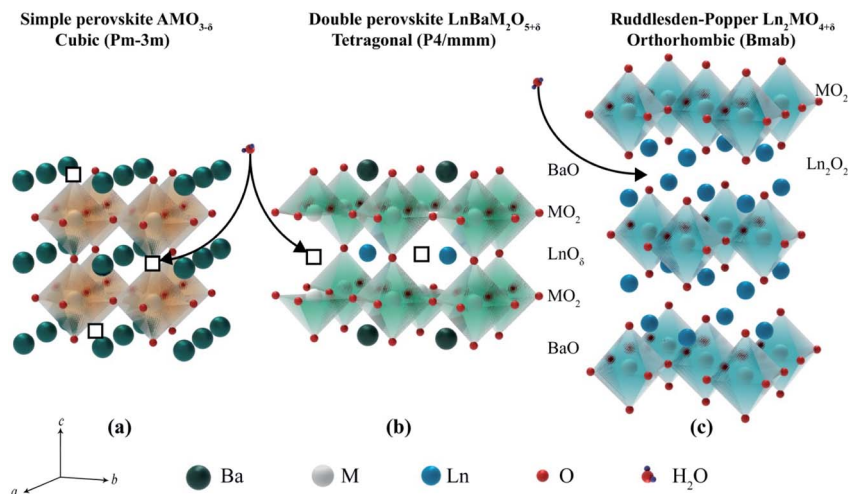
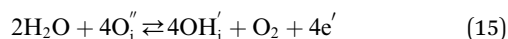


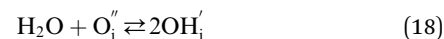
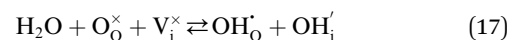
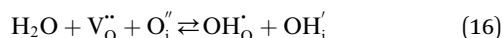
Fig. 14 Possible places for the insertion of water molecules in the different structures.

et al. indicated that the H_2O split reaction is only associated with the interstitial sites, with the reaction equation written as:



The difference in the opinion of researchers concerning the hydration process of $\text{Ln}_2\text{NiO}_{4+\delta}$ materials implies that this can be an interesting question for further study. Nevertheless, both studies agree that $\text{Ln}_2\text{NiO}_{4+\delta}$ has a different hydration mechanism in comparison with that for traditional ABO_{3-x} perovskite oxides, while the interstitial sites play an important role in the protonation.

For the RP phases with pronounced basic properties (for example, BaLaInO_4), the proton defects may be formed according to the following reactions:^{144,405–408}



The first two reactions require vacancy (lattice or interstitial) defects. These defects occur to a considerable degree in nickelates, even those that are not doped by acceptors (eqn (19)). In detail, the heating of $\text{Ln}_2\text{NiO}_{4+\delta}$ leads to oxygen desorption, and correspondingly the appearance of the necessary vacancies (eqn (20)), which are theoretically capable of providing hydration. The third reaction does not require crystallographic or interstitial vacancies, allowing the formation of proton defects directly upon water interaction with interstitial oxygen. Tarasova *et al.*⁴⁰⁷ used IR spectroscopy to reveal the two energetically non-equivalent hydroxyl groups in BaLaInO_4 and $\text{BaLaIn}_{0.9}\text{Nb}_{0.1}\text{O}_{4+\delta}$, confirming the possible realisation of eqn (14) and (15).

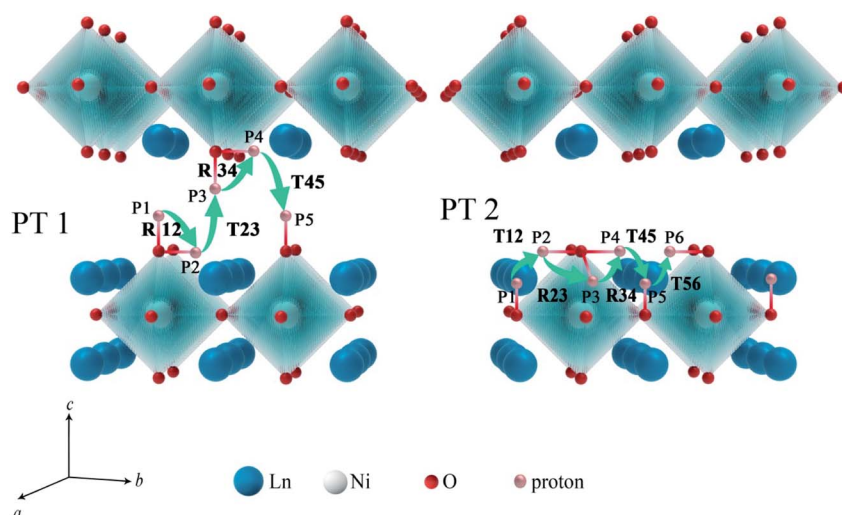
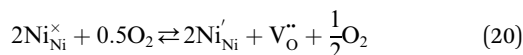
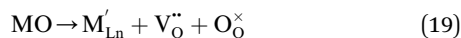


Fig. 15 Schematic representations of two paths for proton transport (PT) between the inter-layer PT1 and inner-layer PT2. P_n ($n = 1-6$) are the possible proton locations and R and T refer to proton rotation and transfer, respectively.³³²



Grimaud *et al.*¹⁴⁴ analysed the weight change of $\text{Pr}_2\text{NiO}_{4+\delta}$ in air with various $p\text{H}_2\text{O}$ levels (from 0.002 to 0.095 atm). This analysis revealed different weight changes depending on $p\text{H}_2\text{O}$, but could not determine the actual proton concentration in praseodymium nickelate due to the difficulty associated with two simultaneous processes, hydration/dehydration and oxygen sorption/desorption.

Zhang *et al.*³³² studied both oxygen migration and proton diffusivity in undoped and doped $\text{La}_2\text{NiO}_{4+\delta}$ using first-principle calculations, including analyses of relative energy, effective charge and electron density. They proposed a possible mechanism (Fig. 15) and found that proton transportation is unfavourable in a perfect $\text{La}_2\text{NiO}_{4+\delta}$ crystal; however, fast proton transport may occur for Co- and Cu-doped derivatives. It should be noted that unlike oxygen transport, proton migration is proposed to occur between the apical and equatorial oxygen ions with a resulting energy barrier of ~ 1.1 eV, having five potential insertion sites on oxygen ions. This fact implies that the migration of protons between two rock-salt layers is unfavourable in nickelates in terms of a very large energy barrier, which is in accordance with the hydration of other RP phases.^{409,410} However, it is also noted that the calculated proton transport route, whether rotating or jumping, is associated with the lattice oxygen only, and no interstitial oxygen is considered. As discussed above, the interstitial oxygen can play an important role in the protonation for $\text{Ln}_2\text{NiO}_{4+\delta}$, while the participation of interstitial oxygen may change the distance of proton migration, and thus alter the optimised migration routes. Therefore, it will be desirable to have a more comprehensive view concerning the first-principle calculations of proton transportation by also considering the interstitial oxygens. Although this aspect has yet to be considered in detail, it can be beneficial for an understanding of proton transportation in the $\text{Ln}_2\text{NiO}_{4+\delta}$ class of materials.

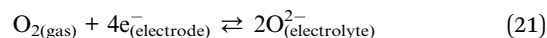
As can be seen above, the issue of the proton transportation in $\text{Ln}_2\text{NiO}_{4+\delta}$ phases remains open and should be evaluated in detail in future research.

5.4. Electrochemical activity towards oxygen- and proton-involving electrode processes

The electrochemical activity of electrodes depends on different parameters affecting the active zone where the electrochemical reactions occur. Among them, a number of parameters have a technology-related nature (particle size, tortuosity, and porosity), which regulates the triple phase boundary (TPB) length.^{411–415} Another set is related to the inherent properties of the phases, including oxygen and electron transport, which determine the activity of TPB. Although the complete separation of composition from technological parameters is a difficult task, some regularities can be revealed.

Oxygen electrodes of SOFCs or PCFCs allow the realisation of the oxygen reduction reaction (ORR):

For SOFCs:



For PCFCs:



This reaction occurs in the case of predominantly electronic conductors, such as Pt and LSM.⁴¹⁶ When materials can also conduct oxygen-ions, they become mixed ionic-electronic conductors (MIECs).^{417–422} MIECs have a distinct advantage over electronic conductors since the ORR can occur at the surface of the ceramic electrode together with TPB:

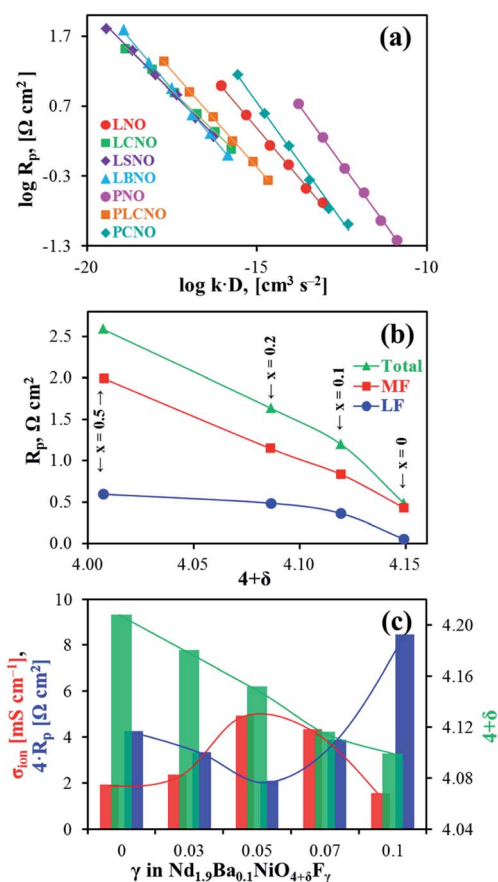


Fig. 16 Correlation of polarisation resistances of $\text{Ln}_2\text{NiO}_{4+\delta}$ -based electrodes (R_p) measured on the symmetrical cells with proton-conducting electrolytes with kinetic parameters (kD), oxygen content ($4 + \delta$) and ionic conductivity (σ_{ion}) of nickelates. Panels (a), (b) and (c) were reproduced from works by Sadykov *et al.*,²⁶⁷ Grimaud *et al.*¹⁴⁴ and Tarutin *et al.*,²⁰⁷ respectively. In panel (a) the following abbreviations are used: LNO = $\text{La}_2\text{NiO}_{4+\delta}$, LCNO = $\text{La}_{1.7}\text{Ca}_{0.3}\text{NiO}_{4+\delta}$, LSNO = $\text{La}_{1.7}\text{Sr}_{0.3}\text{NiO}_{4+\delta}$, LBNO = $\text{La}_{1.7}\text{Ba}_{0.3}\text{NiO}_{4+\delta}$, PNO = $\text{Pr}_2\text{NiO}_{4+\delta}$, PCNO = $\text{Pr}_{1.7}\text{Ca}_{0.3}\text{NiO}_{4+\delta}$, and PLCNO = $\text{Pr}_{0.85}\text{La}_{0.85}\text{Ba}_{0.3}\text{NiO}_{4+\delta}$. Panel (b) highlights the results obtained for the PSN|BCY|PSN symmetrical cells at 600 °C and $p\text{H}_2\text{O} = 0.03$ atm. Here, PSN = $\text{Pr}_{2-x}\text{Sr}_x\text{NiO}_{4+\delta}$, and BCY = $\text{BaCe}_{0.9}\text{Y}_{0.1}\text{O}_{3-\delta}$. In panel (c), all the data are provided for 600 °C and the R_p values were obtained for symmetrical cells based on proton-conducting $\text{BaCe}_{0.5}\text{Zr}_{0.3}\text{Y}_{0.1}\text{O}_{3-\delta}$ electrolyte.

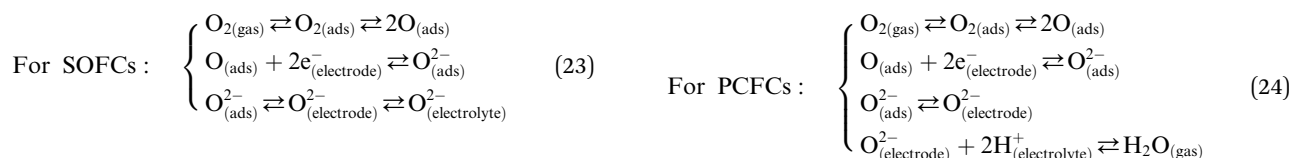


Table 6 Overall polarisation resistances (R_p) and corresponding activation energy (E_a) of nickelate-based electrodes for symmetrical cells, electrode|electrolyte|electrode. Visualisation of the data is presented in Fig. S4, ESI

Electrode	Electrolyte	$R_p, \Omega \text{ cm}^2$			$E_a, \text{ eV}$	Ref.
		500 °C	600 °C	700 °C		
La ₂ NiO _{4+δ}	BaCe _{0.9} Y _{0.1} O _{3-δ}	91.8	14.1	—	1.01	429
La ₂ NiO _{4+δ}	BaCe _{0.9} Y _{0.1} O _{3-δ}	41.6	3.88	—	1.01	81
La ₂ NiO _{4+δ}	La _{5.5} WO _{11.25-δ}	—	35	11.5	1.36	265
La ₂ NiO _{4+δ}	BaCe _{0.8} Y _{0.2} O _{3-δ}	—	20.8	4.94	1.01	349
La ₂ NiO _{4+δ}	BaCe _{0.5} Zr _{0.3} Dy _{0.2} O _{3-δ}	4.5	0.64	0.10	1.24	157
La ₂ Ni _{0.9} Cu _{0.1} O _{4+δ}	BaCe _{0.5} Zr _{0.3} Dy _{0.2} O _{3-δ}	4.7	0.92	0.21	0.96	157
La ₂ Ni _{0.8} Cu _{0.2} O _{4+δ}	BaCe _{0.5} Zr _{0.3} Dy _{0.2} O _{3-δ}	13.1	2.06	0.47	1.01	157
La ₂ Ni _{0.7} Cu _{0.3} O _{4+δ}	BaCe _{0.5} Zr _{0.3} Dy _{0.2} O _{3-δ}	42.3	7.90	1.20	1.08	157
La _{1.5} Pr _{0.5} NiO _{4+δ}	La _{5.5} WO _{11.25-δ}	—	18.4	2.52	1.39	265
70%La ₂ NiO _{4+δ} -30%LaNi _{0.6} Fe _{0.4} O _{3-δ}	BaZr _{0.1} Ce _{0.7} Y _{0.2} O _{3-δ}	—	13.4	2.09	1.24	430
50%La ₂ NiO _{4+δ} -50%LaNi _{0.6} Fe _{0.4} O _{3-δ}	BaZr _{0.1} Ce _{0.7} Y _{0.2} O _{3-δ}	—	15.5	2.34	1.26	430
30%La ₂ NiO _{4+δ} -70%LaNi _{0.6} Fe _{0.4} O _{3-δ}	BaZr _{0.1} Ce _{0.7} Y _{0.2} O _{3-δ}	—	19.9	2.92	1.27	430
50%La ₂ NiO _{4+δ} -50%LaNi _{0.6} Fe _{0.4} O _{3-δ}	BaZr _{0.1} Ce _{0.7} Y _{0.2} O _{3-δ}	—	5.42	0.99	1.08	431
La _{1.95} Ba _{0.05} NiO _{4+δ}	BaCe _{0.5} Zr _{0.3} Dy _{0.2} O _{3-δ}	37.9	5.56	1.11	1.08	432
La _{1.7} Ca _{0.3} NiO _{4+δ}	BaCe _{0.89} Gd _{0.1} Cu _{0.01} O _{3-δ}	—	10.8	1.88	1.24	433
La _{1.7} Sr _{0.3} NiO _{4+δ}	BaCe _{0.89} Gd _{0.1} Cu _{0.01} O _{3-δ}	—	5.99	0.74	1.47	433
La _{1.7} Ba _{0.3} NiO _{4+δ}	BaCe _{0.89} Gd _{0.1} Cu _{0.01} O _{3-δ}	—	4.38	0.64	1.44	433
La _{1.7} Ba _{0.3} NiO _{4+δ} -BaCe _{0.89} Gd _{0.1} Cu _{0.01} O _{3-δ}	BaCe _{0.7} Zr _{0.1} Y _{0.2} O _{3-δ}	—	1.52	0.21	1.35	433
La _{1.7} Ba _{0.3} NiO _{4+δ} -BaCe _{0.89} Gd _{0.1} Cu _{0.01} O _{3-δ}	BaCe _{0.89} Gd _{0.1} Cu _{0.01} O _{3-δ}	—	4.64	0.62	1.35	359
La _{1.7} Ca _{0.3} NiO _{4+δ} -BaCe _{0.89} Gd _{0.1} Cu _{0.01} O _{3-δ}	BaCe _{0.89} Gd _{0.1} Cu _{0.01} O _{3-δ}	—	6.14	1.14	1.21	359
La _{1.7} Sr _{0.3} NiO _{4+δ} -BaCe _{0.89} Gd _{0.1} Cu _{0.01} O _{3-δ}	BaCe _{0.89} Gd _{0.1} Cu _{0.01} O _{3-δ}	—	9.59	0.82	1.34	359
La _{1.7} Ba _{0.3} NiO _{4+δ} -BaCe _{0.89} Gd _{0.1} Cu _{0.01} O _{3-δ}	CaZr _{0.95} Sc _{0.05} O _{3-δ}	—	278	45	1.14	434
La _{1.7} Ca _{0.3} NiO _{4+δ} -BaCe _{0.89} Gd _{0.1} Cu _{0.01} O _{3-δ}	CaZr _{0.95} Sc _{0.05} O _{3-δ}	—	666	128	1.20	434
La _{1.7} Sr _{0.3} NiO _{4+δ} -BaCe _{0.89} Gd _{0.1} Cu _{0.01} O _{3-δ}	CaZr _{0.95} Sc _{0.05} O _{3-δ}	—	213	30.0	1.24	434
La _{1.2} Sr _{0.8} NiO _{4+δ}	BaCe _{0.7} Zr _{0.1} Y _{0.2} O _{3-δ}	1.58	0.29	0.07	0.93	435
BaCe _{0.68} Zr _{0.1} Y _{0.1} Yb _{0.1} Cu _{0.02} O _{3-δ} infiltrated with 42.2 wt% La _{1.2} Sr _{0.8} NiO _{4-δ}	BaCe _{0.68} Zr _{0.1} Y _{0.1} Yb _{0.1} Cu _{0.02} O _{3-δ}	1.34	0.20	0.04	1.15	436
LaSrNiO _{4+δ}	BaCe _{0.9} Y _{0.1} O _{3-δ}	—	2.04	0.32	1.73	81
Nd ₂ NiO _{4+δ}	BaCe _{0.9} Y _{0.1} O _{3-δ}	278	29.9	4.9	1.06	429
Nd ₂ NiO _{4+δ}	BaCe _{0.9} Y _{0.1} O _{3-δ}	81.1	6.75	3.5	1.06	81
Nd _{1.95} Ba _{0.05} NiO _{4+δ}	BaCe _{0.5} Zr _{0.3} Dy _{0.2} O _{3-δ}	24.6	3.42	0.45	1.25	432
60%Nd _{1.95} NiO _{4+δ} -40%BaZr _{0.1} Ce _{0.7} Y _{0.1} Yb _{0.1} O _{3-δ}	BaZr _{0.1} Ce _{0.7} Y _{0.1} Yb _{0.1} O _{3-δ}	—	15.4	1.87	1.33	358
50%Nd _{1.95} NiO _{4+δ} -50%BaZr _{0.1} Ce _{0.7} Y _{0.1} Yb _{0.1} O _{3-δ}	BaZr _{0.1} Ce _{0.7} Y _{0.1} Yb _{0.1} O _{3-δ}	—	9.55	1.47	1.24	358
50%Nd _{1.95} NiO _{4+δ} -50%BaZr _{0.1} Ce _{0.7} Y _{0.1} Yb _{0.1} O _{3-δ}	BaZr _{0.1} Ce _{0.7} Y _{0.1} Yb _{0.1} O _{3-δ}	—	7.06	1.21	1.23	358
Nd _{1.9} Ba _{0.1} NiO _{4+δ}	BaZr _{0.3} Ce _{0.5} Y _{0.1} Yb _{0.1} O _{3-δ}	136	17.9	2.67	1.30	207
Nd _{1.9} Ba _{0.1} NiO _{4+δ}	BaCe _{0.5} Zr _{0.3} Dy _{0.2} O _{3-δ}	115	15.9	1.8	1.40	437
Nd _{1.9} Ba _{0.2} NiO _{4+δ}	BaCe _{0.5} Zr _{0.3} Dy _{0.2} O _{3-δ}	212	21.4	3.5	1.30	437
Nd _{1.9} Ba _{0.1} NiO _{4+δ} F _{0.05}	BaZr _{0.3} Ce _{0.5} Y _{0.1} Yb _{0.1} O _{3-δ}	63.1	7.82	0.41	1.40	207
Nd _{1.9} Ba _{0.1} NiO _{4+δ} F _{0.1}	BaZr _{0.3} Ce _{0.5} Y _{0.1} Yb _{0.1} O _{3-δ}	259	33.1	5.09	1.34	207
NdSrNiO _{4+δ}	BaCe _{0.9} Y _{0.1} O _{3-δ}	93.2	1.62	0.27	1.54	81
Pr ₂ NiO _{4+δ}	BaCe _{0.9} Y _{0.1} O _{3-δ}	6.71	1.7	0.38	0.87	429
Pr ₂ NiO _{4+δ}	BaCe _{0.9} Y _{0.1} O _{3-δ}	3.7	0.54	0.18	1.02	144
Pr ₂ NiO _{4+δ}	BaCe _{0.9} Y _{0.1} O _{3-δ}	6.75	0.49	0.14	0.86	81
Pr ₂ NiO _{4+δ}	BaCe _{0.9} Y _{0.1} O _{3-δ}	1.83	0.32	0.13	0.97	231
Pr ₂ NiO _{4+δ}	BaCe _{0.9} Y _{0.1} O _{3-δ}	9.17	0.89	0.19	0.96	252
(Pr _{0.9} La _{0.1}) ₂ (Ni _{0.74} Cu _{0.21} Nb _{0.05})O _{4+δ}	BaCe _{0.7} Zr _{0.1} Y _{0.2} O _{3-δ}	5.07	0.77	0.17	1.03	360
Pr _{1.9} Ca _{0.1} NiO _{4+δ}	BaCe _{0.89} Gd _{0.1} Cu _{0.01} O _{3-δ}	—	3.67	0.51	1.47	433
Pr _{1.95} Ba _{0.05} NiO _{4+δ}	BaCe _{0.5} Zr _{0.3} Dy _{0.2} O _{3-δ}	10.0	0.62	0.19	1.19	434
Pr _{1.9} Sr _{0.1} NiO _{4+δ}	BaCe _{0.9} Y _{0.1} O _{3-δ}	9.92	1.16	0.21	1.22	144
Pr _{1.8} Sr _{0.2} NiO _{4+δ}	BaCe _{0.9} Y _{0.1} O _{3-δ}	14.5	1.92	0.39	1.18	144
Pr _{1.5} Sr _{0.5} NiO _{4+δ}	BaCe _{0.9} Y _{0.1} O _{3-δ}	30.1	2.7	0.45	1.26	144
Pr _{1.2} Sr _{0.8} NiO _{4+δ}	BaCe _{0.7} Zr _{0.1} Y _{0.2} O _{3-δ}	3.47	0.57	0.13	0.98	435

Therefore, the TPB length is not limited by the contact of three phases, and this length can be extended due to additional pathways for oxygen molecules.

Despite having an ionic electrolyte type, the ORR comprises a combination of two consequent macroscopic processes, namely oxygen exchange at the surface of the electrodes and oxygen diffusion within the ceramic phase. On the one hand, these processes are characterised by kinetic parameters (oxygen exchange constant, k , and oxygen diffusion coefficient, D); on the other hand, they determine the polarisation resistance of the electrodes (R_p), as shown in particular by the ALS (Adler, Lane, Steele) model.⁴²³ Therefore, it is evident that there is a direct relation between R_p , k , and D . As can be seen from Fig. 16a, this correlation indeed exists, indicating that the lowest R_p values can be achieved for materials having the highest product of kD .

Grimaud *et al.* evaluated the electrochemical activity of Sr-doped $\text{Pr}_2\text{NiO}_{4+\delta}$ electrodes in the system with a $\text{BaCe}_{0.9}\text{Y}_{0.1}\text{O}_{3-\delta}$ protonic conductor, and found that the optimal electrode performance was observed for the undoped $\text{Pr}_2\text{NiO}_{4+\delta}$ having a higher $4 + \delta$ level.¹⁴⁴ In detail, both partial (middle- and low-frequency) resistances, related with the charge transfer through the interface and the electrode reactions, respectively, decreased

with $4 + \delta$ growth (Fig. 16b). Most probably, the “ $R_p-(4 + \delta)$ ” relation is a special case that overlays with other tendencies. For example, no direct “ $R_p-(4 + \delta)$ ” correlation was revealed in the work of Tarutin *et al.*²⁰⁷ Instead, the electrochemical activity of the $\text{Nd}_2\text{NiO}_{4+\delta}$ -based electrodes was regulated by the oxygen-ionic conductivity (Fig. 16c) or oxygen diffusion coefficient, according to the Nernst–Einstein relationship.

Table 6 summarises the $\text{Ln}_2\text{NiO}_{4+\delta}$ -based electrodes obtained for symmetrical cells with proton-conducting electrolytes. Although the polarisation resistances vary across a wide range (~ 3 orders of magnitude), the target values, after excluding the extreme examples, can be estimated to be ~ 10 , 3 and $0.5 \Omega \text{ cm}^2$ at 500, 600 and 700 °C, respectively, with a corresponding activation energy of ~ 1 eV. Analysis of the activation energies shows that they drop in the range of ~ 0.9 – 1.5 eV, implying that kinetic parameters (see Table 3) regulate the overall electrochemical activity of the electrodes.

The high noise of the listed R_p results is due to the technological features of the various materials. As can be seen, the compositions of the electrodes include basic nickelates and their doped or co-doped analogues and composites, which can be prepared by conventional means or utilising attractive techniques for the improvement of electroactivity (for example,

Table 7 Literature survey on the analysis of impedance spectra performed for the symmetrical ED|ET|ED cells, where ED is the electrode and ET is the electrolyte

ET composition	ED composition	Conditions	Equivalent circuit	Description	Ref.
$\text{BaCe}_{0.9}\text{Y}_{0.1}\text{O}_{3-\delta}$	$\text{La}_2\text{NiO}_{4+\delta}$	Wet air, $p\text{H}_2\text{O} = 0.03$ atm	$(RQ)_{\text{MF}}-(RQ)_{\text{LF}}$	MF: ionic transfer reaction at the ED/ET interface LF: oxygen dissociation and oxygen reduction reaction	81
$\text{BaCe}_{0.9}\text{Y}_{0.1}\text{O}_{3-\delta}$	$\text{Pr}_2\text{NiO}_{4+\delta}$	Wet air, $p\text{H}_2\text{O} = 0.03$ atm	$(RQ)_{\text{MF}}-(RQ)_{\text{LF}}$	MF: H^+ charge transfer at the ED/ET interface LF: oxygen adsorption, oxygen dissociation and molecular diffusion	439
$\text{BaCe}_{0.9}\text{Y}_{0.1}\text{O}_{3-\delta}$	$\text{Pr}_2\text{NiO}_{4+\delta}$	Wet air, $p\text{H}_2\text{O} = 0.03$ – 0.3	$(RQ)_{\text{MF}}-(RQ)_{\text{LF}}$	MF: H^+ charge transfer at the ED/ET interface LF: water formation or water gas diffusion	144
$\text{BaCe}_{0.9}\text{Y}_{0.1}\text{O}_{3-\delta}$	$\text{Pr}_2\text{NiO}_{4+\delta}$	Wet air, $p\text{H}_2\text{O} = 0.2$	$(RQ)_{\text{MF}}-(RQ)_{\text{LF}}$	MF: H^+ charge transfer at the ED/ET interface LF: oxygen dissociative adsorption or oxygen reduction reaction	231
$\text{BaZr}_{0.7}\text{Ce}_{0.2}\text{Y}_{0.1}\text{O}_{3-\delta}$	$\text{La}_2\text{NiO}_{4+\delta}$	Wet air, $p\text{H}_2\text{O} = 0.03$	$(RQ)_1-(RQ)_2-(RQ)_3$	1: charge transfer at the ED/ET interface 2: oxygen adsorption 3: molecular oxygen diffusion	440
$\text{BaCe}_{0.7}\text{Zr}_{0.1}\text{Y}_{0.2}\text{O}_{3-\delta}$ (BCZY)	$\text{La}_2\text{NiO}_{4+\delta}$ and $\text{La}_2\text{NiO}_{4+\delta}$ - $\text{LaNi}_{0.6}\text{Fe}_{0.4}\text{O}_{3-\delta}$ composites	—	$(RQ)_{\text{HF}}-(RQ)_{\text{LF}}$	HF: O^{2-} charge transfer at the ED/ET interface LF: oxygen adsorption, dissociation, charge transfer and molecular diffusion	430
BCZY	BCZY- $\text{Nd}_{1.95}\text{NiO}_{4+\delta}$	Wet air, $p\text{H}_2\text{O} = 0.03$	$(RQ)_{\text{HF}}-(RQ)_{\text{MF}}-(RQ)_{\text{LF}}$	HF: H^+ charge transfer at the ED/ET interface MF: oxygen reduction reaction LF: diffusion process of O^- to TPB	358
BCZY	$\text{La}_2\text{NiO}_{4+\delta}$ - $\text{LaNi}_{0.6}\text{Fe}_{0.4}\text{O}_{3-\delta}$	—	$(RQ)_{\text{HF}}-(RQ)_{\text{LF}}$	HF: O^{2-} charge transfer at the ED/ET interface LF: oxygen adsorption, dissociation, charge transfer and molecular diffusion	431
BCZY	$(\text{Pr}_{0.9}\text{La}_{0.1})_2\text{Ni}_{0.74}\text{Cu}_{0.21}\text{Nb}_{0.05}\text{O}_{4+\delta}$	—	$(RQ)_{\text{HF}}-(RQ)_{\text{LF}}$	HF: H^+ charge transfer LF: oxygen surface exchange	360
$\text{BaCe}_{0.5}\text{Zr}_{0.3}\text{Dy}_{0.2}\text{O}_{3-\delta}$	$\text{Nd}_{1.95}\text{Ba}_{0.05}\text{NiO}_{4+\delta}$	Dry air	$(RQ)_{\text{HF}}-(RQ)_{\text{MF}}-(RQ)_{\text{LF}}$	HF: charge transfer across the electrode/electrolyte interface MF: oxygen dissociation and surface diffusion LF: oxygen adsorption and gas-phase diffusion	361
BCZY	$\text{Ln}_{1.2}\text{Sr}_{0.8}\text{NiO}_{4+\delta}$ (Ln = La and Pr)	Ambient air	$(RQ)_{\text{HF}}-(RQ)_{\text{LF}}$	HF: bulk charge transfer process LF: —	435
$\text{BaCe}_{0.6}\text{Zr}_{0.2}\text{Y}_{0.2}\text{O}_{3-\delta}$ (BCZY')	$\text{Pr}_2\text{NiO}_{4+\delta}$ -BCZY'	Wet air, $p\text{H}_2\text{O} = 0.6$	$(RQ)_{\text{HF}}-(RQ)_{\text{LF}}$	HF: — LF: —	232

infiltration). Moreover, depending on the compositions of the cells and external conditions, the $\text{Ln}_2\text{NiO}_{4+\delta}$ -based phases are reported to show proton transportation, thus constituting the class of triple-conducting materials.^{424–428,438} Thus, considering the above-mentioned factors, further elaboration will specify the important details affecting the electrochemical performance of the considered electrode materials.

Analysing the nature of ongoing electrode processes, it is rational to consider an algorithm for decoding the impedance spectra collected for symmetrical cells. According to Table 7, the corresponding spectra are described by two or three RQ -combinations (R is the partial resistance of R_p , while Q is the constant phase element). If the first of these combinations is mostly due to an ionic charge transfer between the electrolyte and electrode phases, the second (or third) combination(s) may be attributed to various processes, starting from the reduction of oxygen atoms and ending with molecular diffusion of gas components within a porous electrode. Again, this uncertainty in physical models occurs due to completely different electrochemical systems that have varying functional parameters.

Among the numerous publications, there are a few works in which the authors tried to distinguish the factors associated with the inherent properties of nickelate phases and their microstructural parameters from each other.

For example, Grimaud *et al.*¹⁴⁴ studied the simultaneous effects of $p\text{O}_2$ and $p\text{H}_2\text{O}$ on the R_p of the $\text{Pr}_2\text{NiO}_{4+\delta}$ electrode at 600 °C. According to their results, R_p comprises the sum of two

(medium- (MF) and low- (LF) frequency) processes. R_{MF} is not affected by $p\text{H}_2\text{O}$, but depends on the variation of $p\text{O}_2$ according to the following relation: $R_{\text{MF}} \sim (p\text{O}_2)^{-1/4}$. On the contrary, the power function, n , for the $R_{\text{LF}} \sim (p\text{O}_2)^{-n}$ relation changes from 0.44 for dry air ($p\text{H}_2\text{O} = 0.006$ atm) to 0.61 for wet air ($p\text{H}_2\text{O} = 0.20$ atm) due to the involved $p\text{H}_2\text{O}$ -associated processes.

In the next work of Grimaud *et al.*,⁴⁴¹ special attention was paid to the electrode performance of $\text{Pr}_2\text{NiO}_{4+\delta}$ depending on the variation in $p\text{H}_2\text{O}$ and microstructural parameters. For a porous state of $\text{Pr}_2\text{NiO}_{4+\delta}$, the following tendencies were observed: $R_{\text{MF}} \sim (p\text{H}_2\text{O})^{-1/2}$ and $R_{\text{LF}} \sim (p\text{H}_2\text{O})^{-1}$. Their study indicated that the H_2O -assisted mechanism occurred for the considered system, namely proton charge transfer in the former case and water formation in the latter case. When the $\text{Pr}_2\text{NiO}_{4+\delta}$ electrode layer was prepared in a dense form, the first relation was again observed, confirming the ability of the nickelate to demonstrate proton transportation. However, no dependence ($n = 0$) was observed between R_{LF} and $p\text{H}_2\text{O}$ that could be explained in terms of the limited diffusion of water molecules inside the electrodes.

Quarez *et al.*³⁵⁷ considered the effects of several parameters on the electrochemical activity of the same electrode, *i.e.* calcination temperature to fabricate the PN|LW|PN symmetrical cells, the thickness of the PN electrodes, and weight amount of LW phases in the PN-LW electrode composites (here PN = $\text{Pr}_2\text{NiO}_{4+\delta}$ and LW = $\text{La}_{27.15}\text{W}_{4.85}\text{O}_{55+\delta}$). Temperature- and thickness-related effects were predictable, where an

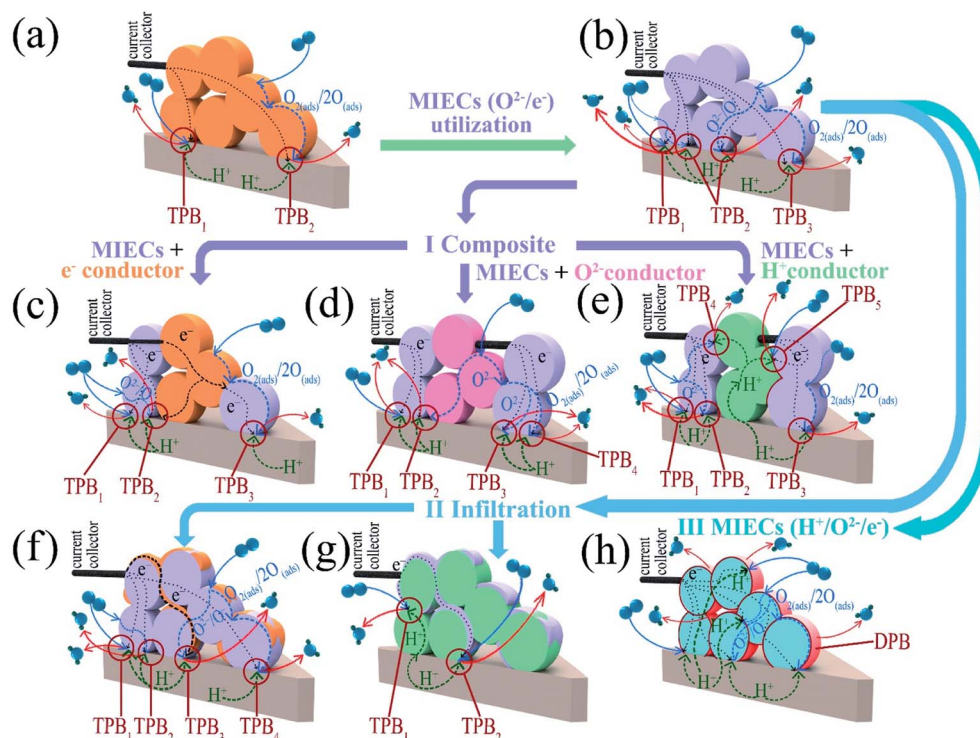


Fig. 17 Possible ways of electrochemical reactions in systems with proton-conducting electrolytes depending on the nature of the electrodes: (a) single-phase electronic conductor (EC), (b) single-phase MIEC, (c) MIEC + EC composite, (d) MIEC + O^{2-} -electrolyte, (e) MIEC + H^+ -electrolyte, (f) MIEC infiltrated with EC, (g) H^+ -electrolyte infiltrated with MIEC and (h) ideal single-phase triple-conducting ($\text{H}^+/\text{O}^{2-}/e^-$) electrode. Here, TPB is the triple phase boundary and DPB is the double phase boundary. Solid arrows correspond to the gas phases, while dashed arrows correspond to the ceramic phases.

improvement in electrochemical activity occurred for the highly porous electrodes (prepared at the lowest sintering temperature of 800 °C) and with the lowest thickness (12 μm against 24 and 36 μm for the other cases), implying that the determining role is played by molecular diffusion. However, no positive composition effect was observed upon the addition of the LW phase; therefore, composite materials do not always provide an incremental improvement in electrode functionality.

Technological effects were also evaluated by Solís *et al.*²⁶⁵ Here it was found that among three sintering temperatures (1050 °C, 1100 °C and 1150 °C), the best electrochemical activity for $\text{La}_{1.5}\text{Pr}_{0.5}\text{Ni}_{0.8}\text{Co}_{0.2}\text{O}_{4+\delta}$ electrodes was achieved for the lowest temperature, confirming the crucial effect of electrode porosity.

From the provided examples, it is clear that the electrochemical activity of nickelates can be quite easily tuned by technological factors, especially sintering temperature, ensuring a certain electrode porosity. However, the performance of these electrodes can be also regulated by means of engineering techniques aimed at extending the surface of the electrochemically active zone.

Fig. 17 shows some of the main strategies associated with increasing the number of active parts in electrochemical reactions. These strategies aim at introducing an additional charge carrier together with the electron carrier, *i.e.* either oxygen-ions, protons or both.

A gradual complication of the provided scheme consists of substituting a pure electron conductor (Fig. 17a) with a mixed ionic-electronic conductor (MIEC) with O^{2-} -transportation (Fig. 17b). Many complex oxides belong to these MIECs, including cobaltites,^{442–444} ferrites,^{434–448} nickelates^{52,234,379} having simple and layered structures, and solid solutions based on these classes.^{449–452} Utilisation of MIECs deposited on proton-conducting electrolytes allows the TPB to be extended by an MIEC phase perimeter limited by the electrolyte surface.

Another strategy for increasing the TPB involves the development of composite systems. Considering (O^{2-}/h^+)-MIEC as an example, three different types of composites can be formed (Fig. 17c–e), consisting of an MIEC combined with an electronic, oxygen-ionic or protonic conductor. The last combination seems to represent the most promising variant since it allows transportation of three different types of charge carriers, some of which exist within one phase, while others exist within the second phase.

An increase in the TPB can be realised by means of nano-scaled sediments formed purposefully on the surface of the main porous phases (Fig. 17f and g). This method, which is known as infiltration, is widely used to achieve high performance electrodes.^{25,453–455} However, it should be noted that the number of active parts determining the TPB length may be lower than that for single-phase MIECs (see the comparison of Fig. 17b and g). Nevertheless, in most cases, this accelerates the

Table 8 Methods for improving the electrochemical performances of Ln_2NiO_4 -based electrodes, where R_p is the polarisation resistance determined for the symmetrical ED|ET|ED cells at 600 °C

Case (see Fig. 17)	Example, ED ^a ET ^b	Performance		
		R_p , Ω cm ²	Ref.	Remarks
Single-phase materials				
(b)	LN BCY20	20.8	349	
	NBN BCZD	13.9	361	
Composite materials				
(c)	LN-LNF BCZY	13.4	430	LN : LNF = 7 : 3 (wt ratio)
	LN-LNF BCZY	19.9	430	LN : LNF = 3 : 7 (wt ratio)
	LN-LNF BCZY	5.4	431	LN : LNF = 1 : 1 (wt ratio)
(d)	LNF-SDC BCZY	7.2	431	LNF : SDC = 1 : 1 (wt ratio)
	LBN-SDC BCGC	7.8	433	LBN : SDC = 1 : 1 (wt ratio) + LNF current collector
(e)	NN-BCZYYb BCZYYb	7.24	358	NN : BCZYYb = 1 : 1 (wt ratio)
	LBN-BCGC BCGC	4.6	359	LBN : BCGC = 1 : 1 (wt ratio)
	LBN-BCGC BCGC	4.3	433	LBN : BCGC = 1 : 1 (wt ratio) + LNF current collector
Infiltration				
(f)	LNF _{inf} -LN _{bb} BCZY	0.31	459	31 wt% of infiltration component
(g)	LN _{inf} -BZCY _{bb} BZCY	29.3	440	
	PLN _{inf} -BCZY _{bb} BCZY	0.76	360	46.1 wt% of infiltration component
Single-phase triple-conducting material				
(h)	PN BCY	0.89	144	$p\text{H}_2\text{O} = 0.03$ atm (0.31 Ω cm ² at $p\text{H}_2\text{O} = 0.30$ atm)

^a Electrode (ED) abbreviations: PSN = $\text{Pr}_{1.4}\text{Sr}_{0.6}\text{NiO}_{4+\delta}$, LN = $\text{La}_2\text{NiO}_{4+\delta}$, NBN = $\text{Nd}_{1.95}\text{Ba}_{0.05}\text{NiO}_{4+\delta}$, LNF = $\text{LaNi}_{0.6}\text{Fe}_{0.4}\text{O}_{3-\delta}$, NN = $\text{Nd}_{1.95}\text{NiO}_{4+\delta}$, LBN = $\text{La}_{1.7}\text{Ba}_{0.3}\text{NiO}_{4+\delta}$, PLN_{inf} = $(\text{Pr}_{0.9}\text{La}_{0.1})_2\text{Ni}_{0.74}\text{Cu}_{0.21}\text{Nb}_{0.05}\text{O}_{4+\delta}$, PN = $\text{Pr}_2\text{NiO}_{4+\delta}$. ^b Electrolyte (ET) abbreviations: BCY = $\text{BaCe}_{0.9}\text{Y}_{0.1}\text{O}_{3-\delta}$, BCY20 = $\text{BaCe}_{0.8}\text{Y}_{0.2}\text{O}_{3-\delta}$, BCZD = $\text{BaCe}_{0.5}\text{Zr}_{0.3}\text{Dy}_{0.2}\text{O}_{3-\delta}$, BCZY = $\text{BaCe}_{0.7}\text{Zr}_{0.1}\text{Y}_{0.2}\text{O}_{3-\delta}$, SDC = $\text{Ce}_{0.8}\text{Sm}_{0.2}\text{O}_{2-\delta}$, BCGC = $\text{BaCe}_{0.89}\text{Gd}_{0.1}\text{Cu}_{0.01}\text{O}_{3-\delta}$, BCZYYb = $\text{BaCe}_{0.7}\text{Zr}_{0.1}\text{Y}_{0.2}\text{Yb}_{0.1}\text{O}_{3-\delta}$, BZCY = $\text{BaZr}_{0.7}\text{Ce}_{0.2}\text{Y}_{0.1}\text{O}_{3-\delta}$, inf is the infiltration, and bb is the backbone.

electrochemical reactions, thus promoting the higher performance of electrodes and cells based thereupon.

The last example represents (Fig. 17h) a case when the electrochemically active zone for triple-conducting materials is dramatically increased, where a double phase boundary (DPB) replaces the TPB, which is limited by the contact of three phases. Specifically, the entire surface of the single-phase triple-conducting electrode becomes active towards the oxygen reduction and water evolution reactions. In this case, there are three types of charge carriers (as in the case of the composites presented in Fig. 17e), which simultaneously exist within the same phase.

The ability of these phases to show triple-conducting behaviour is presently under discussion. For example, there are reports confirming the hydration of the nickelate phases;^{444,441} however, no direct confirmation of the data has been

presented. Moreover, the term “triple-conducting” should mean that all three partial (electronic, oxygen-ionic and protonic) conductivities are comparable. This has not been achieved for any state-of-the-art electrode system at 600–800 °C, where only temperatures as low as 200–400 °C allow the promotion of sufficient mobility/concentration of protons.^{456–458}

To move from theoretical to experimental aspects, the research data corresponding to the above-mentioned examples of electrode systems is presented in Table 8. According to these observations, strategies related to infiltration and the design of triple-conducting materials are identified as the most reliable, resulting in the achievement of a polarisation resistance of less than 1 Ω cm² at 600 °C. It is important to note that Section 5.4 reports data obtained for symmetrical cells, when the opposite electrode sides operate under the same conditions. In the real

Table 9 Design and performance of PCFCs and PCECs with nickelate-based oxygen (steam) electrodes under OCV conditions at 600 °C, where U_{OC} is the open-circuit voltage value, R_o , R_p , and R_t are the ohmic, polarisation and total resistance, respectively, and σ is the conductivity of the thin-film electrolyte. Visualisation of the data is presented in Fig. S5, ESI

Fuel electrode	Electrolyte ^a (thickness)	Oxygen electrode ^b	Electrochemical characteristics					Year	Ref.
			U_{OC} , V	R_o , Ω cm ²	R_p , Ω cm ²	R_t , Ω cm ²	σ , mS cm ⁻¹		
Ni-BCY	BCY (40 μm)	PN	1.15	1.84	2.76	4.60	2.2	2010	252
Ni-BCY	BCY (27 μm)	NN	1.06	—	—	4.8	—	2013	460
Ni-BCY	BCY (50 μm)	PN	1.09	0.81	0.8	1.61	6.2	2014	461
Ni-BCZY	BCZY (20 μm)	LN	1.04	0.64	0.96	1.60	3.1	2014	430
Ni-BCZY	BCZY (20 μm)	70%LN-30% LNF	1.04	0.44	0.49	0.93	4.5	2014	430
Ni-BCZY	BCZY (20 μm)	50% LN-50% LNF	1.05	0.50	0.51	1.01	4.0	2014	430
Ni-BCZY	BCZY (20 μm)	30% LN-70% LNF	1.04	0.53	0.57	1.10	3.8	2014	430
Ni-BCZY	BCZY (24 μm)	50% LN-50% LNF	1.04	0.54	0.59	1.13	4.4	2015	431
Ni-BZY	BCZY44 (5 μm)	PN	1.03	0.77	1.00	1.77	0.6	2015	462
Ni-BCZY	BCZY (12 μm)	PLNCN	1.01	0.33	0.32	0.65	3.6	2017	360
Ni-BCZD	BCZD (15 μm)	NBN	0.97	0.89	0.44	1.33	1.7	2018	361
Ni-BCZY	BCZY (15 μm)	PS0.8N	1.03	0.40	2.17	2.57	3.7	2018	435
Ni-BCZY	BCZY (15 μm)	LS0.8N	1.03	0.34	1.48	1.82	4.4	2018	435
Ni-BCZY15	BCZY15 (5 μm)	PN	1.02	0.08	0.28	0.36	6.2	2018	362
Ni-BCZY	BCZY (20 μm)	LN	1.03	0.36	0.88	1.24	5.5	2018	459
Ni-BCZY	BCZY (20 μm)	LN-13 wt% LNF	1.03	0.37	0.36	0.73	5.4	2018	459
Ni-BCZY	BCZY (20 μm)	LN-23 wt% LNF	1.01	0.37	0.34	0.71	5.4	2018	459
Ni-BCZY	BCZY (20 μm)	LN-31 wt% LNF	0.99	0.29	0.31	0.60	6.8	2018	459
Ni-BCZY	BCZY (20 μm)	LN-37 wt% LNF	0.99	0.41	0.54	0.95	4.9	2018	459
Ni-BCZY62	BCZY62 (20 μm)	PN	0.98	0.22	0.71	0.93	9.0	2018	232
Ni-BCGC	BCGC (25 μm)	PCN-BCGC LNF ^c	1.08	—	—	1.86	—	2018	463
Ni-BCZY	BCZY (15 μm)	LSNF	1.06	0.29	0.41	0.70	5.1	2019	363
Ni-BCZD	BCZD (25 μm)	PB10N-BCZD	1.08	0.52	0.39	0.91	4.8	2019	364
PB10N-BCZD ^d									
Ni-BCZYYb	BCZYYb (15 μm)	PN	0.99	0.28	0.58	0.86	5.3	2019	365
Ni-BCZYYb	LC BCZYYb (20 μm)	PN	0.95	0.49	1.11	1.60	4.0	2019	365
Ni-BCZYYb	BCZYYb (35 μm)	LNC	1.05	0.72	0.70	1.42	4.8	2019	157
Ni-BCZD	BCZD (25 μm)	PB5N LNF	1.02	0.37	0.25	0.62	6.7	2020	464
Ni-BCZYYC	BCZYYC (13 μm)	LS0.8N-BCZYYC	1.01	0.19	0.36	0.55	6.8	2020	436
Ni-BCZY53	BCZY53 (—)	LCN	1.02	0.18	0.28	0.46	—	220	465
Ni-BCZD	BCZD (30 μm)	PB10N-BCZD	1.03	0.43	0.18	0.61	8.3	2020	466

^a Electrolyte abbreviations: BCY = BaCe_{0.9}Y_{0.1}O_{3-δ}, BCZY = BaCe_{0.7}Zr_{0.1}Y_{0.2}O_{3-δ}, BZY = BaZr_{0.85}Y_{0.15}O_{3-δ}, BCZY44 = BaCe_{0.4}Zr_{0.4}Y_{0.2}O_{3-δ}, BCZY53 = BaCe_{0.5}Zr_{0.3}Y_{0.2}O_{3-δ}, BCZD = BaCe_{0.5}Zr_{0.3}Dy_{0.2}O_{3-δ}, BCZY15 = BaCe_{0.55}Zr_{0.3}Y_{0.15}O_{3-δ}, BCZY62 = BaCe_{0.6}Zr_{0.2}Y_{0.2}O_{3-δ}, BCGC = BaCe_{0.89}Gd_{0.1}Cu_{0.01}O_{3-δ}, BCZYYb = BaCe_{0.7}Zr_{0.1}Y_{0.2}Yb_{0.1}O_{3-δ}, LC = La₂Ce₂O₇, and BCZYYC = BaCe_{0.68}Zr_{0.1}Y_{0.1}Yb_{0.1}Cu_{0.02}O_{3-δ}. ^b Electrode abbreviations: PN = Pr₂NiO_{4+δ}, NN = Nd₂NiO_{4+δ}, LN = La₂NiO_{4+δ}, LCN = La_{1.9}Ca_{0.1}NiO_{4+δ}, LNF = LaNi_{0.6}Fe_{0.4}O_{3-δ}, PLNCN = (Pr_{0.9}La_{0.1})₂Ni_{0.74}Cu_{0.23}Nb_{0.05}O_{4+δ}, NBN = Nd_{1.95}Ba_{0.05}NiO_{4+δ}, PS0.8N = Pr_{1.2}Sr_{0.8}NiO_{4+δ}, LS0.8N = La_{1.2}Sr_{0.8}NiO_{4+δ}, PCN = Pr_{1.7}Ca_{0.3}NiO_{4+δ}, LSNF = La_{1.2}Sr_{0.8}Ni_{0.6}Fe_{0.4}O_{4+δ}, PB10N = Pr_{1.9}Ba_{0.1}NiO_{4+δ}, LNC = La₂Ni_{0.8}Cu_{0.2}O_{4+δ}, LCN = La_{1.9}Ca_{0.1}NiO_{4+δ}, and PB5N = Pr_{1.85}Ba_{0.05}NiO_{4+δ}. ^c Functional electrode (PCN-BCGC) is used together with the LNF collector layer. ^d Functional fuel electrode (reduced PB10N-BCZD) is used together with the supported fuel electrode layer (Ni-BCZD).

regimes of PCFCs or PCECs, only one electrode side operates under oxidising conditions, while the other is fed by reducing gases. Therefore, the performance of $\text{Ln}_2\text{NiO}_{4+\delta}$ -based electrodes also needs to be considered under real conditions.

6. Applied peculiarities of $\text{Ln}_2\text{NiO}_{4+\delta}$ -based electrodes in proton-conducting electrochemical cells

This section highlights the features of applying Ln_2NiO_4 -based electrodes in PCFCs or PCECs. Firstly, open-circuit voltage (OCV) conditions will be considered, and then the performance of the electrodes will be evaluated under electrochemical cell operating conditions.

6.1. OCV conditions

The OCV conditions of any electrochemical cell represent important information since they allow conclusions to be formulated regarding cell integrity and electrolyte electron conductivity. Although OCV measurements ($U_{\text{OC}} = \sim 1 \text{ V}$) are far from the conditions corresponding to the maximum power density ($\sim 0.5 \text{ V}$) or thermoneutral voltage ($\sim 1.3 \text{ V}$), the

electrochemical characterisation of PCFCs/PCECs is almost always performed at OCV. In detail, the impedance spectra are measured at OCV applying a low acceleration voltage (20–50 mV). The spectra obtained in this way provide the corresponding information on ohmic resistance (R_{O}) and polarisation resistance of the electrodes (R_{p}).

Considering R_{O} , the quality of the electrolytes used (in terms of composition and fabrication technique) can be estimated as follows:

$$\sigma = \frac{h}{R_{\text{O}}} \quad (25)$$

where h is the thickness of the electrolyte. It is clear that lower ohmic loss can be achieved by developing thin electrolytes. However, the conductivity of the $\text{Ba}(\text{Ce,Zr})\text{O}_3$ -based electrolytes is not higher than 10 mS cm^{-1} at $600 \text{ }^\circ\text{C}$ (Table 9). Therefore, performance improvement is also limited in terms of developing new compositions fabricated at an optimal thickness (10–30 μm).

Considering R_{p} , the main strategies for improving the electrode performance were described in Section 5.4. As shown in Table 9, the polarisation resistances of Ln_2NiO_4 -based electrodes are quite low, mostly reaching values below $1 \Omega \text{ cm}^2$ at

Table 10 Design and performance of PCFCs with nickelate-based cathodes. Visualisation of the data is presented in Fig. S5, ESI

Fabrication details	Anode	Electrolyte ^a (thickness)	Cathode ^b	P_{max} , mW cm^{-2}			Year	Ref.
				500 $^\circ\text{C}$	600 $^\circ\text{C}$	700 $^\circ\text{C}$		
Co-pressing/screen-printing	Ni-BCY	BCY (40 μm)	PN	—	96	—	2010	252
Tape-casting/screen-printing	Ni-BCY	BCY (27 μm)	NN	—	60	—	2013	460
Co-pressing/screen-printing	Ni-BCY	BCY (50 μm)	PN	—	184	—	2014	461
Co-pressing/painting	Ni-BCZY	BCZY (20 μm)	LN	—	196	398	2014	430
Co-pressing/painting	Ni-BCZY	BCZY (20 μm)	70% LN-30% LNF	—	298	590	2014	430
Co-pressing/painting	Ni-BCZY	BCZY (20 μm)	50% LN-50% LNF	—	273	532	2014	430
Co-pressing/painting	Ni-BCZY	BCZY (20 μm)	30% LN-70% LNF	—	264	486	2014	430
Co-pressing/painting	Ni-BCZY	BCZY (24 μm)	50% LN-50% LNF	—	266	490	2015	431
Co-pressing/spin coating	Ni-BZY	BCZY44 (5 μm)	PN	—	102	234	2015	462
Tape-calendering/painting	Ni-BCZD	BCZD (30 μm)	LN	—	130	215	2016	467
Co-pressing/screen-printing	Ni-BCZY	BCZY (12 μm)	PLNCN	—	420	770	2017	360
Co-pressing/screen-printing	Ni-BCZY	BCZY (15 μm)	PS0.8N	—	127	352	2018	435
Co-pressing/screen-printing	Ni-BCZY	BCZY (15 μm)	LS0.8N	—	223	461	2018	435
Co-pressing/screen-printing	Ni-BCZY15	BCZY15 (5 μm)	PN	240	560	—	2018	362
Co-pressing/painting	Ni-BCZY	BCZY (20 μm)	LN	—	210	461	2018	459
Co-pressing/painting	Ni-BCZY	BCZY (20 μm)	LN-13 wt% LNF	—	361	623	2018	459
Co-pressing/painting	Ni-BCZY	BCZY (20 μm)	LN-23 wt% LNF	—	369	877	2018	459
Co-pressing/painting	Ni-BCZY	BCZY (20 μm)	LN-31 wt% LNF	—	369	969	2018	459
Co-pressing/painting	Ni-BCZY	BCZY (20 μm)	LN-37 wt% LNF	—	302	802	2018	459
Dry-pressing/dip-coating/screen-printing	Ni-BCZY	BCZY (16 μm)	LS0.8N	—	220	460	2018	468
Dry-pressing/dip-coating/screen-printing	Ni-BCZYCY	BCZYCY (13 μm)	LS0.8N	—	250	680	2018	469
Tape-calendering/painting	Ni-BCGC	BCGC (25 μm)	PCN-BCGC LNF ^c	—	61	132	2018	463
Co-pressing/painting	Ni-BCZY	BCZY (15 μm)	LSNF	139	421	782	2019	363
Tape-calendering	Ni-BCZD PB10N -BCZD ^d	BCZD (25 μm)	PB10N-BCZD	—	305	395	2019	364
Tape-calendering/spraying	Ni-BCZYyb	BCZYyb (35 μm)	LNC	—	200	340	2019	157
Co-pressing/screen-printing	Ni-BCZYCY	BCZYCY (13 μm)	LS0.8N-BCZYCY	—	540	1220	2020	436

^a Electrolyte abbreviations: BCY = $\text{BaCe}_{0.9}\text{Y}_{0.1}\text{O}_{3-\delta}$, BCZY = $\text{BaCe}_{0.7}\text{Zr}_{0.1}\text{Y}_{0.2}\text{O}_{3-\delta}$, BZY = $\text{BaZr}_{0.85}\text{Y}_{0.15}\text{O}_{3-\delta}$, BCZY44 = $\text{BaCe}_{0.4}\text{Zr}_{0.4}\text{Y}_{0.2}\text{O}_{3-\delta}$, BCZD = $\text{BaCe}_{0.5}\text{Zr}_{0.3}\text{Dy}_{0.2}\text{O}_{3-\delta}$, BCZY15 = $\text{BaCe}_{0.55}\text{Zr}_{0.3}\text{Y}_{0.15}\text{O}_{3-\delta}$, BCZY62 = $\text{BaCe}_{0.6}\text{Zr}_{0.2}\text{Y}_{0.2}\text{O}_{3-\delta}$, BCGC = $\text{BaCe}_{0.89}\text{Gd}_{0.1}\text{Cu}_{0.01}\text{O}_{3-\delta}$, BCZYyb = $\text{BaCe}_{0.7}\text{Zr}_{0.1}\text{Y}_{0.2}\text{Yb}_{0.1}\text{O}_{3-\delta}$, LC = $\text{La}_2\text{Ce}_2\text{O}_7$, and BCZYCY = $\text{BaCe}_{0.68}\text{Zr}_{0.1}\text{Y}_{0.1}\text{Yb}_{0.1}\text{Cu}_{0.02}\text{O}_{3-\delta}$. ^b Electrode abbreviations: PN = $\text{Pr}_2\text{NiO}_{4+\delta}$, NN = $\text{Nd}_2\text{NiO}_{4+\delta}$, LN = $\text{La}_2\text{NiO}_{4+\delta}$, LNF = $\text{LaNi}_{0.6}\text{Fe}_{0.4}\text{O}_{3-\delta}$, PLNCN = $(\text{Pr}_{0.9}\text{La}_{0.1})_2\text{Ni}_{0.74}\text{Cu}_{0.21}\text{Nb}_{0.05}\text{O}_{4+\delta}$, NBN = $\text{Nd}_{1.95}\text{Ba}_{0.05}\text{NiO}_{4+\delta}$, PS0.8N = $\text{Pr}_{1.2}\text{Sr}_{0.8}\text{NiO}_{4+\delta}$, LS0.8N = $\text{La}_{1.2}\text{Sr}_{0.8}\text{NiO}_{4+\delta}$, PCN = $\text{Pr}_{1.7}\text{Ca}_{0.3}\text{NiO}_{4+\delta}$, LSNF = $\text{La}_{1.2}\text{Sr}_{0.8}\text{Ni}_{0.6}\text{Fe}_{0.4}\text{O}_{4+\delta}$, PB10N = $\text{Pr}_{1.9}\text{Ba}_{0.1}\text{NiO}_{4+\delta}$, LNC = $\text{La}_2\text{Ni}_{0.8}\text{Cu}_{0.2}\text{O}_{4+\delta}$, and PB5N = $\text{Pr}_{1.85}\text{Ba}_{0.05}\text{NiO}_{4+\delta}$. ^c Functional cathode (PCN-BCGC) is used together with the LNF collector layer. ^d Functional anode (reduced PB10N-BCZD) is used together with the supported anode layer (Ni-BCZD).

Table 11 Design and performance of PCECs with nickelate-based anodes

Anode ^a	Electrolyte ^b (thickness)	Cathode	U_{OC} , V		$i_{@1.3\text{ V}}$, mA cm ⁻²		Year	Ref.
			600 °C	700 °C	600 °C	700 °C		
LN	BCZD (30 μm)	Ni-BCZD	1.06	1.00	180	300	2016	467
NBN	BCZD (15 μm)	Ni-BCZD	0.97	0.94	155	400	2018	361
PS0.8N	BCZY (15 μm)	Ni-BCZY	1.03	0.97	350	1120	2018	435
LS0.8N	BCZY (15 μm)	Ni-BCZY	1.01	0.98	420	1410	2018	435 and 468
NBN-BCZD35	BCZD35 (50 μm)	Ni-BCZD35	—	0.9	—	542	2018	470
PN	BCZY62 (20 μm)	Ni-BCZY62	0.98	0.93	345	950	2018	232
LS0.8N	BCZYC (13 μm)	Ni-BCZYC	—	1.01	590	1960	2018	469
PB10N-BCZD	BCZD (25 μm)	Ni-BCZD PB10N-BCZD ^c	1.08	1.01	295	535	2019	364
PN	BCZYYb (15 μm)	Ni-BCZYYb	0.99	0.95	620	1643	2019	365
PN	LC BCZYYb (20 μm)	Ni-BCZYYb	0.95	0.90	330	975	2019	365
PB5N LNF ^d	BCZD (25 μm)	Ni-BCZD	1.02	0.94	610	855	2020	464
NBNF	BCZYYb53 (25 μm)	BCZYYb53	0.99	0.93	360	1370	2020	207
LS0.8N-BCZYC	BCZYC (13 μm)	Ni-BCZYC	1.01	0.99	1040	3020	2020	436

^a Anode abbreviations: LN = La₂NiO_{4+δ}, NBN = Nd_{1.95}Ba_{0.05}NiO_{4+δ}, PS0.8N = Pr_{1.2}Sr_{0.8}NiO_{4+δ}, LS0.8N = La_{1.2}Sr_{0.8}NiO_{4+δ}, PN = Pr₂NiO_{4+δ}, PB10N = Pr_{1.9}Ba_{0.1}NiO_{4+δ}, PB5N = Pr_{1.85}Ba_{0.05}NiO_{4+δ}, LNF = LaNi_{0.6}Fe_{0.4}O_{3-δ}, and NBNF = Nd_{1.9}Ba_{0.1}NiO_{4+δ}F_{0.05}. ^b Electrolyte abbreviations: BCZD = BaCe_{0.3}Zr_{0.3}Dy_{0.2}O_{3-δ}, BCZY = BaCe_{0.7}Zr_{0.1}Y_{0.2}O_{3-δ}, BCZD35 = BaCe_{0.3}Zr_{0.5}Dy_{0.2}O_{3-δ}, BCZY62 = BaCe_{0.6}Zr_{0.2}Y_{0.2}O_{3-δ}, BCZYC = BaCe_{0.68}Zr_{0.1}Y_{0.1}Yb_{0.1}Cu_{0.02}O_{3-δ}, BCZYYb = BaCe_{0.7}Zr_{0.1}Y_{0.2}Yb_{0.1}O_{3-δ}, LC = La₂Ce₂O₇, and BCZYYb53 = BaZr_{0.3}Ce_{0.5}Y_{0.1}Yb_{0.1}O_{3-δ}. ^c Functional cathode (reduced PB10N-BCZD) is used together with the supported cathode layer (Ni-BCZD). ^d Functional anode (PCN-BCGC) is used together with the LNF collector layer.

600 °C. The best results were achieved by An *et al.*³⁶² utilising an undoped Pr₂NiO_{4+δ} electrode and Sun *et al.*⁴³⁶ utilising an infiltrated La_{1.2}Sr_{0.8}NiO_{4-δ}-BaCe_{0.68}Zr_{0.1}Y_{0.1}Yb_{0.1}Cu_{0.02}O_{3-δ} electrode. Looking ahead, it can be noted that these cells also exhibit the highest performance in fuel cell (Table 10) and electrolysis cell (Table 11) operation modes. However, these correlations are not always observed since the electrode response may be considerably (and differently) altered with a variation in the bias. A vivid example of this conclusion was shown in the work by Danilov *et al.*,⁴⁷¹ where the impedance data for a protonic ceramic electrochemical cell with a Pr_{1.95}-Ba_{0.05}NiO_{4+δ} (PBN) electrode was collected not only for OCV, but for the fuel cell (FC) and electrolysis cell (EC) regimes. As can be seen, the overall polarisation resistance of the electrodes monotonously decreased with an increase in bias at low measured temperatures, having a maximum OCV at higher temperatures. This peculiarity indicates that the impedance spectroscopy measurements should be performed under real voltage regimes instead of OCV.

6.2. Fuel cell and electrolysis cell operation modes

Tables 10 and 11 list the evolution of existing results on the application of Ln₂NiO₄-based electrodes with proton-conducting electrolytes. According to the data, it can be seen that the intensive activity initiated in 2017 formed the basis for the work published in the following year. Although some research groups have demonstrated superior results for both PCFCs and PCECs, a significant number of works showed that the maximum power densities range between 200 and 400 mW cm⁻² (fuel cell mode) at 600 °C, while the current densities range between 200 and 600 mA cm⁻² (electrolysis mode) at 1.3 V and the same temperature.

Principally, the literature data reports more promising performances, which can be associated with the utilisation of highly conductive electrode materials, such as simple and double cobaltites and their derivatives.⁴⁷²⁻⁴⁷⁶ Considering the current distribution, this indeed promotes the efficient supply or removal of electrons from the TPB regions to an external electrical circuit. However, as was mentioned in Section 5.2, even if excellent results are achieved for the first time, Co-based oxide-based electrodes suffer from thermo-mechanical incompatibility. Consequently, thermo-cycling and the long-term operation of cells featuring these electrodes may be unsuccessful.

The problem of the low conductivity of nickelates (below 100 S cm⁻¹ for a gas-tight body) can be solved using additional current collector layers (for example, (La,Sr)MnO₃, La(Ni,Fe)O₃, Pt), which improve the current distribution characteristics by covering the surface of the origin electrode.

Generally, the achieved average levels are quite promising for the development of intermediate-temperature PCFCs and PCECs in terms of their up-scaling and durability.^{460,461} For example, Dailly and Marrony⁴⁶⁰ showed that a 3.5 × 3.5 cm² PCFC with an Nd₂NiO_{4+δ} cathode exhibits no visible degradation at 600 °C for over 950 h.

7. Conclusion and future perspectives

The materials of the Ln₂NiO_{4+δ}-related class represent a promising alternative to the conventional ABO₃ electrodes in terms of their application in solid oxide electrochemical cells, including protonic ceramic fuel cells (PCFCs) and protonic ceramic electrolysis cells (PCECs). Exhibiting high structural flexibility towards different types of doping, these layered nickelates enable purposeful tailoring of functional properties important

for prospective application, including high phase stability, chemical and mechanical compatibility, and good mixed ionic-electronic conductivity and electrochemical performance.

Numerous experimental results published over the last five years have shown that lanthanide nickelate-based electrodes demonstrate quite good performances, with polarisation resistance values as low as $0.3\text{--}1\ \Omega\ \text{cm}^2$ at $600\ ^\circ\text{C}$ (open circuit voltage regime of PCFCs and PCECs), which can remain stable over long term operation. These results constitute a possible basis for the scalable fabrication of durable PCFCs/PCECs.

However, although this review describes many advantages of layered nickelates in comparison with other possible oxygen electrodes, a number of pending issues still need to be solved/clarified:

(1) Degree of hydration/protonation of $\text{Ln}_2\text{NiO}_{4+\delta}$ -based materials. Revealing the effect of type and concentration of dopant(s) on the concentration of protons. Identification of mechanisms of proton transport in the layered phases. This information is needed for the design of triple-conducting materials having a high active electrode zone towards occurring (oxygen- and hydrogen-involved) electrochemical reactions. In addition, the mechanism studies for proton migration in layered nickelates are interesting and potentially important for proton transportation in oxides. Since oxygen vacancies are usually regarded as the prerequisite for hydration/protonation, the interstitial oxygens in layered nickelates may play a different role in the proton migration procedure in comparison with that in oxygen vacancy-containing oxides. This difference not only leads to a different strategy for designing materials, but also may inspire scientists to have a better understanding of the mechanism for proton migration since the whole landscape has not been revealed to date.

(2) Rational design of microstructural parameters. The provided analysis was carried out considering macroscopic parameters such as polarisation resistance. On the one hand, these parameters depend on internal solid phase properties; on the other hand, the performance is also affected by the electrode structure. Currently, no general information regarding the morphological properties of $\text{Ln}_2\text{NiO}_{4+\delta}$ -based electrodes exists in the literature. Although nano-structuring of electrodes is a widely employed approach for improving the electrode performance, the high calcination temperatures for achieving the desired $\text{Ln}_2\text{NiO}_{4+\delta}$ can be detrimental for the formation and/or maintenance of the nanostructure of the electrode. Thus, the use of advanced preparation techniques to lower the phase formation temperatures and shorten the dwell time can be beneficial for the formation of nanostructured electrodes with improved TPBs. Moreover, advanced electrode development techniques (three-dimensional ordered pore, finger-like, and nanowires-based structures),^{477–480} which deserve further studies, have not been used for $\text{Ln}_2\text{NiO}_{4+\delta}$.

(3) New fabrication approaches to improve the electrochemical activity of $\text{Ln}_2\text{NiO}_{4+\delta}$ -based electrodes, in particular, adaptation of the plasma spraying technique, pulsed laser deposition, and exsolution, or optimisation of the impregnation method.^{481–484}

(4) Further tailoring the functionality of $\text{Ln}_2\text{NiO}_{4+\delta}$ -based materials by introducing new dopants or their combination in appropriate concentrations at the Ln-, Ni- or O-sublattices (see, for example, the latest works^{485–489}). The (co)doping strategy has great potential due to the previously-mentioned flexibility of the RP structures. The design of suitable composite materials also belongs to this direction.^{315,490,491}

(5) Long-term features of $\text{Ln}_2\text{NiO}_{4+\delta}$ -based electrodes. To fabricate low-cost and performance-competitive PCFCs and PCECs, special attention should be devoted to the kinetic-related processes taking place over longer than 1000 h, including particle coarsening, porosity changes and chemical reactivity with CO_2 , high concentrations of H_2O (in the case of electrolysis cells), and electrolyte components. All these factors affect the TPB length and its corresponding catalytic activity.

In summary, layered $\text{Ln}_2\text{NiO}_{4+\delta}$ oxides show potential suitability for application in protonic ceramic electrochemical cells as electrode materials due to their unique features. However, the application of layered $\text{Ln}_2\text{NiO}_{4+\delta}$ oxides has only emerged in recent years and many issues are still not clear, leaving great room for further exploration. The investigation of layered $\text{Ln}_2\text{NiO}_{4+\delta}$ oxides not only provides a solution for achieving high cell performance, which is the primary goal for practical applications, but also leads to an in-depth understanding of the scientific issues for the community, possibly opening a new door for the development of protonic ceramic electrochemical cells.

Conflicts of interest

There are no conflicts to declare.

Acknowledgements

A. Y. gratefully acknowledges financial support from the FCT, Portugal (project CICECO-Aveiro Institute of Materials, UIDB/50011/2020 & UIDP/50011/2020, financed by national funds through the FCT/MCTES and when appropriate co-financed by FEDER under the PT2020 Partnership Agreement). L. B. gratefully acknowledges the support from the National Natural Science Foundation of China (grant no. 51972183) and the Startup Funding for Talents at University of South China. A. T., J. L and D. M. are grateful to the national projects, supported by the Russian Science Foundation [grant no. 16-19-00104] and the Council of the President of the Russian Federation [scholarship no. CII-161.2018.1 and CII-1413.2019.1].

References

- J. Speirs, P. Balcombe, P. Blomerus, M. Stettler, P. Achurra-Gonzalez, M. Woo, D. Ainalis, J. Cooper, A. Sharafian, W. Merida, D. Crow, S. Giarola, N. Shah, N. Brandon and A. Hawkes, *Prog. Energy*, 2020, 2, 012002.
- F. Dawood, M. Anda and G. M. Shafiullah, *Int. J. Hydrogen Energy*, 2020, 45, 3847–3869.

- 3 Z. Abdin, A. Zafaranloo, A. Rafiee, W. Mérida, W. Lipiński and K. R. Khalilpour, *Renewable Sustainable Energy Rev.*, 2020, **120**, 109620.
- 4 A. Martin, M.-F. Agnoletti and E. Brangier, *Int. J. Hydrogen Energy*, 2020, **45**, 11889–11900.
- 5 G. Yang, C. Su, H. Shi, Y. Zhu, Y. Song, W. Zhou and Z. Shao, *Energy Fuels*, 2020, DOI: 10.1021/acs.energyfuels.0c01887.
- 6 V. Venkataraman, M. Pérez-Fortes, L. Wang, Y. S. Hajimolana, C. Boigues-Muñoz, A. Agostini, S. J. McPhail, F. Maréchal, J. V. Herle and P. V. Aravinda, *J. Energy Storage*, 2019, **24**, 100782.
- 7 A. M. Abdalla, S. Hossain, A. T. Azad, P. M. I. Petra, F. Begum, S. G. Eriksson and A. K. Azad, *Renewable Sustainable Energy Rev.*, 2018, **82**, 353–368.
- 8 Y. Meng, J. Gao, Z. Zhao, J. Amoroso, J. Tong and K. S. Brinkman, *J. Mater. Sci.*, 2019, **54**, 9291–9312.
- 9 J. Kim, S. Sengodan, S. Kim, O. Kwon, Y. Bu and G. Kim, *Renewable Sustainable Energy Rev.*, 2019, **109**, 606–618.
- 10 N. L. R. M. Rashid, A. A. Samat, A. A. Jais, M. R. Somalu, A. Muchtar, N. A. Baharuddin, W. N. Roslam and W. Isahak, *Ceram. Int.*, 2019, **45**, 6605–6615.
- 11 W. Wang, D. Medvedev and Z. Shao, *Adv. Funct. Mater.*, 2019, **28**, 1802592.
- 12 D. Medvedev, *Int. J. Hydrogen Energy*, 2020, **44**, 26711–26740.
- 13 S. Hossain, A. M. Abdalla, S. N. Bintijamain, J. H. Zaini and A. K. Azad, *Renewable Sustainable Energy Rev.*, 2017, **79**, 750–764.
- 14 D. A. Medvedev, J. G. Lyagaeva, E. V. Gorbova, A. K. Demin and P. Tsiakaras, *Prog. Mater. Sci.*, 2016, **75**, 38–79.
- 15 C. Duan, R. J. Kee, H. Zhu, C. Karakaya, Y. Chen, S. Ricote, A. Jarry, E. J. Crumlin, D. Hook, R. Braun, N. P. Sullivan and R. O'Hayre, *Nature*, 2018, **557**, 217–222.
- 16 C. Duan, J. Tong, M. Shang, S. Nikodemski, M. Sanders, S. Ricote, A. Almansoori and R. O'Hayre, *Science*, 2015, **349**, 1321–1326.
- 17 S. Choi, C. J. Kucharczyk, Y. Liang, X. Zhang, I. Takeuchi, H.-I. Ji and S. M. Haile, *Nat. Energy*, 2018, **3**, 202–210.
- 18 S. Choi, T. C. Davenport and S. M. Haile, *Energy Environ. Sci.*, 2019, **12**, 206–215.
- 19 K. Bae, D. Y. Jang, H. J. Choi, D. Kim, J. Hong, B.-K. Kim, J.-H. Lee, J.-W. Son and J. H. Shim, *Nat. Commun.*, 2017, **8**, 14553.
- 20 H. An, H.-W. Lee, B.-K. Kim, J.-W. Son, K. J. Yoon, H. Kim, D. Shin, H.-I. Ji and J.-H. Lee, *Nat. Energy*, 2018, **3**, 870–875.
- 21 Y. Wang, W. Li, L. Ma, W. Li and X. Liu, *J. Mater. Sci. Technol.*, 2020, **55**, 35–55.
- 22 M. Reisert, A. Aphale and P. Singh, *Materials*, 2018, **11**, 2169.
- 23 B. Koo, K. Kim, J. K. Kim, H. Kwon, J. W. Han and W. Jung, *Joule*, 2018, **2**, 1476–1499.
- 24 Z. Yang, M. Guo, N. Wang, C. Ma, J. Wang and M. Han, *Int. J. Hydrogen Energy*, 2017, **42**, 24948–24959.
- 25 L. Fan, B. Zhu, P.-C. Su and C. He, *Nano Energy*, 2018, **45**, 148–176.
- 26 W. Zhou, X. Wang, Y. Zhu, J. Dai, Y. Zhu and Z. Shao, *Mater. Rev.*, 2018, **32**, 337–356.
- 27 A. V. Kasyanova, L. R. Tarutina, A. O. Rudenko, J. G. Lyagaeva and D. A. Medvedev, *Russ. Chem. Rev.*, 2020, **89**, 667–692.
- 28 P. Kaur and K. Singh, *Ceram. Int.*, 2020, **46**, 5521–5535.
- 29 S. Afroze, A. Karim, Q. Cheok, S. Eriksson and A. K. Azad, *Front. Energy*, 2019, **13**, 770–797.
- 30 S. S. Hashim, F. Liang, W. Zhou and J. Sunarso, *ChemElectroChem*, 2019, **6**, 3549–3569.
- 31 M. Rafique, H. Nawaz, M. S. Rafique, M. B. Tahir, G. Nabi and N. R. Khalid, *Energy Res.*, 2019, **43**, 2423–2446.
- 32 G. Nirala, D. Yadav and S. Upadhyay, *J. Adv. Ceram.*, 2020, **9**, 129–148.
- 33 D. Lee, Y.-L. Lee, A. Grimaud, W. T. Hong, M. D. Biegalski, D. Morgane and Y. Shao-Horn, *J. Mater. Chem. A*, 2014, **2**, 6480–6487.
- 34 S. Choi, S. Yoo, J.-Y. Shin and G. Kim, *J. Electrochem. Soc.*, 2011, **158**, B995–B999.
- 35 A. R. Gilev, E. A. Kiselev and V. A. Cherepanov, *Solid State Ionics*, 2019, **339**, 115001.
- 36 M. Garali, M. Kahlaoui, B. Mohammed, A. Mater, C. B. Azouz and C. Chefi, *Int. J. Hydrogen Energy*, 2019, **44**, 11020–11032.
- 37 B. Philippeau, F. Mauvy, C. Mazataud, S. Fourcade and J.-C. Grenier, *Solid State Ionics*, 2013, **249–250**, 17–25.
- 38 X. Zhang, L. Zhang, J. Meng, W. Zhang, F. Meng, X. Liu and J. Meng, *Int. J. Hydrogen Energy*, 2017, **42**, 29498–29510.
- 39 V. A. Sadykov, E. M. Sadovskaya, N. F. Eremeev, P. I. Skriabin, A. V. Krasnov, Y. N. Bepalko, S. N. Pavlova, Y. E. Fedorova, E. Y. Pikalova and A. V. Shlyakhtina, *Russ. J. Electrochem.*, 2019, **55**, 701–718.
- 40 S. N. Ruddlesden and P. Popper, *Acta Crystallogr.*, 1958, **11**, 54–55.
- 41 M. Greenblatt, *Curr. Opin. Solid State Mater. Sci.*, 1997, **2**, 174–183.
- 42 A. Demourgues, A. Wattiaux, J. C. Grenier, M. Pouchard, J. L. Soubeyroux, J. M. Dance and P. Hagenmuller, *J. Solid State Chem.*, 1993, **105**, 458–470.
- 43 A. Aguadero, J. A. Alonso, M. J. Martínez-Lope, M. T. Fernández-Díaz, M. J. Escudero and L. Daza, *J. Mater. Chem.*, 2006, **16**, 3402–3408.
- 44 J. F. Ackerman, *Mater. Res. Bull.*, 1979, **14**, 487–491.
- 45 K. K. Singh, P. Ganguly and J. B. Goodenough, *J. Solid State Chem.*, 1984, **52**, 254–273.
- 46 P. Ganguly and C. N. R. Rao, *J. Solid State Chem.*, 1984, **53**, 193–216.
- 47 C. Frayret, A. Villesuzanne and M. Pouchard, *Chem. Mater.*, 2005, **17**, 6538–6544.
- 48 R. D. Shannon, *Acta Crystallogr., Sect. A: Found. Crystallogr.*, 1996, **A32**, 751–767.
- 49 M. T. Fernández-Díaz, J. L. Martínez and J. Rodríguez-Carvajal, *Solid State Ionics*, 1993, **63–65**, 902–906.
- 50 C. Allançon, J. Rodríguez-Carvajal, M. T. Fernández-Díaz, P. Odier, J. M. Bassat, J. P. Loup and J. L. Martínez, *Z. Phys. B: Condens. Matter*, 1996, **100**, 85–90.
- 51 J. M. Bassat, P. Odier and J. P. Loup, *J. Solid State Chem.*, 1994, **110**, 124–135.

- 52 A. V. Kovalevsky, V. V. Kharton, A. A. Yaremchenko, Y. V. Pivak, E. V. Tsipis, S. O. Yakovlev, A. A. Markov, E. N. Naumovich and J. R. Frade, *J. Electroceram.*, 2007, **18**, 205–218.
- 53 E. Boehm, J.-M. Bassat, P. Dordor, F. Mauvy, J.-C. Grenier and P. Stevens, *Solid State Ionics*, 2005, **176**, 2717–2725.
- 54 C. Allançon, A. Gonthier-Vassal, J. M. Bascat, J. P. Loup and P. Odier, *Solid State Ionics*, 1994, **74**, 239–248.
- 55 H. Tamura, A. Hayashi and Y. Ueda, *Solid State Ionics*, 1996, **258**, 61–71.
- 56 T. Nakamura, K. Yashiro, K. Sato and J. Mizusaki, *Solid State Ionics*, 2009, **180**, 368–376.
- 57 V. Vashook, E. Girdauskaite, J. Zosel, T.-L. Wen, H. Ullmann and U. Guth, *Solid State Ionics*, 2006, **177**, 1163–1171.
- 58 T. Nakamura, K. Yashiro, K. Sato and J. Mizusaki, *J. Solid State Chem.*, 2009, **182**, 1533–1537.
- 59 T. Nakamura, K. Yashiro, K. Sato and J. Mizusaki, *Solid State Ionics*, 2009, **180**, 1406–1413.
- 60 V. V. Kharton, E. V. Tsipis, E. N. Naumovich, A. Thursfield, M. V. Patrakeev, V. A. Kolotygin, J. C. Waerenborgh and I. S. Metcalfe, *J. Solid State Chem.*, 2008, **181**, 1425–1433.
- 61 E. N. Naumovich, M. V. Patrakeev, V. V. Kharton, A. A. Yaremchenko, D. I. Logvinovich and F. M. B. Marques, *Solid State Sci.*, 2005, **7**, 1353–1362.
- 62 E. N. Naumovich, M. V. Patrakeev, V. V. Kharton, A. A. Yaremchenko, E. V. Tsipis, J. R. Frade, D. I. Logvinovich and F. M. B. Marques, *Mater. Sci. Forum*, 2006, **514–516**, 397–401.
- 63 H.-S. Kim and H. Yoo, *Phys. Chem. Chem. Phys.*, 2010, **12**, 4704–4713.
- 64 S.-Y. Jeon, M.-B. Choi, J.-H. Hwang, E. D. Wachsman and S.-J. Song, *J. Solid State Electrochem.*, 2012, **16**, 785–793.
- 65 Y. Naumovich, *Quantitative description of oxygen non-stoichiometry in mixed ionic and electronic conductors based on a non-ideal solution approach*, Institute of Power Engineering, Warsaw, 2019.
- 66 H. Tamura, A. Hayashi and Y. Ueda, *Phys. C*, 1993, **216**, 83–88.
- 67 S. J. Skinner, *Solid State Sci.*, 2003, **5**, 419–426.
- 68 J. D. Jorgensen, B. Dabrowski, S. Pei, D. R. Richards and D. G. Hinks, *Phys. Rev. B: Condens. Matter Mater. Phys.*, 1989, **40**, 2187.
- 69 T. Broux, C. Prestipino, M. Bahout, S. Paofai, E. Elkaïm, V. Vibhu, J.-C. Grenier, A. Rougier, J.-M. Bassat and O. Hernandez, *Dalton Trans.*, 2016, **45**, 3024–3033.
- 70 V. Vibhu, M. R. Suchomel, N. Penin, F. Weill, J.-C. Grenier, J.-M. Bassat and A. Rougier, *Dalton Trans.*, 2019, **48**, 266–277.
- 71 S. M. Aspera, M. Sakaue, T. D. K. Wungu, M. Alaydrus, T. P. T. Linh, H. Kasai, M. Nakanishi and T. Ishihara, *J. Phys.: Condens. Matter*, 2012, **24**, 405504.
- 72 A. Flura, S. Dru, C. Nicollet, V. Vibhu, S. Fourcade, E. Lebraud, A. Rougier, J.-M. Bassat and J.-C. Grenier, *J. Solid State Chem.*, 2015, **228**, 189–198.
- 73 R. K. Sharma, S.-K. Cheah, M. Burriel, L. Dessemond, J.-M. Bassat and E. Djurado, *J. Mater. Chem. A*, 2017, **5**, 1120–1132.
- 74 A. Montenegro-Hernández, J. Vega-Castillo, A. Caneiro and L. Moggi, *J. Solid State Chem.*, 2019, **276**, 210–216.
- 75 D. Ning, A. Baki, T. Scherb, J. Song, A. Fantin, X. Liu, G. Schumacher, J. Banhart and H. J. M. Bouwmeester, *Solid State Ionics*, 2019, **342**, 115056.
- 76 Y. Toyosumi, H. Ishikawa and K. Ishikawa, *J. Alloys Compd.*, 2006, **408–412**, 1200–1204.
- 77 M. Zaghrioui, F. Giovannelli, N. P. D. Brouri and I. Laffez, *J. Solid State Chem.*, 2004, **177**, 3351–3358.
- 78 S. M. Pikalov, L. B. Vedmid, E. A. Filonov, E. Y. Pikalova, J. G. Lyagaeva, N. A. Danilov and A. A. Murashkina, *J. Alloys Compd.*, 2019, **801**, 558–567.
- 79 Y. Takeda, M. Nishijima, N. Imanishi, R. Kanno, O. Yamamoto and M. Takano, *J. Solid State Chem.*, 1992, **96**, 72–83.
- 80 T. Ogier, C. Prestipino, S. Figueroa, F. Mauvy, J. Mougín, J. C. Grenier, A. Demourgues and J. M. Bassat, *Chem. Phys. Lett.*, 2019, **727**, 116–120.
- 81 J. Dailly, S. Fourcade, A. Largeteau, F. Mauvy, J. C. Grenier and M. Marrony, *Electrochim. Acta*, 2010, **55**, 5847–5853.
- 82 E. Y. Pikalova, A. A. Kolchugin, V. A. Sadykov, E. M. Sadvskaya, E. A. Filonova, N. F. Ereemeev and N. M. Bogdanovich, *Int. J. Hydrogen Energy*, 2018, **43**, 17373–17386.
- 83 C. Allançon, P. Odier, J. M. Bassat and J. P. Loup, *J. Solid State Chem.*, 1997, **131**, 167–172.
- 84 A. D. Rougier, A. Flura, C. Nicollet, V. Vibhu, S. Fourcade, E. Lebraud, J.-M. Bassat and J.-C. Grenier, *ECS Trans.*, 2015, **68**, 817–823.
- 85 H. Zhao, F. Mauvy, C. Lalanne, J.-M. Bassat, S. Fourcade and J.-C. Grenier, *Solid State Ionics*, 2008, **179**, 2000–2005.
- 86 A. Egger, E. Bucher, W. Sitte, C. Lalanne and J.-M. Bassat, *ECS Trans.*, 2009, **25**, 2547–2556.
- 87 B. Gedziorowski, K. Cichy, A. Niemczyk, A. Olszewska, Z. Zhang, S. Kopec, K. Zheng, M. Marzec, M. Gajewska, Z. Du, H. Zhao and K. Swierczek, *J. Eur. Ceram. Soc.*, 2020, **40**, 4056–4066.
- 88 E. Niwa, T. Nakamura, J. Mizusaki and T. Hashimoto, *Thermochim. Acta*, 2011, **523**, 46–50.
- 89 H. Ishikawa, Y. Toyosumi and K. Ishikawa, *J. Alloys Compd.*, 2006, **406–412**, 1196–1199.
- 90 E. Niwa, K. Wakai, T. Hori, K. Yashiro, J. Mizusaki and T. Hashimoto, *Thermochim. Acta*, 2014, **575**, 129–134.
- 91 T. Nakamura, K. Yashiro, K. Sato and J. Mizusaki, *Solid State Ionics*, 2010, **181**, 402–411.
- 92 V. Sadykov, Y. Okhlupin, N. Yermeev, Z. Vinokurov, A. Shmakov, V. Belyaev, N. Uvarov and J. Mertens, *Solid State Ionics*, 2014, **262**, 918–922.
- 93 V. Vibhu, A. Rougier, C. Nicollet, A. Flura, J.-C. Grenier and J.-M. Bassat, *Solid State Ionics*, 2015, **278**, 32–37.
- 94 A. Murata, C. Hai and M. Matsuda, *Mater. Lett.*, 2014, **136**, 292–294.
- 95 M. Sakai, C. Wang, T. Okiba, H. Soga and T. Hashimoto, *J. Therm. Anal. Calorim.*, 2020, **142**, 139–147.
- 96 E. Dogdibegovic, Q. Cai, N. S. Alabri, W. Guan and X.-D. Zhou, *J. Electrochem. Soc.*, 2016, **164**, F99–F106.

- 97 G. Amow and S. J. Skinner, *J. Solid State Electrochem.*, 2006, **10**, 538–546.
- 98 J. P. Tang, R. I. Dass and A. Manthiram, *Mater. Res. Bull.*, 2000, **35**, 411–424.
- 99 K. Ruck, G. Krabbes and I. Vogel, *Mater. Res. Bull.*, 1999, **34**, 1689–1697.
- 100 Y. Shen, H. Zhao, X. Liua and N. Xu, *Phys. Chem. Chem. Phys.*, 2010, **12**, 15124–15131.
- 101 E. Y. Pikalova, D. A. Medvedev and A. F. Khasanov, *Phys. Solid State*, 2010, **59**, 694–702.
- 102 V. A. Sadykov, E. Y. Pikalova, A. A. Kolchugin, E. A. Filonova, E. M. Sadvovskaya, N. F. Ereemeev, A. V. Ishchenko, A. V. Fetisov and S. M. Pikalov, *Solid State Ionics*, 2018, **317**, 234–243.
- 103 S. W. Li and Y. F. Ren, *Mater. Res. Bull.*, 1995, **30**, 1505–1511.
- 104 M. James and J. P. Attfield, *J. Mater. Chem.*, 1996, **6**, 57–62.
- 105 Y. Takeda, R. Kanno, M. Sakano and O. Yamamoto, *Mater. Res. Bull.*, 1990, **25**, 293–306.
- 106 E. S. Kravchenko, K. V. Zakharchuk, V. V. Pankov and A. A. Yaremchenko, *J. Belarus. State Univ. Chem.*, 2017, **1**, 43–49.
- 107 A. Yaremchenko, E. Kravchenko, K. Zakharchuk, J. Grins, G. Svensson and V. Pankov, Oxygen-deficient Ruddlesden–Popper $\text{Pr}_{1-x}\text{Sr}_{1+x}\text{NiO}_{4-\delta}$ as prospective oxygen electrode materials for SOFC/SOEC, *21st International Conference on Solid State Ionics (SSI-21)*, Padua, Italy, 18–23 June 2017, Program Guide and Abstracts, abstract I-12_26/O, p. 365.
- 108 E. Kravchenko, D. Khalyavin, K. Zakharchuk, J. Grins, G. Svensson, V. Pankov and A. Yaremchenko, *J. Mater. Chem. A*, 2015, **3**, 23852–23863.
- 109 A. B. Austin, L. G. Carreiro and J. V. Marzik, *Mater. Res. Bull.*, 1989, **24**, 639–646.
- 110 Y. K. Chung, Y.-U. Kwon and S. H. Byeon, *Bull. Korean Chem. Soc.*, 1995, **16**, 120–125.
- 111 H. Soga, C. Wang, T. Hayashi, T. Morise, E. Niwa and T. Hashimoto, *ECS Trans.*, 2017, **78**, 613–622.
- 112 K. K. Singh, P. Ganguly and C. N. R. Rao, *Mater. Res. Bull.*, 1982, **17**, 493–500.
- 113 E. Boehm, J.-M. Bassat, M. C. Steil, P. Dordor, F. Mauvy and J.-C. Grenier, *Solid State Sci.*, 2003, **5**, 973–981.
- 114 A. Aguadero, J. A. Alonso, M. J. Escudero and L. Daza, *Solid State Ionics*, 2008, **179**, 393–400.
- 115 M. Sakai, C. Wang, T. Okiba, H. Soga, E. Niwa and T. Hashimoto, *J. Therm. Anal. Calorim.*, 2019, **135**, 2765–2774.
- 116 C. Wang, H. Soga, T. Okiba, E. Niwa and T. Hashimoto, *Mater. Res. Bull.*, 2019, **111**, 61–69.
- 117 G. Amow, P. S. Whitfield, I. J. Davidson, R. P. Hammond, C. N. Munnings and S. J. Skinner, *Ceram. Int.*, 2004, **30**, 1635–1639.
- 118 C. Berger, E. Bucher, A. Egger, A. T. Strasser, N. Schrödl, C. Gspan, J. Hofer and W. Sitte, *Solid State Ionics*, 2018, **316**, 93–101.
- 119 S. Li, H. Tu, F. Li, M. T. Anwar and L. Yu, *J. Alloys Compd.*, 2017, **694**, 17–23.
- 120 T. Nakamura, Y. Ling and K. Amezawa, *J. Mater. Chem. A*, 2015, **3**, 10471–10479.
- 121 E. V. Tsipis, E. N. Naumovich, M. V. Patrakeev, J. C. Waerenborgh, Y. V. Pivak, P. Gaczyński and V. V. Kharton, *J. Phys. Chem. Solids*, 2007, **68**, 1443–1455.
- 122 M.-L. Fontaine, C. Laberty-Robert, A. Barnabé, F. Ansart and P. Tailhades, *Ceram. Int.*, 2004, **30**, 2087–2098.
- 123 A. K. Ganguli, R. Nagarajan, G. R. Rao, N. Y. Vasanthacharya and C. N. R. Rao, *Solid State Commun.*, 1989, **72**, 195–197.
- 124 R. Benloucif, N. Nguyen, J. M. Greneche and B. Raveau, *J. Phys. Chem. Solids*, 1989, **50**, 435–440.
- 125 C. Lalanne, G. Prospero, J.-M. Bassat, F. Mauvy, S. Fourcade, P. Stevens, M. Zahid, S. Diethelm, J. Van herle and J.-C. Grenier, *J. Power Sources*, 2008, **185**, 1218–1224.
- 126 F. Mauvy, C. Lalanne, J.-M. Bassat, J.-C. Grenier, A. Brisse, A.-L. Sauvet, C. Barthet and J. Fouletier, *Solid State Ionics*, 2009, **180**, 1183–1189.
- 127 Y. Chen, B. Qian, G. Yang, D. Chen and Z. Shao, *J. Mater. Chem. A*, 2015, **3**, 6501–6508.
- 128 M. Ferkhi and H. A. Yahia, *Mater. Res. Bull.*, 2016, **83**, 268–274.
- 129 A. Usenka, V. Pankov, V. Vibhu, A. Flura, J.-C. Grenier and J.-M. Bassat, *ECS Trans.*, 2019, **91**, 1341–1353.
- 130 A. A. Kolchugin, E. Y. Pikalova, N. M. Bogdanovich, D. I. Bronin, S. M. Pikalov, S. V. Plaksin, M. V. Ananyev and V. A. Eremin, *Solid State Ionics*, 2016, **288**, 48–53.
- 131 A. R. Gilev, E. A. Kiselev, D. M. Zakharov and V. A. Cherepanov, *J. Alloys Compd.*, 2018, **753**, 491–501.
- 132 E. Pikalova, A. Kolchugin, E. Filonova, N. Bogdanovich, S. Pikalov, M. Ananyev, N. Molchanova and A. Farlenkov, *Solid State Ionics*, 2018, **319**, 130–140.
- 133 M. Khairy, P. Odier and J. Choisnet, *J. Phys., Colloq.*, 1986, **47**, C1-831–C1-835.
- 134 I. Gopalakrishnan, G. Colsmann and B. Reuter, *J. Solid State Chem.*, 1977, **22**, 145–149.
- 135 T. Nitadori, M. Muramatsu and M. Misono, *Bull. Chem. Soc. Jpn.*, 1988, **61**, 3831–3837.
- 136 K. Sreedhar and C. N. R. Rao, *Mater. Res. Bull.*, 1990, **25**, 1235–1242.
- 137 X. Granados, J. Fontcuberta, M. Vallet-Regi, M. J. Sayague and J. M. Gonza-Calbet, *J. Solid State Chem.*, 1993, **102**, 455–464.
- 138 L. V. Makhnach, V. V. Pankov and P. Strobel, *Mater. Chem. Phys.*, 2008, **111**, 125–130.
- 139 V. V. Vashook, S. P. Tolochko, I. I. Yushkevich, L. V. Makhnach, I. F. Kononyuk, H. Altenburg, J. Hauck and H. Ullmann, *Solid State Ionics*, 1998, **110**, 245–253.
- 140 V. V. Vashook, I. I. Yushkevich, L. V. Kokhanovsky, L. V. Makhnach, S. P. Tolochko, I. F. Kononyuk, H. Ullmann and H. Altenburg, *Solid State Ionics*, 1999, **119**, 23–30.
- 141 A. Aguadero, M. J. Escudero, M. Perez, J. A. Alonso, V. Pomjakushin and L. Daza, *Dalton Trans.*, 2006, 4377–4383.
- 142 T. Nakamura, K. Yashiro, K. Sato and J. Mizusaki, *Phys. Chem. Chem. Phys.*, 2009, **11**, 3055–3062.

- 143 S. C. Chen, K. V. Ramanujachary and M. Greenblatt, *J. Solid State Chem.*, 1993, **105**, 444–457.
- 144 A. Grimaud, F. Mauvy, J. M. Bassat, S. Fourcade, M. Marrony and J. C. Grenier, *J. Mater. Chem.*, 2012, **22**, 16017–16025.
- 145 E. Kravchenko, K. Zakharchuk, A. Viskup, J. Grins, G. Svensson, V. Pankov and A. Yaremchenko, *ChemSusChem*, 2017, **10**, 600–611.
- 146 S. M. Doyle, M. P. S. Kumar and D. M. Paul, *J. Phys.: Condens. Matter*, 1992, **4**, 3559–3568.
- 147 B. W. Arbuckle, K. V. Ramanujachary, Z. Zhang and M. Greenblatt, *J. Solid State Chem.*, 1990, **88**, 278–290.
- 148 T. Nakamura, K. Yashiro, K. Sato and J. Mizusaki, *Mater. Chem. Phys.*, 2010, **122**, 250–258.
- 149 J. Alonso, M. Vallet-Regi and J. M. Gonzalez-Calbet, *Solid State Ionics*, 1993, **66**, 219–223.
- 150 M. Hücker, K. Chung, M. Chand, T. Vogt, J. M. Tranquada and D. J. Buttrey, *Phys. Rev. B: Condens. Matter Mater. Phys.*, 2004, **70**, 064105.
- 151 M. Jimenez-Ruiz, C. Prieto, J. L. Martinez and J. M. Alonso, *J. Solid State Chem.*, 1998, **140**, 278–284.
- 152 C. J. Liu, M. D. Mays, D. O. Cowan and M. G. Sanchez, *Chem. Mater.*, 1991, **3**, 495–500.
- 153 H.-S. Kim and H.-I. Yoo, *Solid State Ionics*, 2013, **232**, 129–137.
- 154 Z. Li, R. Haugrud, J. B. Smith and T. Norby, *Solid State Ionics*, 2009, **180**, 1433–1441.
- 155 E. Kravchenko, A. Neagu, K. Zakharchuk, J. Grins, G. Svensson, V. Pankov and A. A. Yaremchenko, *Eur. J. Inorg. Chem.*, 2018, 3320–3329.
- 156 A. Aguadero, M. Perez, J. A. Alonso and L. Daza, *J. Power Sources*, 2005, **151**, 52–56.
- 157 A. P. Tarutin, J. G. Lyagaeva, A. S. Farlenkov, A. I. Vylkov and D. M. Medvedev, *Ceram. Int.*, 2019, **45**, 16105–16112.
- 158 K. Zheng and K. Swierczek, *Mater. Res. Bull.*, 2016, **84**, 259–266.
- 159 Y. Wang, J. Cheng, Q. Jiang, J. Yang and J. Gao, *J. Power Sources*, 2011, **196**, 3104–3108.
- 160 J. A. Kilner and C. K. M. Shaw, *Solid State Ionics*, 2002, **154–155**, 523–527.
- 161 E. V. Tsipis, E. N. Naumovich, A. L. Shaula, M. V. Patrakee, J. C. Waerenborgh and V. V. Kharton, *Solid State Ionics*, 2008, **179**, 57–60.
- 162 S. Miyoshi, T. Furuno, O. Sangoanruang, H. Matsumoto and T. Ishihara, *J. Electrochem. Soc.*, 2007, **154**, B57–B62.
- 163 T. Klande, K. Efimov, S. Cusenza, K.-D. Becker and A. Feldhoff, *J. Solid State Chem.*, 2011, **184**, 3310–3318.
- 164 S. Crapanzano, I. V. Babich and L. Lefferts, *Appl. Catal., A*, 2010, **378**, 144–150.
- 165 S. Y. Gómez, J. Gorauskis, V. Øygarden, D. Hotza, T. Grande and K. Wiik, *Solid State Ionics*, 2016, **292**, 38–44.
- 166 J. Zhu, D. Xiao, J. Li and X. Yang, *Catal. Lett.*, 2009, **129**, 240–246.
- 167 H. El Shinawi and C. Greaves, *J. Mater. Chem.*, 2010, **20**, 504–511.
- 168 S. Yi, Y. Shen, H. Zhao, Z. Du, N. Chen and B. Huang, *Electrochim. Acta*, 2016, **219**, 394–400.
- 169 W. Li, B. Guan, J. Yan, N. Zhang, X. Zhang and X. Liu, *J. Power Sources*, 2016, **318**, 178–183.
- 170 L. Y. Gavrilova, T. V. Aksenova, L. A. Bannykh, Y. V. Teslenko and V. A. Cherepanov, *J. Struct. Chem.*, 2003, **44**, 248–251.
- 171 A. R. Gilev, E. A. Kiselev and V. A. Cherepanov, *Solid State Ionics*, 2015, **279**, 53–59.
- 172 A. R. Gilev, E. A. Kiselev and V. A. Cherepanov, *RSC Adv.*, 2016, **6**, 72905–72917.
- 173 R. Benloucif, N. Nguyen, J. M. Greneche and B. Raveau, *J. Phys. Chem. Solids*, 1991, **52**, 381–387.
- 174 R. P. Forslund, W. G. Hardin, X. Rong, A. M. Abakumov, D. Filimonov, C. T. Alexander, J. T. Mefford, H. Iyer, A. M. Kolpak, K. P. Johnston and K. J. Stevenson, *Nat. Commun.*, 2018, **9**, 3150.
- 175 H. Chaker, T. Roisnel, M. Potel and R. B. Hassen, *J. Solid State Chem.*, 2004, **177**, 4067–4072.
- 176 H. Chaker, I. Raies, A. Chouket, T. Roisnel and R. B. Hassen, *Ionics*, 2017, **23**, 2229–2240.
- 177 S. Y. Istomin, O. M. Karakulina, M. G. Rozova, S. M. Kazakov, A. A. Gippius, E. V. Antipov, I. A. Bobrikov, A. M. Balagurov, A. A. Tsirlin, A. Michau, J. J. Biendicho and G. Svensson, *RSC Adv.*, 2016, **6**, 33951–33958.
- 178 A. Chouket, O. Bidault, L. Combemale, O. Heintz, M. Khitouni and V. Optasanu, *J. Alloys Compd.*, 2018, **732**, 149–159.
- 179 J. E. Millburn and M. J. Rosseinsky, *Chem. Mater.*, 1997, **9**, 511–522.
- 180 F. Tonus, M. Bahout, P. D. Battle, T. Hansen, P. F. Henry and T. Roisnel, *J. Mater. Chem.*, 2010, **20**, 4103–4115.
- 181 M. Jammali, R. B. Hassen and J. Rohlicek, *Powder Diffr.*, 2012, **27**, 184–188.
- 182 H. Chaker, T. Roisnel, M. Ceretti and R. B. Hassen, *Powder Diffr.*, 2010, **25**, 241–246.
- 183 M. Jammali, H. Chaker, K. Cherif and R. B. Hassen, *J. Mater. Chem.*, 2010, **183**, 1194–1199.
- 184 S. E. Dutton, M. Bahout, P. D. Battle, F. Tonus and V. Demange, *J. Solid State Chem.*, 2008, **181**, 2217–2226.
- 185 T. Ishihara, S. Miyoshi, T. Furuno, O. Sangoanruang and H. Matsumoto, *Solid State Ionics*, 2006, **177**, 3087–3091.
- 186 N. Ye and J. L. Hertz, *Acta Mater.*, 2014, **63**, 123–129.
- 187 K. Meeporn, N. Chanlek and P. Thongbai, *RSC Adv.*, 2016, **6**, 91377–91385.
- 188 C. A. Silva, J. B. Silva, M. C. Silva-Santana, P. B. Silva and N. O. Moreno, *Adv. Mater. Res.*, 2014, **975**, 75–80.
- 189 S. -Y. Jeon, B. Singh, Y. -S. Yoo, J. -H. Hwang and S. -J. Song, *J. Am. Ceram. Soc.*, 2014, **97**, 1489–1496.
- 190 S.-Y. Jeon, B. Singh, H.-N. Im, K.-P. Seong and S.-J. Song, *J. Alloys Compd.*, 2014, **589**, 572–578.
- 191 D. Reinen, U. Kesper and D. Belder, *J. Solid State Chem.*, 1995, **116**, 355–363.
- 192 V. F. Savchenko, L. V. Makhnach, I. I. Emelyanova and V. V. Pankov, *Inorg. Mater.*, 2006, **42**, 788–793.
- 193 Z. Zhang, Z. Du, A. Niemczyk, K. Li, H. Zhao and K. Swierczek, *Solid State Ionics*, 2018, **317**, 26–31.
- 194 A. Kawahara and T. Ishihara, *Electrochem. Solid-State Lett.*, 2010, **13**, B76–B78.

- 195 T. Ishihara, N. Sirikanda, K. Nakashima, S. Miyoshi and H. Matsumoto, *J. Electrochem. Soc.*, 2010, **157**, B141–B146.
- 196 Q. Zhou, L. Qu, T. Zhang, Y. He, C. Zhao, M. Wang, T. Wei and Y. Zhang, *J. Alloys Compd.*, 2020, **824**, 153967.
- 197 M. Bansod, A. P. Khandale and S. S. Bhoga, *Ionics*, 2017, **23**, 2561–2570.
- 198 T. Ishihara, K. Nakashima, S. Okada, M. Enoki and H. Matsumoto, *Solid State Ionics*, 2008, **179**, 1367–1371.
- 199 J. Mao, S. Peng, C. Zhang, S. Qi, J. Cui, Y. Gong, S. Wang, C. Wu and Q. Zhou, *J. Alloys Compd.*, 2019, **793**, 519–525.
- 200 Q. Zheng, J. Xue, Q. Liao, Y. Wei, Z. Li and H. Wang, *Chem. Eng. Sci.*, 2013, **101**, 240–247.
- 201 H. W. Nie, T.-L. Wen, S. R. Wang, Y. S. Wang, U. Guth and V. Vashook, *Solid State Ionics*, 2006, **177**, 1929–1932.
- 202 H. Lou, Y. Ge, P. Chen, M. Mei, F. Ma and G. Lü, *J. Mater. Chem.*, 1997, **7**, 2097–2101.
- 203 Q. Li, Y. Fan, H. Zhao, L. P. Sun and L. H. Huo, *J. Power Sources*, 2007, **167**, 64–68.
- 204 V. N. Chaudhari, A. P. Khandale and S. S. Bhoga, *J. Power Sources*, 2014, **248**, 647–654.
- 205 V. Bhat, C. N. R. Rao and J. M. Honig, *Solid State Commun.*, 1992, **81**, 751–756.
- 206 B. W. Arbuckle, K. V. Ramanujachary, A. M. Buckley and M. Greenblatt, *J. Mater. Chem.*, 1992, **97**, 274–282.
- 207 A. P. Tarutin, G. K. Vdovin, D. A. Medvedev and A. A. Yaremchenko, *Electrochim. Acta*, 2020, **337**, 135808.
- 208 K. Wissel, J. Heldt, P. B. Groszewicz, S. Dasgupta, H. Breitzke, M. Donzelli, A. I. Waidha, A. D. Fortes, J. Rohrer, P. R. Slater, G. Buntkowsky and O. Clemens, *Inorg. Chem.*, 2018, **57**, 6549–6560.
- 209 M. Ali Nowroozi, K. Wissel, M. Donzelli, N. Hosseinpourkavaz, S. Plana-Ruiz, U. Kolb, R. Schoch, M. Bauer, A. M. Malik, J. Rohrer, S. Ivlev, F. Kraus and O. Clemens, *Commun. Mater.*, 2020, **1**, 27.
- 210 M. Zinkevich and F. Aldinger, *J. Alloys Compd.*, 2004, **375**, 147–161.
- 211 A. N. Petrov, V. A. Cherepanov, A. Y. Zuyev and V. M. Zhukovsky, *J. Solid State Chem.*, 1988, **77**, 1–14.
- 212 D. E. Rice and D. J. Buttrey, *J. Solid State Chem.*, 1993, **105**, 197–210.
- 213 A. A. Yaremchenko, V. V. Kharton, M. V. Patrakeev and J. R. Frade, *J. Mater. Chem.*, 2003, **13**, 1136–1144.
- 214 V. V. Kharton, A. A. Yaremchenko, A. L. Shaula, M. V. Patrakeev, E. N. Naumovich, D. I. Logvinovich, J. R. Frade and F. M. BMarques, *J. Solid State Chem.*, 2004, **177**, 26–37.
- 215 P. Odier, Y. Nigara, J. Coutures and M. Sayer, *J. Solid State Chem.*, 1985, **56**, 32–40.
- 216 M. Zinkevich, N. Solak, H. Nitsche, M. Ahrens and F. Aldinger, *J. Alloys Compd.*, 2007, **438**, 92–99.
- 217 Y. Adachi, N. Hatada, K. Hirota, M. Kato and T. Uda, *J. Am. Ceram. Soc.*, 2019, **102**, 7077–7088.
- 218 G. Amow, I. J. Davidson and S. J. Skinner, *Solid State Ionics*, 2006, **177**, 1205–1210.
- 219 N. Gauquelin, T. E. Weirich, M. Ceretti, W. Paulus and M. Schroeder, *Monatsh. Chem.*, 2009, **140**, 1095–1102.
- 220 A. Montenegro Hernández, L. Mogni and A. Caneiro, *Int. J. Hydrogen Energy*, 2010, **35**, 6031–6036.
- 221 R. Sayers and S. J. Skinner, *J. Mater. Chem.*, 2011, **21**, 414–419.
- 222 J. D. Sullivan, D. J. Buttrey, D. E. Cox and J. Hriljac, *J. Solid State Chem.*, 1991, **94**, 337–351.
- 223 H. S. C. O'Neill and M. I. Pownceby, *Contrib. Mineral. Petrol.*, 1993, **114**, 296–314.
- 224 P. Odier, C. Allançon and J. M. Bassat, *J. Solid State Chem.*, 2000, **153**, 381–385.
- 225 A. V. Kovalevsky, V. V. Kharton, A. A. Yaremchenko, Y. V. Pivak, E. N. Naumovich and J. R. Frade, *J. Eur. Ceram. Soc.*, 2007, **27**, 4269–4272.
- 226 A. Montenegro-Hernandez, J. Vega-Castillo, L. Mogni and A. Caneiro, *Int. J. Hydrogen Energy*, 2011, **36**, 15704–15714.
- 227 S. Saher, J. Song, V. Vibhu, C. Nicollet, A. Flura, J.-M. Bassat and H. J. M. Bouwmeester, *J. Mater. Chem. A*, 2018, **6**, 8331–8339.
- 228 V. Vibhu, J.-M. Bassat, A. Flura, C. Nicollet, J.-C. Grenier and A. Rougier, *ECS Trans.*, 2015, **68**, 825–835.
- 229 V. Vibhu, A. Flura, A. Rougier, C. Nicollet, S. Fourcade, T. Hungria, J.-C. Grenier and J.-M. Bassat, *J. Energy Chem.*, 2020, **46**, 62–70.
- 230 J. Xue, A. Schulz, H. Wang and A. Feldhoff, *J. Membr. Sci.*, 2016, **497**, 357–364.
- 231 P. Batocchi, F. Mauvy, S. Fourcade and M. Parco, *Electrochim. Acta*, 2014, **145**, 1–10.
- 232 W. Li, B. Guan, L. Ma, S. Hu, N. Zhang and X. Liu, *J. Mater. Chem. A*, 2018, **6**, 18057–18066.
- 233 S. Upasen, P. Batocchi, F. Mauvy, A. Slodczyk and P. Colomban, *J. Alloys Compd.*, 2015, **622**, 1074–1085.
- 234 S. Engels, T. Markus, M. Modigell and L. Singheiser, *J. Membr. Sci.*, 2011, **370**, 58–69.
- 235 Q. Wei, S. Zhang, B. Meng, N. Han, Z. Zhu and S. Liu, *Mater. Lett.*, 2018, **230**, 161–165.
- 236 N. Han, Q. Wei, H. Tian, S. Zhang, Z. Zhu, J. Liu and S. Liu, *Energy Technol.*, 2018, **7**, 1800701.
- 237 G. Chen, M. Widenmeyer, B. Tang, L. Kaeswurm, L. Wang, A. Feldhoff and A. Weidenkaff, *Front. Chem. Sci. Eng.*, 2020, **14**, 405–414.
- 238 K. S. Yun, J. H. Park, Y. Kwon, D. Y. Kim, C.-Y. Yoo, J. H. Yu and J. H. Joo, *J. Mater. Chem. A*, 2016, **4**, 13549–13554.
- 239 Y. Kwon, J. H. Park, S. M. Kang, G. D. Nam, J. W. Lee, J. H. Kim, D. Kim, S. M. Jeong, J. H. Yu and J. H. Joo, *Energy Environ. Sci.*, 2019, **12**, 1358–1368.
- 240 S.-N. Lee, A. Atkinson and J. Kilner, *ECS Trans.*, 2013, **57**, 605–613.
- 241 K. J. Lee, J. H. Chung, M. J. Lee and H. J. Hwang, *J. Korean Ceram. Soc.*, 2019, **56**, 160–166.
- 242 M. Yang, E. Bucher and W. Sitte, *J. Power Sources*, 2011, **196**, 7313–7317.
- 243 Y. Gong, R. Wang, J. Banner, S. N. Basu, U. B. Pal and S. Gopalan, *JOM*, 2019, **71**, 3848–3858.
- 244 A. Egger, N. Schrodll, C. Gspan and W. Sitte, *Solid State Ionics*, 2017, **299**, 18–25.

- 245 N. Schrodli, E. Bucher, A. Egger, P. Kreiml, C. Teichert, T. Hoschen and W. Sitte, *Solid State Ionics*, 2015, **276**, 62–71.
- 246 N. Schrodli, A. Egger, C. Gspan, T. Hoschen, F. Horer and W. Sitte, *Solid State Ionics*, 2018, **322**, 44–53.
- 247 D.-P. Huang, Q. Xu, W. Chen, F. Zhang and H.-X. Liu, *Ceram. Int.*, 2008, **34**, 651–655.
- 248 M. Chen, B. H. Moon, S. H. Kim, B. H. Kim, Q. Xu and B. -G. Ahn, *Fuel Cells*, 2012, **12**, 86–96.
- 249 D. Huang, Q. Xu, F. Zhang, W. Chen, H. Liu and J. Zhou, *Mater. Lett.*, 2006, **60**, 1892–1895.
- 250 S. Nishiyama, D. Sakaguchi and T. Hattori, *Solid State Commun.*, 1995, **94**, 279–282.
- 251 K. Ishikawa, W. Shibata, K. Watanabe, T. Isonaga, M. Hashimoto and Y. Suzuki, *J. Solid State Chem.*, 1997, **131**, 275–281.
- 252 G. Taillades, J. Dailly, M. Taillades-Jacquín, F. Mauvy, A. Essouhmi, M. Marrony, C. Lalanne, S. Fourcade, D. J. Jones, J. -C. Grenier and J. Roziere, *Fuel Cells*, 2010, **10**, 166–173.
- 253 A. A. Kolchugin, E. Y. Pikalova, N. M. Bogdanovich, D. I. Bronin and E. A. Filonova, *Russ. J. Electrochem.*, 2017, **53**, 826–833.
- 254 J. B. Goodenough, *Mater. Res. Bull.*, 1973, **8**, 423–431.
- 255 J. B. Goodenough and S. Ramasesha, *Mater. Res. Bull.*, 1982, **17**, 383–390.
- 256 J. B. Goodenough, *J. Less-Common Met.*, 1986, **116**, 83–93.
- 257 N. Poirot, P. Odier, P. Simon and F. Gervais, *Solid State Sci.*, 2003, **5**, 735–739.
- 258 S.-Y. Jeon, M.-B. Choi, J.-H. Hwang, E. D. Wachsman and S.-J. Song, *J. Electrochem. Soc.*, 2011, **158**, B476–B480.
- 259 C. N. R. Rao, D. J. Buttrey, N. Otsuka, P. Ganguly, H. R. Harrison, C. J. Sandberg and J. M. Honig, *J. Solid State Chem.*, 1984, **51**, 266–269.
- 260 J. M. Bassat, F. Gervais, P. Odier and J. P. Loup, *Mater. Sci. Eng., B*, 1989, **3**, 507–514.
- 261 K. Sugiyama, H. Nozaki, T. Takeuchi and H. Ikuta, *J. Phys. Chem. Solids*, 2002, **63**, 979–982.
- 262 A. Murata, T. Uchikoshi and M. Matsuda, *J. Power Sources*, 2015, **293**, 95–100.
- 263 A. L. Shaula, E. N. Naumovich, A. P. Viskup, V. V. Pankov, A. V. Kovalevsky and V. V. Kharton, *Solid State Ionics*, 2009, **180**, 812–816.
- 264 J. M. Bassat, J. P. Loup and P. Odier, *J. Phys.: Condens. Matter*, 1994, **6**, 8285–8293.
- 265 C. Solís, L. Navarrete and J. M. Serra, *J. Power Sources*, 2013, **240**, 691–697.
- 266 Y. Shen, H. Zhao, J. Xu, X. Zhang, K. Zheng and K. Swierczek, *Int. J. Hydrogen Energy*, 2014, **39**, 1023–1029.
- 267 V. A. Sadykov, E. M. Sadvskaya, E. Y. Pikalova, A. A. Kolchugin, E. A. Filonova, S. M. Pikalov, N. F. Eremeev, A. V. Ishchenko, A. I. Lukashevich and J. M. Bassat, *Ionics*, 2018, **24**, 1181–1193.
- 268 J. Yang, J. Cheng, Q. Jiang, Y. Wang, R. Wang and J. Gao, *Int. J. Hydrogen Energy*, 2012, **37**, 1746–1751.
- 269 V. V. Vashook, N. E. Trofimenko, H. Ullmann and L. V. Makhnach, *Solid State Ionics*, 2000, **131**, 329–336.
- 270 T. Klande, S. Cusenza, P. Gacyszynski, K.-D. Becker, L. Dorrer, G. Borchardt and A. Feldhoff, *Solid State Ionics*, 2012, **222–223**, 8–15.
- 271 M. V. Patrakeev, E. N. Naumovich, V. V. Kharton, A. A. Yaremchenko, E. V. Tsipis, P. Nunez and J. R. Frade, *Solid State Ionics*, 2005, **176**, 179–188.
- 272 V. V. Kharton, A. P. Viskup, E. N. Naumovich and F. M. B. Marques, *J. Mater. Chem.*, 1999, **9**, 2623–2629.
- 273 V. V. Kharton, A. P. Viskup, A. V. Kovalevsky, E. N. Naumovich and F. M. B. Marques, *Solid State Ionics*, 2001, **143**, 337–353.
- 274 B. I. Arias-Serrano, E. Kravchenko, K. Zakharchuk, J. Grins, G. Svensson, V. Pankov and A. Yaremchenko, *ECS Trans.*, 2019, **91**, 2387–2397.
- 275 Y. Shen, H. Zhao, K. Świerczek, Z. Du and Z. Xie, *J. Power Sources*, 2013, **240**, 759–765.
- 276 J. Hyodo, K. Tominaga, Y.-W. Ju, S. Ida and T. Ishihara, *Solid State Ionics*, 2014, **256**, 5–10.
- 277 J. M. Bassat, P. Odier, A. Villesuzanne, C. Marin and M. Pouchard, *Solid State Ionics*, 2004, **167**, 341–347.
- 278 H.-S. Kim and H.-I. Yoo, *Phys. Chem. Chem. Phys.*, 2011, **13**, 4651–4658.
- 279 H.-S. Kim and H.-I. Yoo, *Phys. Chem. Chem. Phys.*, 2014, **16**, 16595–16605.
- 280 A. R. Gilev, E. A. Kiselev, D. S. Chezganov and V. A. Cherepanov, *Ceram. Int.*, 2020, **46**, 17553–17560.
- 281 A. R. Gilev, E. A. Kiselev and V. A. Cherepanov, *J. Mater. Chem. A*, 2018, **6**, 5304–5312.
- 282 V. A. Sadykov, E. Y. Pikalova, A. A. Kolchugin, A. V. Fetisov, E. M. Sadvskaya, E. A. Filonova, N. F. Eremeev, V. B. Goncharov, A. V. Krasnov, P. I. Skriabin, A. N. Shmakov, Z. S. Vinokurov, A. V. Ishchenko and S. M. Pikalov, *Int. J. Hydrogen Energy*, 2020, **45**, 13625–13642.
- 283 F. Mauvy, E. Boehm, J. M. Bassat, J. C. Grenier and J. Fouletier, *Solid State Ionics*, 2007, **178**, 1200–1204.
- 284 S.-Y. Jeon, Y.-S. Yoo, B. Singh, H.-N. Im and S.-J. Song, *J. Electrochem. Soc.*, 2016, **163**, F1302–F1307.
- 285 J. Xue, Q. Liao, W. Chen, H. J. M. Bouwmeester, H. Wang and A. Feldhoff, *J. Mater. Chem. A*, 2015, **3**, 19107–19114.
- 286 T. Ina, Y. Orikasa, T. Masese, T. Nakao, A. Mineshige, K. Amezawa, H. Tanida, T. Uruga and Y. Uchimoto, *Electrochemistry*, 2014, **82**, 875–879.
- 287 A. Egger and W. Sitte, *Solid State Ionics*, 2014, **258**, 30–37.
- 288 W. Li, B. Guan, X. Zhang, J. Yan, Y. Zhou and X. Liu, *Phys. Chem. Chem. Phys.*, 2016, **18**, 8502–8511.
- 289 Z. Li and R. Haugsrud, *Solid State Ionics*, 2012, **206**, 67–71.
- 290 S. J. Skinner and J. A. Kilner, *Solid State Ionics*, 2000, **135**, 709–712.
- 291 E. S. Tropin, M. V. Ananyev, A. S. Farlenkov, A. V. Khodimchuk, A. V. Berenov, A. V. Fetisov, V. A. Eremin and A. A. Kolchugin, *J. Solid State Chem.*, 2018, **262**, 199–213.
- 292 J. A. Kilner, S. J. Skinner and H. H. Brongersma, *J. Solid State Electrochem.*, 2011, **15**, 861–876.
- 293 T. Inprasit, S. Wongkasemjit, S. J. Skinner, M. Burriel and P. Limthongkul, *RSC Adv.*, 2015, **5**, 2486–2492.

- 294 K. Develos-Bagarinao, J. D. Vero, H. Kishimoto, T. Ishiyama, K. Yamaji, T. Horita and H. Yokokawa, *Phys. Chem. Chem. Phys.*, 2019, **21**, 7183–7195.
- 295 J. Railsback, G. Hughes, L. Mogni, A. Montenegro-Hernandez and S. Barnett, *J. Electrochem. Soc.*, 2016, **163**, F1433–F1439.
- 296 K. Yakal-Kremiski, L. V. Mogni, A. Montenegro-Hernandez, A. Caneiro and S. A. Barnett, *J. Electrochem. Soc.*, 2014, **161**, F1366–F1374.
- 297 J. Hyodo, K. Tominaga, Y.-W. Ju, S. Ida and T. Ishihara, *ECS Trans.*, 2014, **61**, 123–129.
- 298 S. J. Skinner and J. A. Kilner, *Ionics*, 1999, **5**, 171–174.
- 299 F. Mauvy, J. M. Bassat, E. Boehm, P. Dordor and J. P. Loup, *Solid State Ionics*, 2003, **158**, 395–407.
- 300 R. Sayers, R. A. D. Souza, J. A. Kilner and S. J. Skinner, *Solid State Ionics*, 2010, **181**, 386–391.
- 301 P.-M. Geffroy, L. Guironnet, H. J. M. Bouwmeester, T. Chartier, J.-C. Grenier and J.-M. Bassat, *J. Eur. Ceram. Soc.*, 2019, **39**, 59–65.
- 302 M. Burriel, H. Tellez, R. J. Chater, R. Castaing, P. Veber, M. Zaghioui, T. Ishihara, J. A. Kilner and J.-M. Bassat, *J. Phys. Chem. C*, 2016, **120**, 17927–17938.
- 303 J.-M. Bassat, M. Burriel, O. Wahyudi, R. Castaing, M. Ceretti, P. Veber, I. Weill, A. Villesuzanne, J.-C. Grenier, W. Paulus and J. A. Kilner, *J. Phys. Chem. C*, 2013, **117**, 26466–26472.
- 304 M. Burriel, G. Garcia, J. Santiso, J. A. Kilner, R. J. Chater and S. J. Skinner, *J. Mater. Chem.*, 2008, **18**, 416–422.
- 305 J. A. Lane and J. A. Kilner, *Solid State Ionics*, 2000, **136–137**, 997–1001.
- 306 Z. Li, T. Norby and R. Haugrud, *J. Am. Ceram. Soc.*, 2012, **95**, 2065–2073.
- 307 A. Egger, E. Bucher and W. Sitte, *J. Electrochem. Soc.*, 2011, **158**, B573–B579.
- 308 G. Kim, S. Wang, A. J. Jacobson and C. L. Chen, *Solid State Ionics*, 2006, **177**, 1461–1467.
- 309 G. Garcia, M. Burriel, N. Bonanos and J. Santiso, *J. Electrochem. Soc.*, 2008, **155**, P28–P32.
- 310 J. B. Smith and T. Norby, *J. Electrochem. Soc.*, 2006, **153**, A233–A238.
- 311 S.-Y. Jeon, M.-B. Choi, H.-N. Im, J.-H. Hwang and S.-J. Song, *J. Phys. Chem. Solids*, 2012, **73**, 656–660.
- 312 S.-Y. Jeon, H.-N. Im, B. Singh, S.-K. Hong and S.-J. Song, *Ceram. Int.*, 2014, **40**, 16785–16790.
- 313 R. Moreno, J. Zapata, J. Roqueta, N. Bagues and J. Santiso, *J. Electrochem. Soc.*, 2014, **161**, F3046–F3051.
- 314 R. Moreno, P. Garcia, J. Zapata, J. Roqueta, J. Chaigneau and J. Santiso, *Chem. Mater.*, 2013, **25**, 3640–3647.
- 315 M. Ghamarinia, A. Babaei and C. Zamani, *Electrochim. Acta*, 2020, **353**, 136520.
- 316 C. Berger, A. Egger, R. Merkle, E. Bucher, B. Stuhlhofer, N. Schrodler, J. Lammer, C. Gspan, G. Logvenov and J. Maier, *J. Electrochem. Soc.*, 2019, **166**, F1088–F1095.
- 317 V. A. Sadykov, N. F. Ereemeev, V. V. Usoltsev, A. S. Bobin, G. M. Alikina, V. V. Pelipenko, E. M. Sadovskaya, V. S. Muzykantov, N. N. Bulgakov and N. F. Uvarov, *Russ. J. Electrochem.*, 2013, **49**, 645–651.
- 318 N. M. Porotnikova, A. V. Khodimchuk, M. V. Ananyev, V. A. Eremin, E. S. Tropin, A. S. Farlenkov, E. Y. Pikalova and A. V. Fetisov, *J. Solid State Electrochem.*, 2018, **22**, 2115–2126.
- 319 H. J. M. Bouwmeester, C. Song, J. Zhu, J. Yi, M. S. Annalanda and B. A. Boukamp, *Phys. Chem. Chem. Phys.*, 2009, **11**, 9640–9643.
- 320 A. Boreave, H. Tan, V. Roche, P. Vernoux and J.-P. Deloume, *Solid State Ionics*, 2008, **179**, 1071–1075.
- 321 L. Minervini, R. W. Grimes, J. A. Kilner and K. E. Sickafus, *J. Mater. Chem.*, 2000, **10**, 2349–2354.
- 322 M. S. D. Read, M. S. Islam, F. King and F. E. Hancock, *J. Phys. Chem. B*, 1999, **103**, 1558–1562.
- 323 A. R. Cleave, J. A. Kilner, S. J. Skinner, S. T. Murphy and R. W. Grimes, *Solid State Ionics*, 2008, **179**, 823–826.
- 324 E. N. Naumovich and V. V. Kharton, *J. Mol. Struct.: THEOCHEM*, 2010, **946**, 57–64.
- 325 A. Chroneos, D. Parfitt, J. A. Kilner and R. W. Grimes, *J. Mater. Chem.*, 2010, **20**, 266–270.
- 326 A. Piovano, A. Perrichon, M. Boehm, M. R. Johnson and W. Paulus, *Phys. Chem. Chem. Phys.*, 2016, **18**, 17398–17403.
- 327 D. Parfitt, A. Chroneos, J. A. Kilner and R. W. Grimes, *Phys. Chem. Chem. Phys.*, 2010, **12**, 6834–6836.
- 328 M. Yashima, H. Yamada, S. Nuansaeng and T. Ishihara, *Chem. Mater.*, 2012, **24**, 4100–4113.
- 329 W. Xie, Y.-L. Lee, Y. Shao-Horn and D. Morgan, *J. Phys. Chem. Lett.*, 2016, **7**, 1939–1944.
- 330 V. Sadykov, E. Pikalova, N. Ereemeev, A. Shubin, I. Zilberberg, I. Prosvirin, E. Sadovskaya and A. Bukhtiyarov, *Solid State Ionics*, 2020, **344**, 115155.
- 331 S. Xu, R. Jacobs and D. Morgan, *Chem. Mater.*, 2018, **30**, 7166–7177.
- 332 L. Zhang, F. Yao, J. Meng, W. Zhang, H. Wang, X. Liu, J. Meng and H. Zhang, *J. Mater. Chem. A*, 2019, **7**, 18558–18567.
- 333 M. Yashima, M. Enoki, T. Wakita, R. Ali, Y. Matsushita, F. Izumi and T. Ishihara, *J. Am. Chem. Soc.*, 2008, **130**, 2762–2763.
- 334 M. Yashima, N. Sirikanda and T. Ishihara, *J. Am. Chem. Soc.*, 2010, **132**, 2385–2392.
- 335 M. Schroeder and M.-A. Dragan, *J. Mater. Sci.*, 2007, **42**, 1972–1983.
- 336 Q. Liao, L. Zhuang, Y. Wei, J. Xue and H. Wang, *Ceram. Int.*, 2018, **44**, 10852–10857.
- 337 Z. Li, R. Haugrud and T. Norby, *Solid State Ionics*, 2011, **184**, 42–46.
- 338 Z. Li, R. Haugrud, J. B. Smith and T. Norby, *J. Electrochem. Soc.*, 2009, **156**, B1039–B1044.
- 339 Z. Zhu, M. Li, C. Xia and H. J. M. Bouwmeester, *J. Mater. Chem. A*, 2017, **5**, 14012–14019.
- 340 S. Miyoshi, T. Furuno, H. Matsumoto and T. Ishihara, *Solid State Ionics*, 2006, **177**, 2269–2273.
- 341 V. V. Kharton, A. A. Yaremchenko, E. V. Tsipis and J. R. Frade, in *Proceedings of Eighth International Symposium on Solid Oxide Fuel Cells (SOFC-VIII)*, ed. S. C. Singhal and M. Dokiya, The Electrochemical Society Inc., Pennington, NJ, 2003, PV 2003-07, pp. 561–570.

- 342 N. A. Tarasova, A. O. Galisheva and I. E. Animitsa, *Russ. J. Electrochem.*, 2019, **55**, 756–761.
- 343 N. Tarasova and I. Animitsa, *C. R. Chim.*, 2019, **22**, 363–368.
- 344 N. Tarasova and I. Animitsa, *Solid State Sci.*, 2019, **87**, 87–92.
- 345 M. I. Vlasov, N. A. Tarasova, A. O. Galisheva, I. E. Animitsa and M. V. Ananyev, *Phys. Chem. Chem. Phys.*, 2019, **21**, 23459–23465.
- 346 N. Tarasova and I. Animitsa, *J. Fluorine Chem.*, 2018, **216**, 107–111.
- 347 N. Tarasova and I. Animitsa, *Solid State Ionics*, 2018, **317**, 21–25.
- 348 N. Tarasova and I. Animitsa, *J. Alloys Compd.*, 2018, **739**, 353–359.
- 349 J. Lyagaeva, D. Medvedev, E. Pikalova, S. Plaksin, A. Brouzgou, A. Demin and P. Tsiakaras, *Int. J. Hydrogen Energy*, 2017, **42**, 1715–1723.
- 350 J. R. Tolchard and T. Grande, *Solid State Ionics*, 2007, **178**, 593–599.
- 351 Y. Rao, S. Zhong, F. He, Z. Wang, R. Peng and Y. Lu, *Int. J. Hydrogen Energy*, 2012, **37**, 12522–12527.
- 352 Y. Lin, R. Ran, Y. Zheng, Z. Shao, W. Jin, N. Xu and J. Ahn, *J. Power Sources*, 2008, **180**, 15–22.
- 353 Y. Lin, R. Ran, C. Zhang, R. Cai and Z. Shao, *J. Phys. Chem. A*, 2010, **114**, 3764–3772.
- 354 D. Medvedev, A. Murashkina, E. Pikalova, A. Demin, A. Podias and P. Tsiakaras, *Prog. Mater. Sci.*, 2014, **60**, 72–129.
- 355 Y. K. Chung, Y.-U. Kwon and S. H. Byeon, *Bull. Korean Chem. Soc.*, 1995, **16**, 120–125.
- 356 Y. Zhu, D. Wang, F. Yuan, G. Zhang and H. Fu, *Appl. Catal., B*, 2008, **82**, 255–263.
- 357 E. Quarez, Y. Oumellal and O. Joubert, *Fuel Cells*, 2013, **13**, 34–41.
- 358 C. Yang, X. Zhang, H. Zhao, Y. Shen, Z. Du and C. Zhanga, *Int. J. Hydrogen Energy*, 2015, **40**, 2800–2807.
- 359 E. Y. Pikalova and A. A. Kolchugin, *Eurasian Chem.-Technol. J.*, 2016, **18**, 3–11.
- 360 G. Li, H. Jin, Y. Cui, L. Gui, B. He and L. Zhao, *J. Power Sources*, 2017, **341**, 192–198.
- 361 N. Danilov, J. Lyagaeva, G. Vdovin, E. Pikalova and D. Medvedev, *Energy Convers. Manage.*, 2018, **172**, 129–137.
- 362 H. An, D. Shin and H.-I. Ji, *J. Korean Ceram. Soc.*, 2018, **55**, 358–363.
- 363 L. Miao, J. Hou, Z. Gong, Z. Jin and W. Liu, *Int. J. Hydrogen Energy*, 2019, **44**, 7531–7537.
- 364 A. Tarutin, J. Lyagaeva, A. Farlenkov, S. Plaksin, G. Vdovin, A. Demin and D. Medvedev, *Mater.*, 2019, **12**, 118.
- 365 W. Li, B. Guan, L. Ma, H. Tian and X. Liu, *ACS Appl. Mater. Interfaces*, 2019, **11**, 18323–18330.
- 366 A. Løken, S. Ricote and S. Wachowski, *Crystals*, 2018, **8**, 365.
- 367 R. Raghvendra, R. K. Singh and P. Singh, *J. Mater. Sci.*, 2014, **49**, 5571–5578.
- 368 D. Tsvetkov, N. Tsvetkova, I. Ivanov, D. Malyshev, V. Sereda and A. Zuev, *Energies*, 2019, **12**, 417.
- 369 P. Gao, A. Bolon, M. Taneja, Z. Xie, N. Orlovskaya and M. Radovic, *Solid State Ionics*, 2017, **300**, 1–9.
- 370 Y. G. Lyagaeva, D. A. Medvedev, A. K. Demin, P. Tsiakaras and O. G. Reznitskikh, *Phys. Solid State*, 2015, **57**, 285–289.
- 371 Y.-P. Wang, Q. Xu, D.-P. Huang, K. Zhao, M. Chen and B.-H. Kim, *Int. J. Hydrogen Energy*, 2016, **41**, 6476–6485.
- 372 V. Vibhu, A. Rougier, J.-C. Grenier and J.-M. Bassat, *ECS Trans.*, 2013, **57**, 2093–2100.
- 373 Y. G. Lyagaeva, N. A. Danilov, M. Y. Gorshkov, G. K. Vdovin, B. D. Antonov, A. K. Demin and D. A. Medvedev, *Russ. J. Appl. Chem.*, 2018, **91**, 583–590.
- 374 Y.-P. Wang, Q. Xu, D.-P. Huang, K. Zhao, M. Chen and B.-H. Kim, *Int. J. Hydrogen Energy*, 2017, **42**, 6290–6302.
- 375 A. Aguadero, J. A. Alonso, M. T. Fernandez-Diaz, M. J. Escudero and L. Daza, *J. Power Sources*, 2007, **169**, 17–24.
- 376 V. V. Kharton, A. V. Kovalevsky, M. Avdeev, E. V. Tsipis, M. V. Patrakeev, A. A. Yaremchenko, E. N. Naumovich and J. R. Frade, *Chem. Mater.*, 2007, **19**, 2027–2033.
- 377 J. Yeyongchaiwat, K. Nonthawissarut, S. Charojrochkul and N. Sukpirom, *Adv. Appl. Ceram.*, 2014, **114**, 1–8.
- 378 X.-D. Zhou, J. W. Templeton, Z. Nie, H. Chen, J. W. Stevenson and L. R. Pederson, *Electrochim. Acta*, 2012, **71**, 44–49.
- 379 J. Cheng, S. Zhang, B. Meng, J. Ding and X. Tan, *J. Alloys Compd.*, 2018, **742**, 966–976.
- 380 T.-W. Chiu, M.-X. Lin, H.-Y. Shih, B. Hwang, H.-Y. Chang and Y.-M. Wang, *Ceram. Int.*, 2017, **43**, S700–S704.
- 381 M. Li, J. Cheng, Y. Gan, S. Li, B. He and W. Sun, *J. Power Sources*, 2015, **275**, 151–158.
- 382 X. Meng, S. Lü, S. Liu, X. Liu, Y. Sui, X. Li, M. Pang, B. Wang, Y. Ji and M. Z. Hu, *Ceram. Int.*, 2015, **41**, 12107–12114.
- 383 T. Chen, Y. Zhou, C. Yuan, M. Liu, X. Meng, Z. Zhan, C. Xia and S. Wang, *J. Power Sources*, 2014, **269**, 812–817.
- 384 M. Letilly, A. L. G. L. Salle, M. Caldes, M. Marrony and O. Joubert, *Fuel Cells*, 2009, **9**, 622–629.
- 385 L.-P. Sun, Q. Li, H. Zhao, L.-H. Huo and J.-C. Grenier, *J. Power Sources*, 2008, **183**, 43–48.
- 386 R. Pelosato, G. Cordaro, D. Stucchi, C. Cristiani and G. Dotelli, *J. Power Sources*, 2015, **298**, 46–67.
- 387 L. Moggi, F. Prado, C. Jimenez and A. Caneiro, *Solid State Ionics*, 2013, **240**, 19–28.
- 388 B. Sikder, A. Chanda, S. Goswami, D. Bhattacharya and S. Velaga, *Mater. Chem. Phys.*, 2019, **236**, 121770.
- 389 L.-S. Unger, C. Niedrig, S. F. Wagner, W. Menesklou, S. Baumann, W. A. Meulenberg and E. Ivers-Tiffée, *J. Eur. Ceram. Soc.*, 2018, **38**, 2378–2387.
- 390 F. Liang, Z. Yang, H. Deng, J. Sunarso, L. Yang and J. Mao, *J. Mater. Sci. Technol.*, 2019, **35**, 1184–1191.
- 391 H. Hao, L. Zhao, J. Hu, X. Hu and H. Hou, *J. Rare Earths*, 2009, **27**, 815–818.
- 392 N. A. Danilov, A. P. Tarutin, J. G. Lyagaeva, E. Y. Pikalova, A. A. Murashkina, D. A. Medvedev, M. V. Patrakeev and A. K. Demin, *Ceram. Int.*, 2017, **43**, 15418–15423.
- 393 W. H. Kan, K.-Y. Lai, A. Huq and A. Manthiram, *J. Power Sources*, 2016, **307**, 454–461.
- 394 S. R. Bishop, D. Marrocchelli, C. Chatzichristodoulou, N. H. Perry, M. B. Mogensen, H. L. Tuller and E. D. Wachsman, *Annu. Rev. Mater. Res.*, 2014, **44**, 205–239.

- 395 S. R. Bishop, K. L. Duncan and E. D. Wachsman, *J. Am. Ceram. Soc.*, 2010, **93**, 4115–4121.
- 396 S. R. Bishop, K. L. Duncan and E. D. Wachsman, *Acta Mater.*, 2009, **57**, 3596–3605.
- 397 T. Nakamura, K. Yashiro, K. Sato and J. Mizusaki, *Solid State Ionics*, 2010, **181**, 292–299.
- 398 S. R. Bishop, D. Marrocchelli, W. Fang, K. Amezawa, K. Yashiro and G. W. Watson, *Energy Environ. Sci.*, 2013, **6**, 1142–1146.
- 399 V. V. Kharton, A. A. Yaremchenko, M. V. Patrakeev, E. N. Naumovich and F. M. B. Marques, *J. Eur. Ceram. Soc.*, 2003, **23**, 1417–1426.
- 400 V. V. Vashook, DSc. thesis, Institute of General and Inorganic Chemistry, National Belarus Academy of Sciences, Minsk, Belarus, 2000.
- 401 H. Ullmann, N. Trofimenko, F. Tietz, D. Stöver and A. Ahmad-Khanlou, *Solid State Ionics*, 2000, **138**, 79–90.
- 402 L. P. Putilov, N. A. Shevryev, A. M. Mineev, A. S. Farlenkov, D. A. Medvedev and V. I. Tsidilkovski, *Acta Mater.*, 2020, **190**, 70–80.
- 403 K. D. Kreuer, *Annu. Rev. Mater. Res.*, 2003, **33**, 333–359.
- 404 E. Fabbri, Daniele Pergolesi and Enrico Traversa, *Chem. Soc. Rev.*, 2010, **39**, 4355–4369.
- 405 N. Tarasova, A. Galisheva and I. Animitsa, *Ionics*, 2020, **26**, 5075–5088.
- 406 N. Tarasova, I. Animitsa and A. Galisheva, *J. Solid State Electrochem.*, 2020, **24**, 1497–1508.
- 407 N. A. Tarasova, A. O. Galisheva, I. E. Animitsa and D. V. Korona, *Russ. J. Phys. Chem. A*, 2020, **94**, 818–821.
- 408 N. Tarasova, I. Animitsa, A. Galisheva and V. Pryakhina, *Solid State Sci.*, 2020, **101**, 106121.
- 409 M. Chen, Y. Xuan, F. Zhang, L. He, X. Wang, H. Pan, J. Ren and Z. Lin, *Int. J. Hydrogen Energy*, 2020, **45**, 14964–14971.
- 410 W. Tan, D. Huan, W. Yang, N. Shi, W. Wang, R. Peng, X. Wu and Y. Lu, *RSC Adv.*, 2018, **8**, 26448–26460.
- 411 G. Rinaldi, A. Nakajo, P. Burdet, M. Cantoni, W. K. S. Chiu and J. Van herle, *Acta Mater.*, 2019, **178**, 194–206.
- 412 H. Moussaoui, R. K. Sharma, J. Debayle, Y. Gavet, G. Delette and J. Laurencin, *J. Power Sources*, 2019, **412**, 736–748.
- 413 W. Kong, M. Zhang, Z. Han and Q. Zhang, *Appl. Sci.*, 2019, **9**, 493.
- 414 P. Vijay, M. O. Tadéa, Z. Shao and M. Ni, *Int. J. Hydrogen Energy*, 2017, **42**, 28836–28851.
- 415 X. Lu, T. M. M. Heenan, J. J. Bailey, T. Li, K. Li, D. J. L. Brett and P. R. Shearing, *J. Power Sources*, 2017, **365**, 210–219.
- 416 E. V. Tsipis and V. V. Kharton, *J. Solid State Electrochem.*, 2008, **12**, 1039–1060.
- 417 X.-Y. Wu and A. F. Ghoniem, *Prog. Energy Combust. Sci.*, 2019, **74**, 1–30.
- 418 A. A. Plazaola, A. C. Labella, Y. Liu, N. B. Porras, D. A. P. Tanaka, M. V. S. Annaland and F. Gallucci, *Processes*, 2019, **7**, 128.
- 419 M. Acosta, F. Baiutti, A. Tarancón and J. L. MacManus-Driscoll, *Adv. Mater. Interfaces*, 2019, **6**, 1900462.
- 420 C. Li, J. J. Chew, A. Mahmoud, S. Liu and J. Sunarso, *J. Membr. Sci.*, 2018, **567**, 228–260.
- 421 C. Zhang, J. Sunarso and S. Liu, *Chem. Soc. Rev.*, 2017, **46**, 2941–3005.
- 422 V. L. Kozhevnikov, I. A. Leonidov and M. V. Patrakeev, *Russ. Chem. Rev.*, 2013, **82**, 772–782.
- 423 S. B. Adler, J. A. Lane and B. C. H. Steele, *J. Electrochem. Soc.*, 1996, **143**, 3554.
- 424 Z. Zhao, J. Cui, M. Zou, S. Mu, H. Huang, Y. Meng, K. He, K. S. Brinkman and J. Tong, *J. Power Sources*, 2020, **450**, 227609.
- 425 C. Xia, Y. Mi, B. Wang, B. Lin, G. Chen and B. Zhu, *Nat. Commun.*, 2019, **10**, 1707.
- 426 Y. Song, Y. Chen, W. Wang, C. Zhou, Y. Zhong, G. Yang, W. Zhou, M. Liu and Z. Shao, *Joule*, 2019, **3**, 2842–2853.
- 427 K. Wei, N. Li, Y. Wu, W. Song, X. Wang, L. Guo, M. Khan, S. Wang, F. Zho and Y. Ling, *Ceram. Int.*, 2019, **45**, 18583–18591.
- 428 R. Ren, Z. Wang, C. Xu, W. Sun, J. Qiao, D. W. Rooney and K. Sun, *J. Mater. Chem. A*, 2019, **7**, 18365–18372.
- 429 J. C. Grenier, F. Mauvy, C. Lalanne, J.-M. Bassat, F. Chauveau, J. Mougín, J. Dailly and M. Marrony, *ECS Trans.*, 2009, **25**, 2537–2546.
- 430 J. Hou, Z. Zhu, J. Qian and W. Liu, *J. Power Sources*, 2014, **264**, 67–75.
- 431 J. Hou, J. Qian, L. Bi, Z. Gong, R. Peng and W. Liu, *J. Mater. Chem. A*, 2015, **3**, 2207–2215.
- 432 Y. G. Lyagaeva, N. A. Danilov, M. Y. Gorshkov, G. K. Vdovin, B. D. Antonov, A. K. Demin and D. A. Medvedev, *Russ. J. Appl. Chem.*, 2018, **91**, 583–590.
- 433 E. P. Antonova, A. A. Kolchugin, E. Y. Pikalova, D. A. Medvedev and N. M. Bogdanovich, *Solid State Ionics*, 2017, **306**, 55–61.
- 434 E. Y. Pikalova, N. M. Bogdanovich and A. V. Kuzmin, *Russ. J. Electrochem.*, 2017, **53**, 752–760.
- 435 S. Yang, Y. Wen, J. Zhang, Y. Lu, X. Ye and Z. Wen, *Electrochim. Acta*, 2018, **267**, 269–277.
- 436 C. Sun, S. Yang, Y. Lu, J. Wen, X. Ye and Z. Wen, *J. Power Sources*, 2020, **449**, 227498.
- 437 A. P. Tarutin, M. Y. Gorshkov, I. N. Bainov, G. K. Vdovin, A. I. Vylkov, J. G. Lyagaeva and D. A. Medvedev, *Ceram. Int.*, 2020, **46**, 24355–24364.
- 438 T. Park, *J. Korean Soc. Precis. Eng.*, 2018, **35**, 1141–1146.
- 439 J. Dailly, F. Mauvy, M. Marrony, M. Pouchard and J.-C. Grenier, *J. Solid State Electrochem.*, 2011, **15**, 245–251.
- 440 S. M. Babinić, S. Ricote and N. P. Sullivan, *J. Electrochem. Soc.*, 2014, **161**, F717–F723.
- 441 A. Grimaud, F. Mauvy, J. M. Bassat, S. Fourcade, L. Rocheron, M. Marrony and J. C. Grenier, *J. Electrochem. Soc.*, 2012, **159**, B683–B694.
- 442 A. Y. Zuev, V. V. Sereda and D. S. Tsvetkov, *J. Electrochem. Soc.*, 2012, **159**, F594–F599.
- 443 N. E. Volkova, V. A. Kolotygin, L. Y. Gavrilova, V. V. Kharton and V. A. Cherepanov, *Solid State Ionics*, 2014, **260**, 15–20.
- 444 E. V. Tsipis, E. N. Naumovich, M. V. Patrakeev, A. A. Yaremchenko, I. P. Marozau, A. V. Kovalevsky, J. C. Waerenborgh and V. V. Kharton, *Solid State Ionics*, 2011, **192**, 42–48.

- 445 E. V. Tsipis, M. V. Patrakeev, P. V. Anikina, E. N. Naumovich and V. V. Kharton, *Mater. Lett.*, 2020, **265**, 127425.
- 446 A. A. Markov, O. V. Merkulov, M. V. Patrakeev and I. A. Leonidov, *Int. J. Hydrogen Energy*, 2019, **44**, 26807–26815.
- 447 C. Li, W. Li, J. J. Chew, S. Liu, X. Zhu and J. Sunarso, *Sep. Purif. Technol.*, 2020, **235**, 116224.
- 448 L. R. Tarutina, G. K. Vdovin, J. G. Lyagaeva and D. A. Medvedev, *J. Alloys Compd.*, 2020, **831**, 154895.
- 449 W. Deibert, M. E. Ivanova, S. Baumann, O. Guillon and W. A. Meulenber, *J. Membr. Sci.*, 2017, **543**, 79–97.
- 450 M. Li, H. Niu, J. Druce, H. Téllez, T. Ishihara, J. A. Kilner, H. Gasparyan, M. J. Pitcher, W. Xu, J. F. Shin, L. M. Daniels, L. A. H. Jones, V. R. Dhanak, D. Hu, M. Zanella, J. B. Claridge and M. J. Rosseinsky, *Adv. Mater.*, 2020, **32**, 1905200.
- 451 K. Ishii, C. Matsunaga, K. Kobayashi, A. J. Stevenson, C. Tardivat and T. Uchikoshi, *J. Eur. Ceram. Soc.*, 2019, **39**, 5292–5297.
- 452 E. V. Shubnikova, M. P. Popov, S. F. Bychkov, S. A. Chizhik and A. P. Nemudry, *Chem. Eng. J.*, 2019, **372**, 251–259.
- 453 D. Ding, X. Li, S. Y. Lai, K. Gerdes and M. Liu, *Energy Environ. Sci.*, 2014, **7**, 552–575.
- 454 S. P. Jiang, *Int. J. Hydrogen Energy*, 2012, **37**, 449–470.
- 455 C. Zhao, Y. Li, W. Zhang, Y. Zheng, X. Lou, B. Yu, J. Chen, Y. Chen, M. Liu and J. Wang, *Energy Environ. Sci.*, 2020, **13**, 53–85.
- 456 R. Zohourian, R. Merkle, G. Raimondi and J. Maier, *Adv. Funct. Mater.*, 2018, **28**, 1801241.
- 457 R. Zohourian, R. Merkle and J. Maier, *Solid State Ionics*, 2017, **299**, 64–69.
- 458 H. T. Lozano, J. Druce, S. J. Cooper and J. A. Kilner, *Sci. Technol. Adv. Mater.*, 2017, **18**, 977–986.
- 459 H. Tang, Z. Gong, Y. Wu, Z. Jin and W. Liu, *Int. J. Hydrogen Energy*, 2018, **43**, 19749–19756.
- 460 J. Dailly and M. Marrony, *J. Power Sources*, 2013, **240**, 323–327.
- 461 J. Dailly, M. Marrony, G. Taillades, M. Taillades-Jacquín, A. Grimaud, F. Mauvy, E. Louradour and J. Salmi, *J. Power Sources*, 2014, **255**, 302–307.
- 462 N. Nasani, D. Ramasamy, S. Mikhalev, A. V. Kovalevsky and D. P. Fagg, *J. Power Sources*, 2015, **278**, 582–589.
- 463 E. Pikalova, A. Kolchugin, N. Bogdanovich, D. Medvedev, J. Lyagaeva, L. Vedmid, M. Ananyev, S. Plaksin and A. Farlenkov, *Int. J. Hydrogen Energy*, 2020, **45**, 13612–13624.
- 464 A. Tarutin, A. Kasyanova, J. Lyagaeva, G. Vdovin and D. Medvedev, *J. Energy Chem.*, 2020, **40**, 65–74.
- 465 X. Li, D. Huan, N. Shi, Y. Yang, Y. Wan, C. Xia, R. Peng and Y. Lu, *Int. J. Hydrogen Energy*, 2020, **45**, 17736–17744.
- 466 A. Tarutin, N. Danilov, J. Lyagaeva and D. Medvedev, *Appl. Sci.*, 2020, **10**, 2481.
- 467 J. Lyagaeva, N. Danilov, G. Vdovin, J. Bu, D. Medvedev, A. Demin and P. Tsiakaras, *J. Mater. Chem. A*, 2016, **4**, 15390–15399.
- 468 S. Yang, Y. Lu, Q. Wang, C. Sun, X. Ye and Z. Wen, *Int. J. Hydrogen Energy*, 2018, **43**, 20050–20058.
- 469 S. Yang, S. Zhang, C. Sun, X. Ye and Z. Wen, *ACS Appl. Mater. Interfaces*, 2018, **10**, 42387–42396.
- 470 N. Danilov, A. Tarutin, J. Lyagaeva, G. Vdovin and D. Medvedev, *J. Mater. Chem. A*, 2018, **6**, 16341–16346.
- 471 N. Danilov, J. Lyagaeva, G. Vdovin and D. Medvedev, *Appl. Energy*, 2019, **237**, 924–934.
- 472 J. Li, J. Hou, Y. Lu, Q. Wang, X. Xi, Y. Fan, X.-Z. Fu and J.-L. Luo, *J. Power Sources*, 2020, **453**, 227909.
- 473 Y. Bu, S. Joo, Y. Zhang, Y. Wang, D. Meng, X. Ge and G. Kim, *J. Power Sources*, 2020, **451**, 227812.
- 474 S. Sun and Z. Cheng, *J. Electrochem. Soc.*, 2020, **167**, 024514.
- 475 D. Xie, K. Li, J. Yang, D. Yan, L. Jia, B. Chi, J. Pu and J. Li, *Int. J. Hydrogen Energy*, 2020, DOI: 10.1016/j.ijhydene.2020.01.014.
- 476 K. Miyazaki, Y. Ding, H. Muroyama, T. Matsui and K. Eguchi, *Electrochemistry*, 2020, **88**, 28–33.
- 477 C. Ren, Y. Zhang, Q. Xu, T. Tian and F. Chen, *Int. J. Hydrogen Energy*, 2020, **45**, 6926–6933.
- 478 M. Ahn, S. Hwang, S. Han, M. Choi, D. Byun and W. Lee, *Korean J. Chem. Eng.*, 2020, **37**, 1371–1378.
- 479 H. Tang, Z. Jin, Y. Wu, W. Liu and L. Bi, *Electrochem. Commun.*, 2019, **100**, 108–112.
- 480 A. He, J. Onishi, J. Gong and N. Shikazono, *J. Power Sources*, 2020, **478**, 228771.
- 481 N. A. Baharuddin, N. F. A. Rahman, H. A. Rahman, M. R. Somalu, M. A. Azmi and J. Raharjo, *Int. J. Energy Res.*, 2020, **44**, 8269–8313.
- 482 J. H. Shim, G. D. Han, H. J. Choi, Y. Kim, S. Xu, J. An, Y. B. Kim, T. Graf, T. D. Schladt, T. M. Gür and F. B. Prinz, *Int. J. Precis. Eng. Manuf.- Green Technol.*, 2019, **6**, 629–646.
- 483 E. G. Kalinina and E. Y. Pikalova, *Russ. Chem. Rev.*, 2019, **88**, 1179–1219.
- 484 P. A. Connor, X. Yue, C. D. Savaniu, R. Price, G. Triantafyllou, M. Cassidy, G. Kerherve, D. J. Payne, R. C. Maher, L. F. Cohen, R. I. Tomov, B. A. Glowacki, R. V. Kumar and J. T. S. Irvine, *Adv. Energy Mater.*, 2018, **8**, 1800120.
- 485 V. A. Tsvinkinberg, A. S. Tolkacheva, E. A. Filonova, O. I. Gyrdasova, S. M. Pikalov, V. A. Vorotnikov, A. I. Vylkov, N. I. Moskalenko and E. Y. Pikalova, *J. Alloys Compd.*, 2020, **853**, 156728.
- 486 V. A. Sadykov, E. M. Sadovskaya, E. A. Filonova, N. F. Ereemeev, V. D. Belyaev, V. A. Tsvinkinberg and E. Y. Pikalova, *Solid State Ionics*, 2020, **357**, 115432.
- 487 Q. Zhou, T. Zhang, C. Zhao, L. Qu, Y. He, T. Wei and X. Tong, *Mater. Res. Bull.*, 2020, **131**, 110986.
- 488 Y. Sadia, Y. Gelbstein and S. J. Skinner, *J. Solid State Chem.*, 2020, **290**, 121556.
- 489 E. A. Filonova, E. Yu. Pikalova, T. Yu. Maksimchuk, A. I. Vylkov, S. M. Pikalov and A. Maignan, *Int. J. Hydrogen Energy*, 2020, DOI: 10.1016/j.ijhydene.2020.10.243.
- 490 M. Khoshkalam, Đ. Tripković, X. Tong, M. A. Faghihi-Sani, M. Chen and P. V. Hendriksen, *J. Power Sources*, 2020, **457**, 228035.
- 491 T. Wan, A. Zhu, Y. Guo, C. Wang, S. Huang, H. Chen, G. Yang, W. Wang and Z. Shao, *J. Power Sources*, 2017, **348**, 9–15.